Supplementary Information

Lead carboxylates passivation for meter-scale perovskite solar modules

Dongdong Xu[1], Ke Xiao[1,2]*, Ye Liu[3], Xin Luo[3], Jian Xu[4], Yikang Wei[4], Yameen Ahmed[5], Shuncheng Yang[1], Haonan Liu[1], Yinke Wang[1], Shun Huang[1], Manya Li[1], YuhongZhang[1], Han Gao[1], Hongfei Sun[1], Gongtao Duan[1], Qiaolei Han[3], Qiang Liu[6], Shuo Zhang[6], Xingjie Lv[6], Jingfu Jiang[6], Li Chao[7], Dongxue Liu[8], Min Hao[9], Xincheng Hou[9], Makhsud I. Saidaminov[5], Hairen Tan[1,3]*

[1]National Laboratory of Solid State Microstructures, College of Engineering and Applied Sciences, Frontiers Science Center for Critical Earth Material Cycling, Jiangsu Physical Science Research Center, Nanjing University, Nanjing 210023, Jiangsu, China.

[2]School of Advanced Manufacturing Engineering, Nanjing University, Suzhou, 215163, China.

[3]Research and Development Center, Renshine Solar (Suzhou) Co., Ltd., Changshu 215500, Jiangsu, China.

[4]School of Interdisciplinary Science, Beijing Institute of Technology, Beijing 100081, China.

[5]Department of Chemistry, University of Victoria, Victoria, BC, Canada.

[6]Shandong Energy Group Co., Ltd., Jinan 250101, Shangdong, China.

[7]Inner Mongolia Three Gorges Mengneng Energy Co., Ltd., Ordos 014300, Inner Mongolia, China.

[8]Institute of Science and Technology Research, China Three Gorges Corporation, Beijing 100038, China.

[9]Jiangsu Fangyang New Energy Investment Co., Ltd., Yancheng 224000, Jiangsu, China.

*Corresponding authors. Email: ke.xiao@nju.edu.cn (K.X.); hairentan@nju.edu.cn (H.T.)

Contents

Supplementary Note 1:

The cosolvency of DOL:2-Me mixed solvents

We found that when high-SVP 2-Me is used as the primary solvent, it cannot completely dissolve the Cs-containing perovskite powder, even incorporating a 10% volume ratio of DMSO (Supplementary Fig. 1a). To solve this problem, a two-step dissolution method is reported by mixing 2-Me dissolved $FAPbI_3$ and DMSO dissolved $CsPbI_3$, yielding a temporarily stable $Cs_{0.03}FA_{0.97}PbI_3$ ink (Supplementary Fig. 1b). However, this solution precipitates after only 3 hours, making it unsuitable for long-term stable production. Notably, introducing 1,3-dioxolane (DOL), a weakly polar and high SVP solvent, alongside 2-Me and DMSO create a cosolvency effect to dissolve $Cs_{0.03}FA_{0.97}PbI_3$ powders, which can significantly enhance the stability of the resulting ink (Supplementary Fig. 1c). Besides, the incorporation of DOL with low boiling point can also elevate the SVP, by determining the liquid-vapor phase transition temperatures of 2-Me:DOL mixtures with varying volume ratios (Supplementary Fig. 2).

To deeply understand the potential mechanism of cosolvency, we prepared a perovskite ink with a concentration of 0.6 M and found that DOL exhibited a wide range of proportions in the $Cs_{0.03}FA_{0.97}PbI_3$ system (Supplementary Fig. 3). We further studied the solubility of cesium iodide (CsI), FAI, methylammonium chloride (MACl), or PbI_2 in the 2-Me:DOL mixed solvent system. However, the results showed that their individual solubility gradually decreased with an increasing DOL ratio (Supplementary Fig. 4). This indicates that the enhanced dissolution of the perovskite cannot be simply attributed to the solubility of its individual precursors. Although the ternary 2-Me:DOL:DMSO system can effectively dissolve it (Supplementary Fig. 5), DOL alone could not re-dissolve the precipitate that formed in the $Cs_{0.03}FA_{0.97}PbI_3$ ink using 2-Me and DMSO, highlighting that DOL's primary role is to prevent the precipitate formation in the first place.

To analyze the precipitate, we found that the yellow-green solid is a mixture of δ-$CsPbI_3$ and PbI_2 through X-ray diffraction (XRD) and optical characterization (Supplementary Fig. 6). We speculate that the role of DOL is to prevent the formation of stable δ-$CsPbI_3$ by releasing Cs^+ and PbI_2, in that the hydrogen-bonded 2-Me:DOL complex coordinates with Cs^+ (via ion-dipole interactions) to form a Cs-complex, thereby hindering its incorporation into the crystal lattice.

Thus, fourier transform infrared spectroscopy (FTIR) analysis reveals that DOL induces a blue shift in the -OH stretching vibration of 2-Me (Supplementary Fig. 7a), indicating that the incorporation of DOL disrupts the original self-association of 2-Me, causing the hydroxyl group to become freer. The hydrogen bonding strength between the oxygen atom in DOL and 2-Me is weaker than the hydrogen bonds between 2-Me molecules, leading to an increase in the hydroxyl vibration frequency and a blue shift in the peak position. ^{1}H nuclear magnetic resonance (^{1}H NMR) spectra of the DOL:2-Me mixture also shows chemical shifts that indicate the formation of hydroxyl hydrogen

(Supplementary Figs. 7b-7f). Notably, the hydroxyl hydrogen of 2-Me exhibits an up-field shift (to lower ppm) along with peak narrowing (Supplementary Fig. 7f). This further confirms that DOL reduces the hydrogen-bonded self-aggregation of 2-Me, providing a more uniform chemical environment for the hydroxyl protons. Together, these results suggest a "fast-binding" mechanism, in which the ether oxygen of DOL (rich in lone-pair electrons) readily approaches the hydroxyl hydrogen of 2-Me with minimal steric hindrance, forming a weak hydrogen-bonded complex composed of one DOL molecule and two 2-Me molecules.

We further calculated the electrostatic potential (ESP) of 2-Me and DOL, revealing complementary interaction regions between the two molecules (Supplementary Figs. 8a, b). Consistent with this, the optimized molecular geometries confirm a stable configuration where one DOL molecule coordinates with two 2-Me molecules via interactions between the hydroxyl group of 2-Me and the oxygen atoms of DOL (Supplementary Figs. 8c-8f).

To investigate the mechanism by which the hydrogen-bonded complex mediates both Cs^+ incorporation into the lattice and ink stability, we performed ab initio molecular dynamics (AIMD) simulations on mixed systems containing 2-Me, DOL, and Cs^+ (Supplementary Fig. 9, Supplementary Video1). AIMD simulation reveals the existence of a well-defined cesium complex, in which strong Cs^+-O ionic interactions occur via electrostatic coordination between Cs^+ and oxygen atoms. In perovskite systems, such a structure serves as a signature of ion-kinetic stabilization and contributes to ink stability.

Based on the above analysis, we proposed a mechanistic model illustrated in Supplementary Fig. 10, in which the cosolvency of DOL primarily originates from the Cs-complex formed in the DOL:2-Me:Cs^+ system. This structure hinders the incorporation of Cs^+ into the PbI_2 lattice through combined molecular-dynamic and steric-hindrance effects. It is well established that Cs^+ readily incorporates into the lattice to form the thermodynamically stable, low-temperature orthorhombic γ-$CsPbI_3$ phase. However, this phase spontaneously transforms into the non-perovskite, photo-inactive δ-$CsPbI_3$ phase under ambient conditions. The DOL-mediated Cs-complex effectively suppresses the lattice-doping process of Cs^+, thereby kinetically stabilizing the precursor ink, preventing the premature formation of the inactive phase, and creating favorable conditions for the subsequent preparation.

2-Methyltetrahydrofuran (2-MeTHF), employed in perovskite ink formulation, shares similar molecular structure and saturated vapor pressure with DOL. However, replacing DOL with 2-MeTHF in the ternary solvent system (2-Me:2-MeTHF:DMSO) fails to effectively dissolve the perovskite precursors, as evidenced by persistent ink turbidity (Supplementary Fig. 11). This result further highlights the unique advantage of DOL in stabilizing the precursor solution.

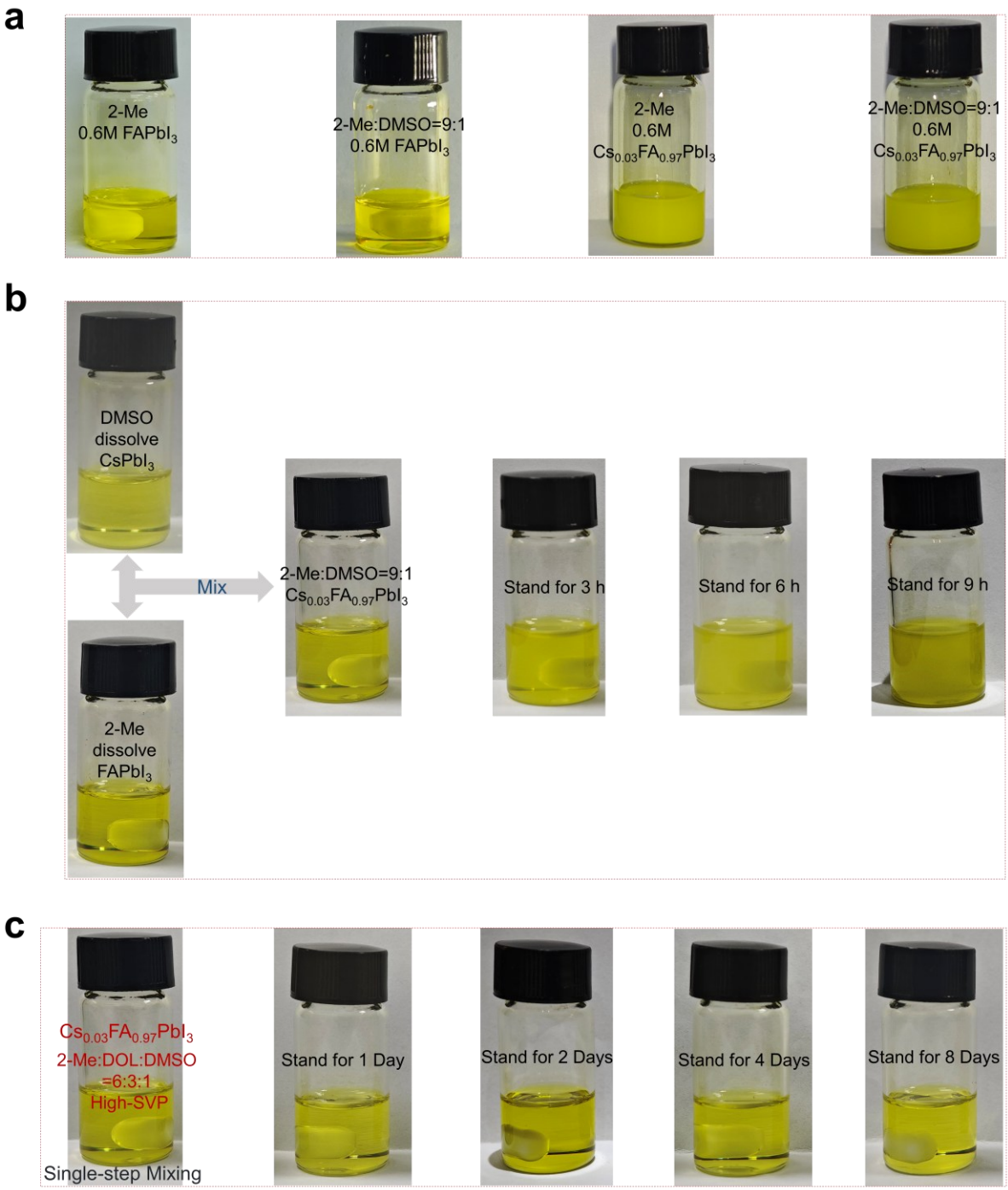

Supplementary Fig. 1 | The digital photos of the perovskite inks. a, Dissolution behavior of perovskite precursor in different solvents. $FAPbI_3$ dissolves completely, whereas $Cs_{0.03}FA_{0.97}PbI_3$ leads to the formation of precipitates. **b,** The two-step dissolution process for mixing $CsPbI_3$ and $FAPbI_3$. **c,** Standing stability of $Cs_{0.03}FA_{0.97}PbI_3$ perovskite dissolved in 2-Me:DOL:DMSO mixture. The ink maintains clear and stable after standing for 8 days.

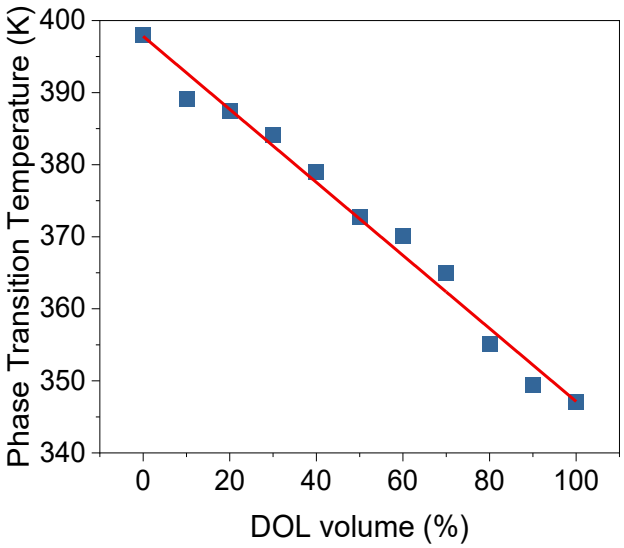

Supplementary Fig. 2 | Liquid-gas phase transition temperature of mixed solvents with different volume ratios of 2-Me and DOL.

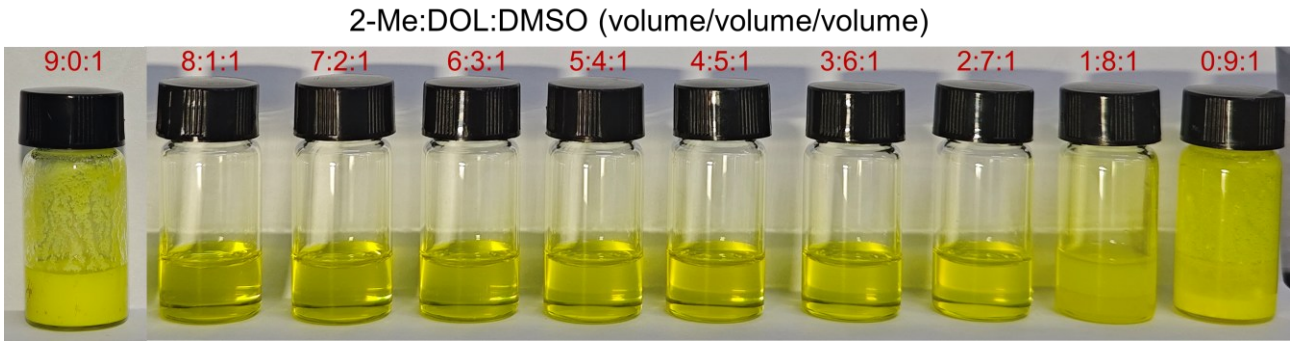

Supplementary Fig. 3 | The digital photos showing the solubility of perovskite precursor solution in different solvent ratios. The solute is $Cs_{0.03}FA_{0.97}PbI_3$ perovskite powder with 20% (mole ratio) MACl added. The concentration of $Cs_{0.03}FA_{0.97}PbI_3$ is 0.6 mole ratio.

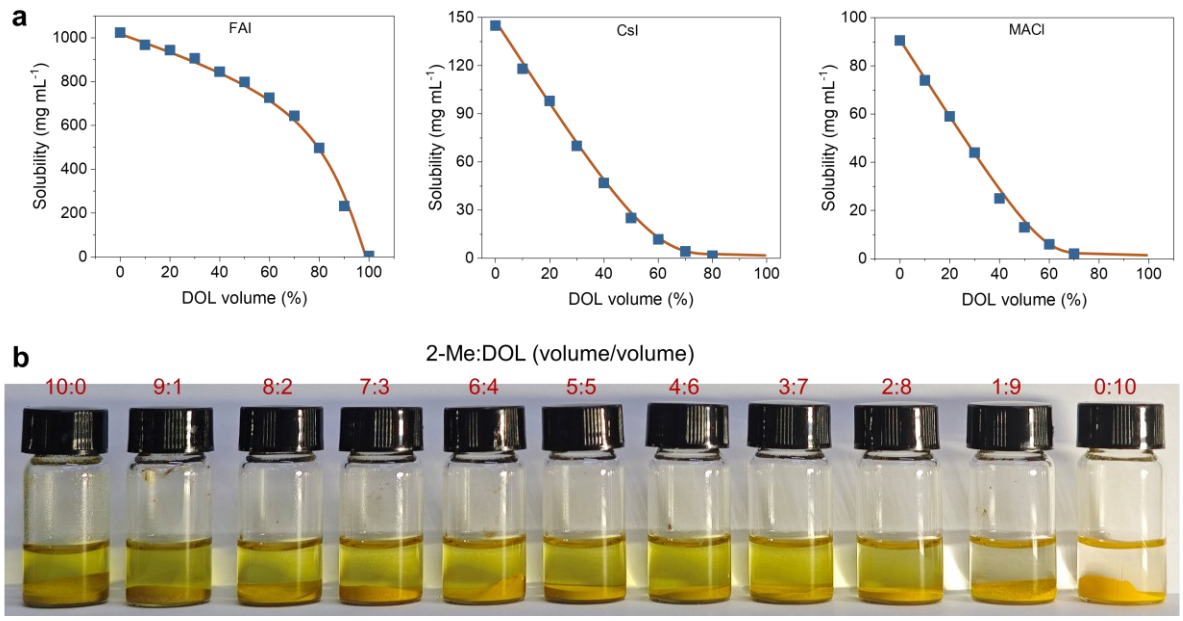

Supplementary Fig. 4 | Solubility of various perovskite precursor powders in DOL:2-Me solvents. **a,** Solubility of FAI, CsI and MACl in different 2-Me:DOL solvent ratios. **b,** PbI_2 is slightly soluble in 2-Me only and continuously become insoluble until it is in DOL. The concentration of PbI_2 is 0.6 mole ratio.

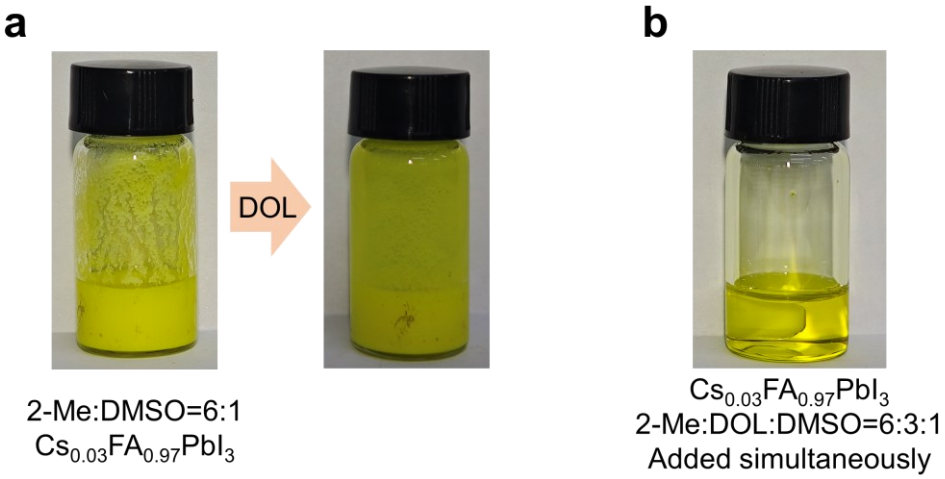

Supplementary Fig. 5 | Solubility of $Cs_{0.03}FA_{0.97}PbI_3$. a, $Cs_{0.03}FA_{0.97}PbI_3$ in the 2-Me:DMSO solvent system remains insoluble. The participation remains undissolved after adding DOL. **b,** The $Cs_{0.03}FA_{0.97}PbI_3$ perovskite can be easily dissolved using 2-Me:DOL:DMSO mixed solvents.

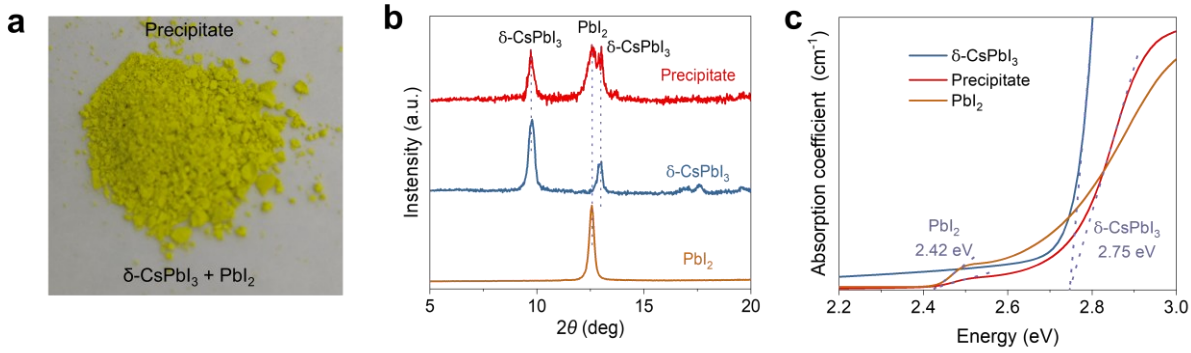

Supplementary Fig. 6 | Structural analysis of precipitate. a, Photograph of the $Cs_{0.03}FA_{0.97}PbI_3$ precipitate formed by 2-Me:DMSO solvents without DOL. **b,** XRD patterns of the precipitate, δ-$CsPbI_3$, and PbI_2. **c,** Absorption spectra of precipitates.

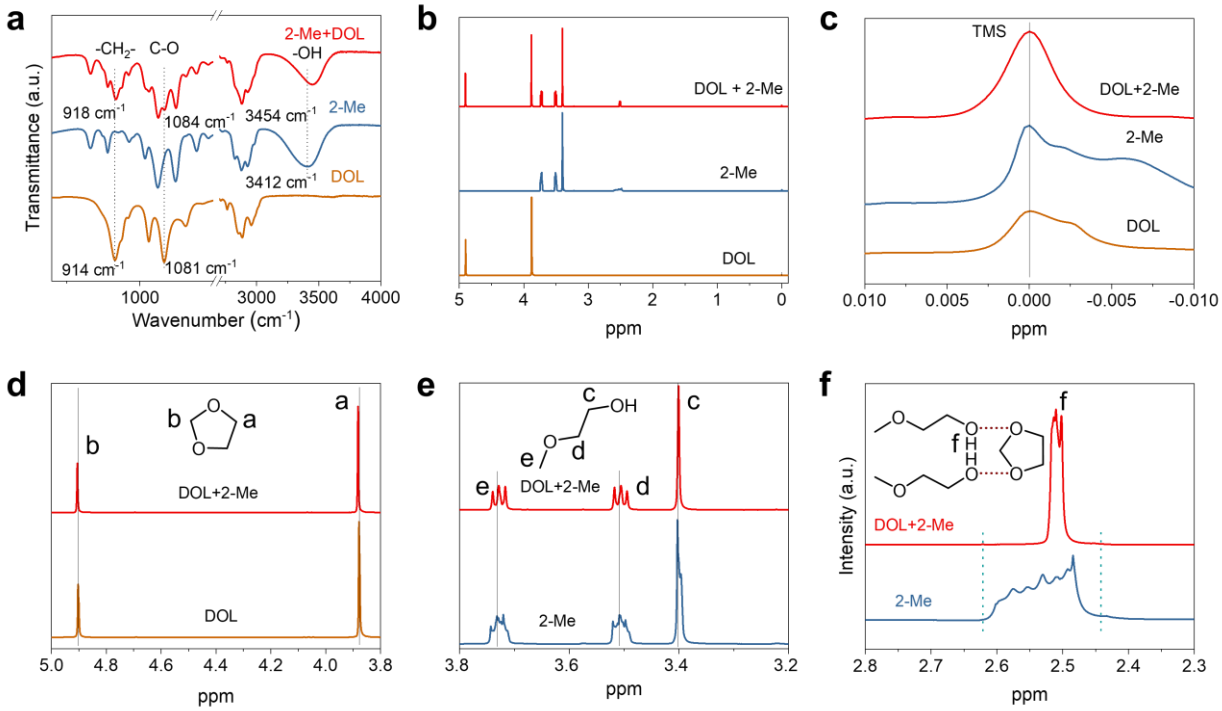

Supplementary Fig. 7 | FTIR and ^{1}H-NMR spectra of DOL, 2-Me, and DOL:2-Me. a, FTIR spectra of DOL, 2-Me, and DOL:2-Me. **b-f,** ^{1}H-NMR spectra of DOL, 2-Me, and DOL:2Me mixture. **b,** Full spectrum of ^{1}H NMR. **c,** Calibration reference (tetramethylsilane (TMS)). **d-f**, ^{1}H-NMR spectra of DOL, 2-Me and DOL:2Me. Insert is the schematic of intermolecular interaction.

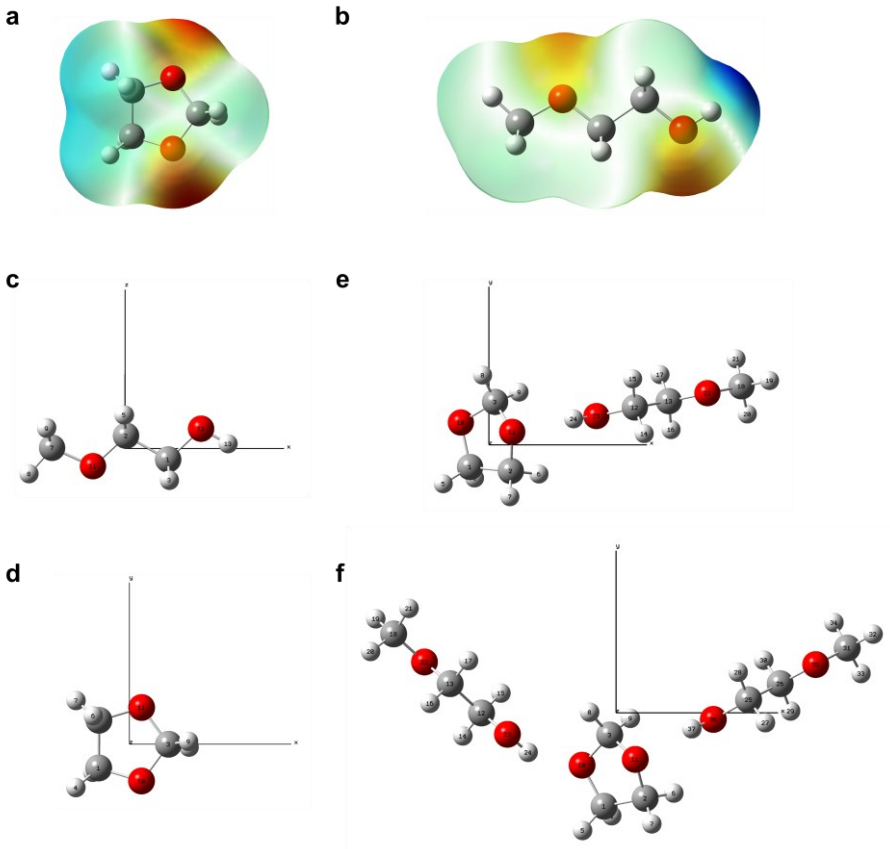

Supplementary Fig. 8 | Stable geometric configurations of 2-Me:DOL. a, Electrostatic potential (ESP) of DOL and **b,** 2-Me molecules. Gaussian 09 at the B3LYP/def2-TZVP level to simulate molecular ESP. The blue regions represent areas of positive charge concentration, which are oppositely charged to the red regions of negative charge concentration. **c,** Stable geometric configurations of 2-Me, **d,** DOL, **e,** one 2-Me molecule with one DOL molecule and **f,** two 2-Me molecules with one DOL molecule.

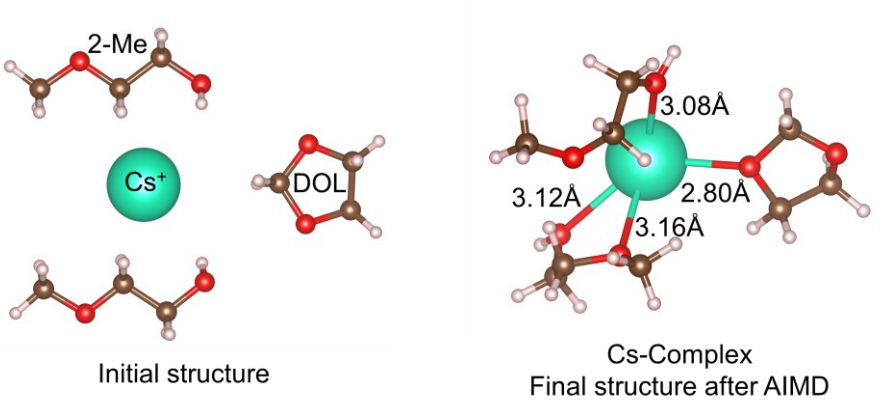

Supplementary Fig. 9 | The AIMD simulations of 2-Me, DOL, and Cs^+. Initial and final configurations of 2-Me, DOL, and Cs^+ in the AIMD simulations, spontaneously forming a Cs-complex.

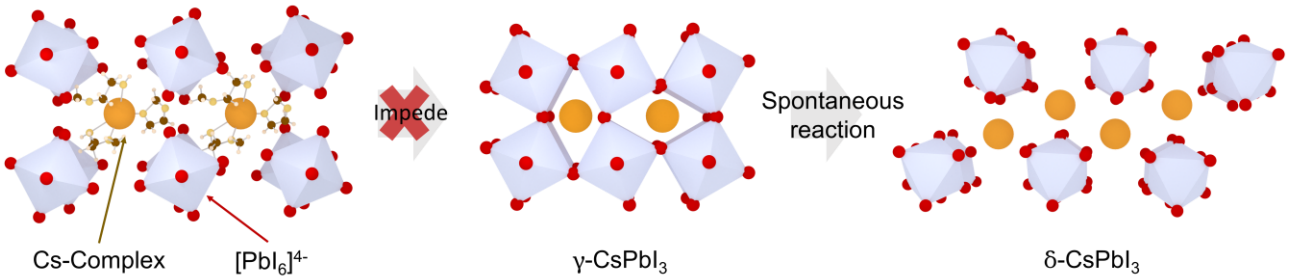

Supplementary Fig. 10 | Schematic of Cs^+ incorporation into the lattice. The schematic representation of the formation of Cs-complex inhibits the incorporation of Cs^+ into the PbI_2 lattice, thereby stabilizing the perovskite ink.

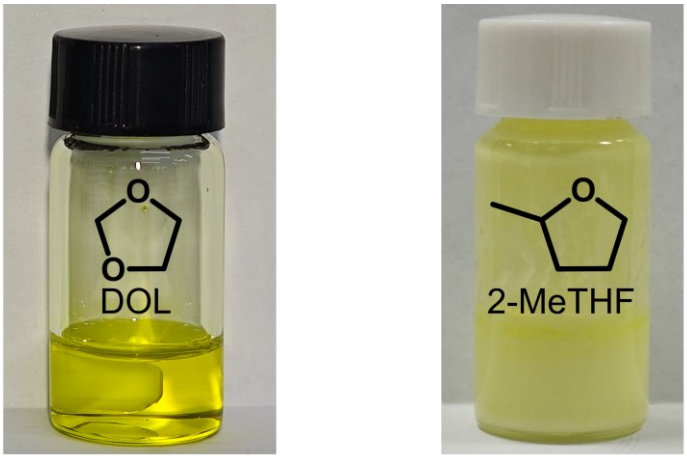

Supplementary Fig. 11 | The digital photos of the perovskite inks. DOL acts as a co-solvent to enhance solubility, whereas the ink remains turbid even after adding 2-MeTHF to the 2-Me:DMSO mixed solution.

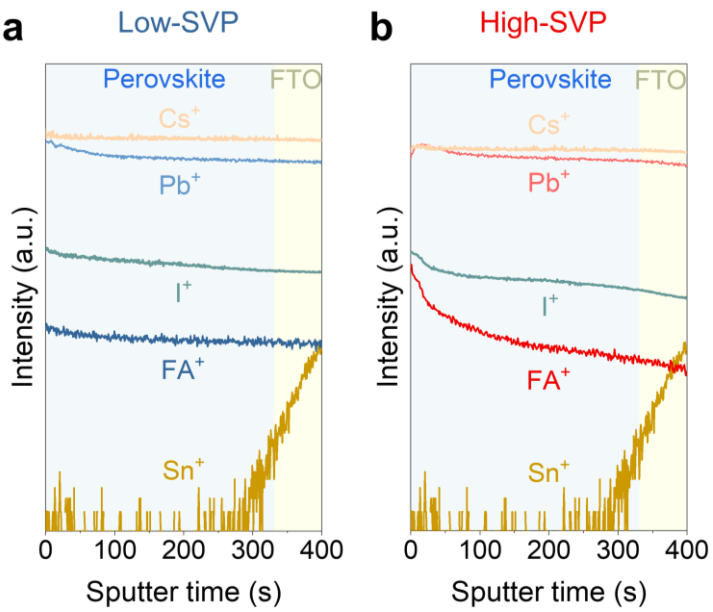

Supplementary Fig. 12 | TOF-SIMS depth profile of the perovskite films. a, Low-SVP perovskite, **b,** High-SVP perovskite.

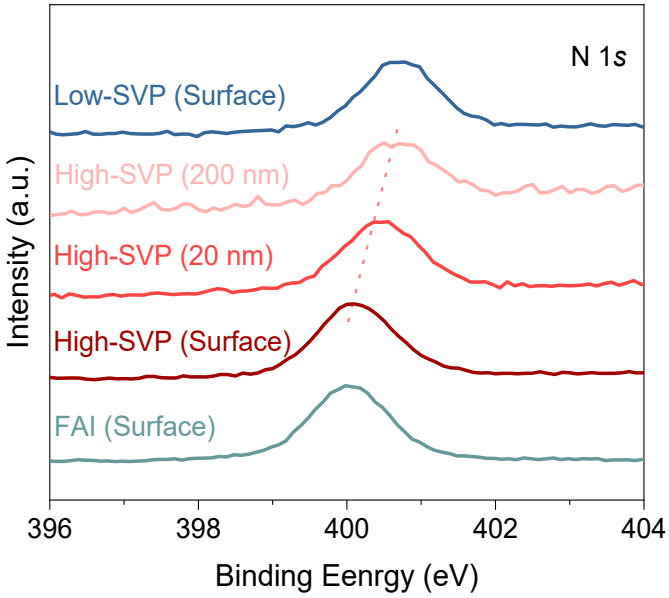

Supplementary Fig. 13 | The XPS spectra of N 1*s*. N 1*s* XPS spectra of FAI powder and perovskite films fabricated using low-SVP and high-SVP solvents. Measurements for FAI and the low-SVP perovskite were confined to the top surface, while those for the high-SVP perovskite included the top surface and depths of 20 nm and 200 nm.

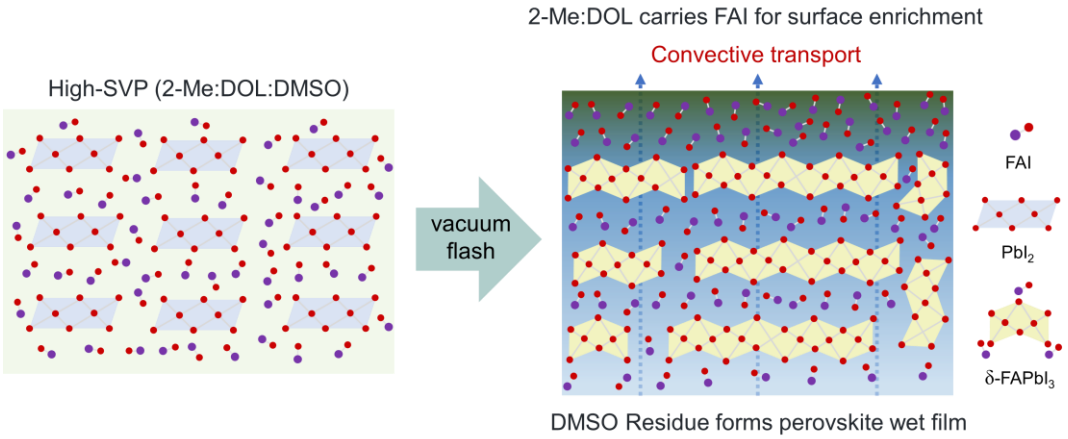

Supplementary Fig. 14 | The schematic illustration of the dynamic process of the surface enrichment of FAI during VCD processing. The high SVP characteristic of 2-Me induces its rapid evaporation under vacuum conditions. This establishes a steep concentration gradient and intense Marangoni flow, thereby driving the migration of FAI toward the liquid–air interface. Owing to the kinetic trapping effect during rapid solvent removal (where the solvent evaporation rate far exceeds the solute diffusion rate, causing FAI transported to the interface to be trapped by the rapidly forming solid perovskite matrix before redistributing into the bulk), FAI species are preferentially accumulated and stabilized at the perovskite surface, ultimately forming an FAI-enriched termination layer.

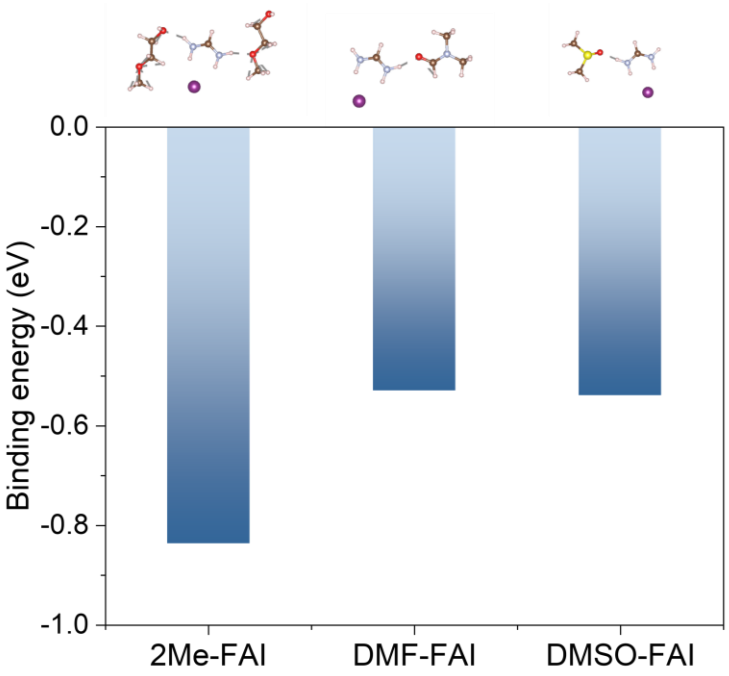

Supplementary Fig. 15 | Binding energy calculations of FAI and solvents. The 2-Me exhibits a higher binding energy with FAI compared to DMF or DMSO. This indicates a stronger interaction between 2-Me and FAI, suggesting that 2-Me forms more favorable associations with FAI species.

Supplementary Note 2:

PV modules fabrication

The fabrication process for the perovskite modules is illustrated in Supplementary Fig. 16, where FTO is fluorine-doped tin oxide, NiO_x is nickel oxide, C_{60} is fullerene, ALD-SnO_2 is atomic layer deposited tin oxide, IZO is indium zinc oxide. Commercial-sized perovskite modules (1.2 m by 0.6 m) were produced on a 150 MW pilot line, following the same processing steps as those established for the 30 cm by 40 cm sub-modules.

First, P1 lines were scribed on a fluorine-doped tin oxide (FTO) glass substrate (30 cm by 40 cm) using a HAN'S LASER system. The substrate was then ultrasonically cleaned sequentially in detergent, deionized water, and isopropanol (IPA), each for 20 minutes. A NiO_x hole-transport layer was subsequently deposited on the cleaned substrate by magnetron sputtering. In ambient air, the perovskite layer was deposited onto the glass/FTO/NiO_x stack via slot-die coating.

For perovskite deposition, the gap between the slot-die coater and the substrate was set to 50 μm, and the coating speed was maintained at 15 mm/s. Immediately after coating, the wet film was transferred to a vacuum-chamber drying (VCD) system, where it was dried for 35 s under a vacuum below 10 Pa. The film was then annealed on a hot plate at 130 °C for 20 min. Prior to slot-die coating, both the ammonium halides passivator (AHP) and lead carboxylates passivator (LCP) solutions were prepared by dissolving the respective materials in IPA.

Next, a 20-nm-thick C_{60} layer was thermally evaporated onto the perovskite film at a rate of 1 Å/s. Approximately 15 nm of SnO_2 was deposited by atomic layer deposition (ALD), followed by the magnetron sputtering of an 80-nm-thick IZO layer. P2 lines were then scribed using the HAN'S LASER system, after which 100-nm-thick Cu electrodes were deposited by magnetron sputtering. P3 lines were scribed with the same laser parameters as those used for P2.

A busbar was attached to the metal electrodes to facilitate electrical testing. The module edges were sealed with butyl rubber, and a polyolefin elastomer (POE) encapsulation film was applied over the active area. A glass cover of the same dimensions as the substrate was placed on top of the butyl rubber and POE stack. The assembly was laminated at 130 °C for 10 minutes. Following lamination, the perovskite solar module was ready for stability testing. Finally, a junction box was installed to enable series interconnection with adjacent modules, forming a panel suitable for photovoltaic power-station deployment.

A complete perovskite solar module comprises a multilayer stack, as schematically illustrated in Supplementary Fig. 17. Supplementary Fig. 18 also provides cross-sectional schematics of the monolithic interconnection structures defined by the P1, P2, and P3 laser scribes. The widths of the P1, P2, and P3 lines are approximately 29 μm, 69 μm, and 53 μm, respectively, resulting in a dead

area width of 158 μm from P1 to P3 (Supplementary Fig. 19). Specifically, the P1 scribe completely isolates the underlying FTO substrate (Supplementary Fig. 20a), while the P2 scribe penetrates through the perovskite layer to make contact with the FTO (Supplementary Fig. 20b). The P3 scribe is terminated at the perovskite surface to isolate the top electrode (Supplementary Fig. 20c). Notably, microscopic curling of the Cu electrode was observed within the P3 scribe lines during the laser process. Furthermore, a cross-sectional SEM image of the fully fabricated module is presented in Supplementary Fig. 20d, confirming the final device architecture of FTO/NiO_x/perovskite/passivator/C_{60}/ALD-SnO_2/IZO/Cu.

To date, the state-of-the-art architecture typically adopts a TCO/NiO_x/self-assembled monolayer (SAM) or TCO/SAM configuration, in which the SAM is regarded as an essential hole-selective layer for achieving higher-performance perovskite solar cells (p-i-n structure). To further enhance module performance, we also attempted to incorporate SAMs during large-area fabrication. Specifically, we introduced the most commonly used SAM material, (4-(3,6-dimethyl-9H-carbazol-9-yl)butyl)phosphonic acid (Me-4PACz), to construct FTO/NiO_x/SAM and FTO/SAM bottom hole-transport structures. Based on the low-SVP solvent system, perovskite modules with an active area of 810 cm^2 were fabricated following the aforementioned process. As shown in Supplementary Fig. 21, compared with the FTO/NiO_x/perovskite configuration, both the FTO/NiO_x/SAM/perovskite and FTO/SAM/perovskite architectures resulted in lower module efficiencies, primarily reflected in reduced open-circuit voltage (V_{OC}) and fill factor (FF). We attribute this to incomplete coverage and localized disordered stacking of the SAM during large-area slot-die coating, which leads to uneven energy level distribution at the interface and severely impedes efficient charge carrier transport. Due to the critical constraints imposed by uniformity and stability, we excluded SAMs from consideration as the hole transport layer. But adapting SAM materials for commercial perovskite modules to achieve superior photovoltaic performance remains a highly worthwhile research topic. Although our preliminary attempts did not yield effective integration, we will continue to explore this direction in future studies.

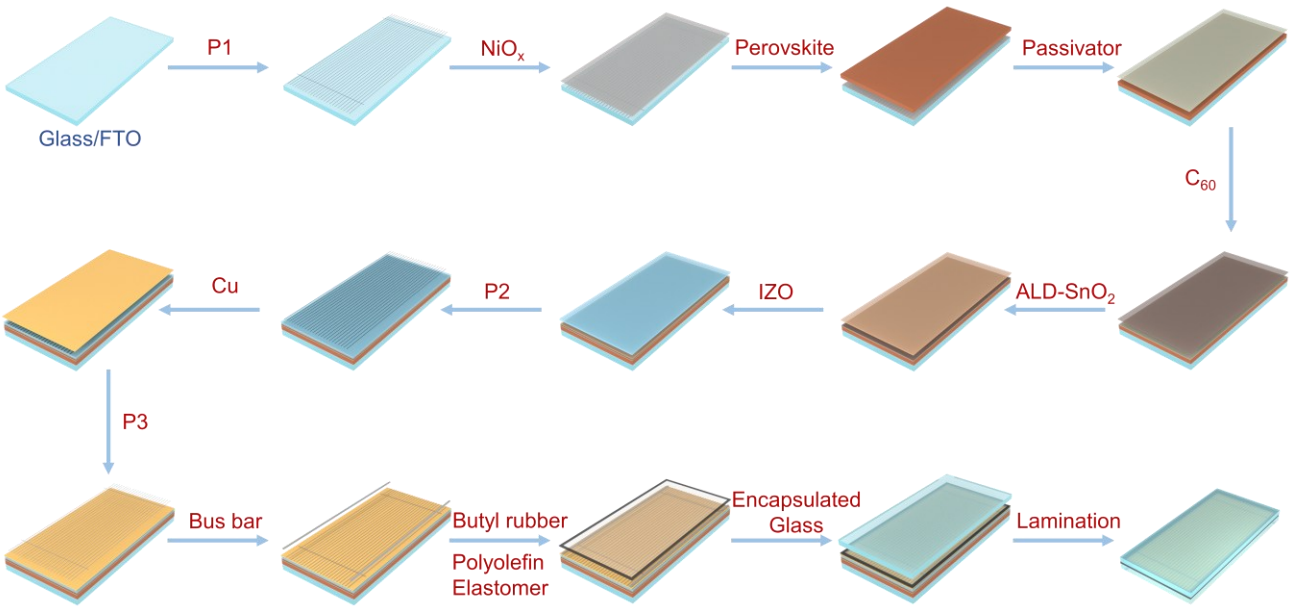

Supplementary Fig. 16 | Process flow diagram for the fabrication of PV modules.

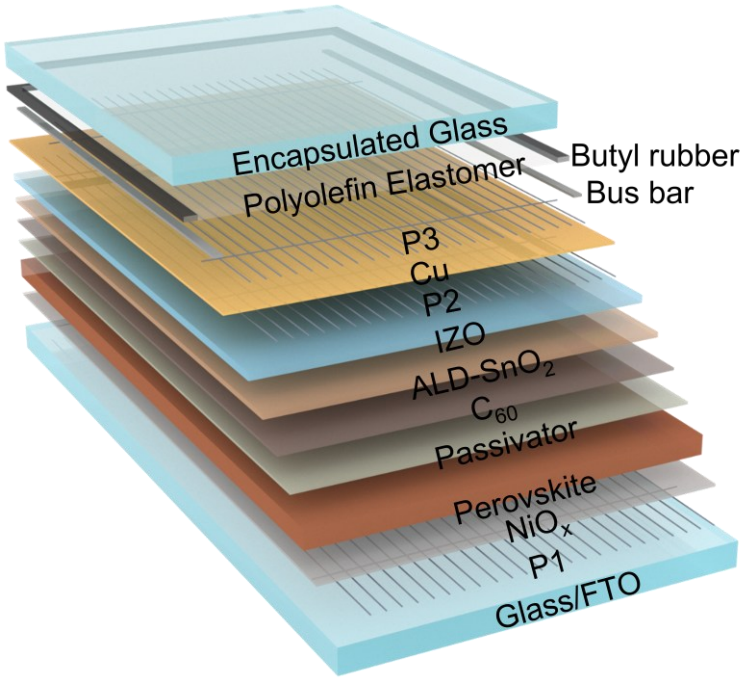

Supplementary Fig. 17 | Configuration diagram of perovskite solar modules.

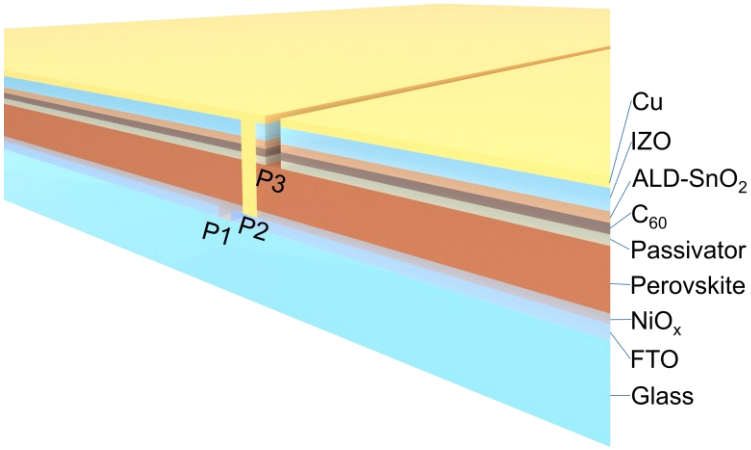

Supplementary Fig. 18 | Cross-sectional schematic of a perovskite solar module showing the P1, P2, and P3 interconnect structures.

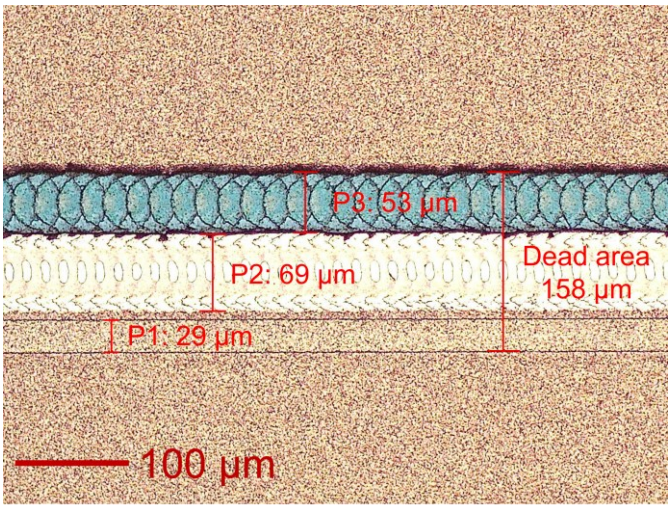

Supplementary Fig. 19 | Microscopic characterization of perovskite solar modules. Optical microscopy image of P1, P2, and P3.

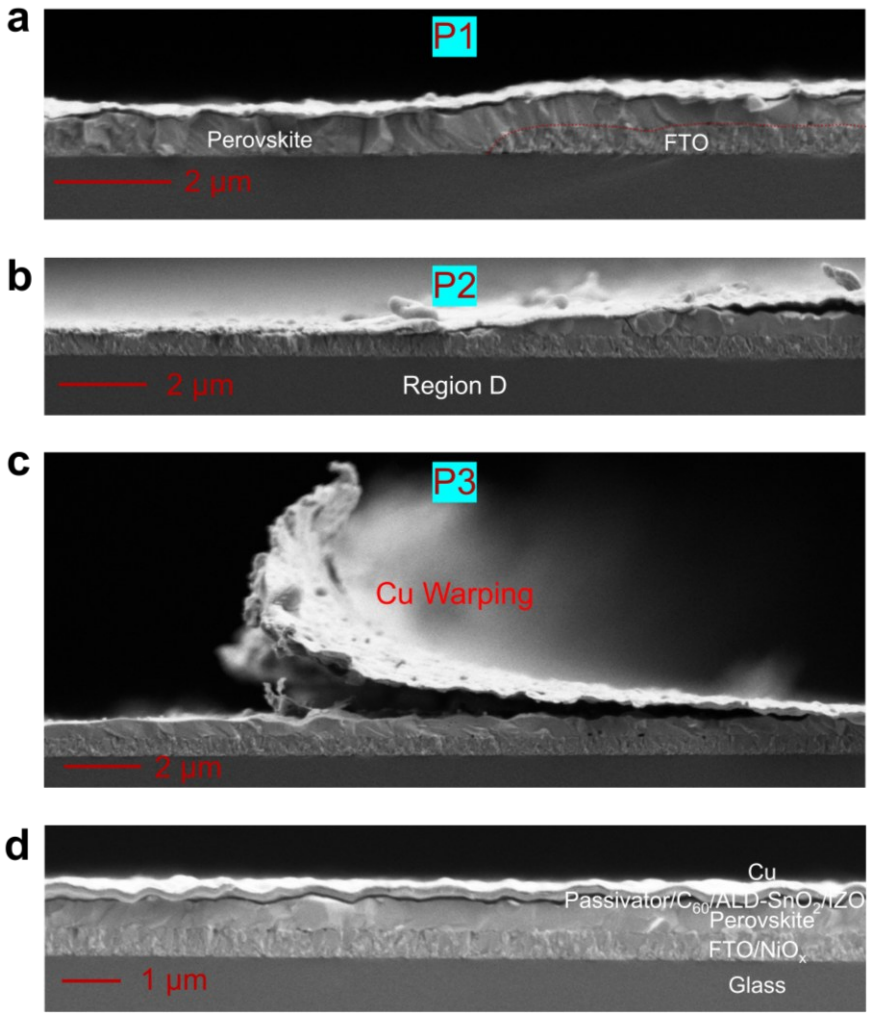

Supplementary Fig. 20 | Microscopic characterization of perovskite solar modules. a-c, SEM cross-sections showing the P1, P2, and P3 interconnects, respectively. **d,** SEM cross-section of the complete module.

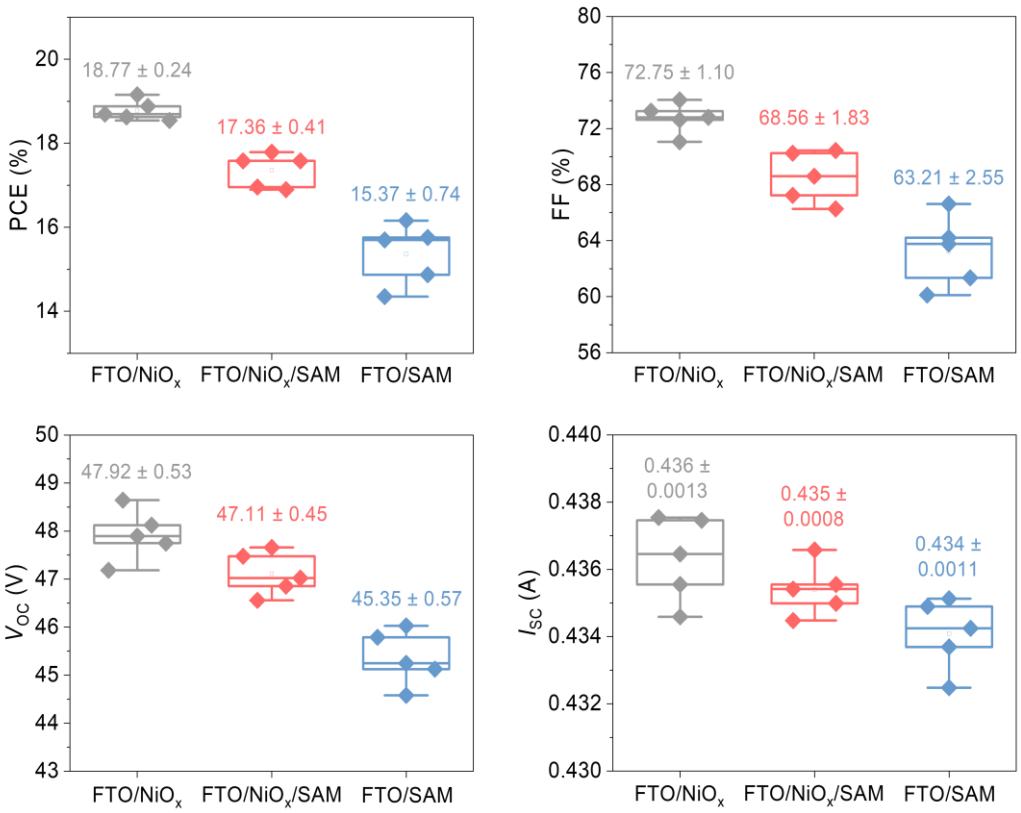

Supplementary Fig. 21 | Statistical photovoltaic parameters of the modules. Perovskite films were fabricated using a low-SVP solvent (DMF:DMSO = 9:1), and none of the modules underwent top-surface passivation. FTO/NiO_x, FTO/NiO_x/SAM, and FTO/SAM denote three different substrates for perovskite coating. The SAM material was dissolved in isopropyl alcohol at a concentration of 0.5 mg mL^{-1}, subsequently deposited by slot-die coating, and annealed on a hot plate at 110 °C for 10 min. The active area of module is 810 cm^2. Five parallel data sets were taken for each set of conditions. Scatters represent raw data; boxplots show the interquartile range with the median as the center line; whiskers indicate the 5th–95th percentiles. Numerical data are presented as mean ± SD.

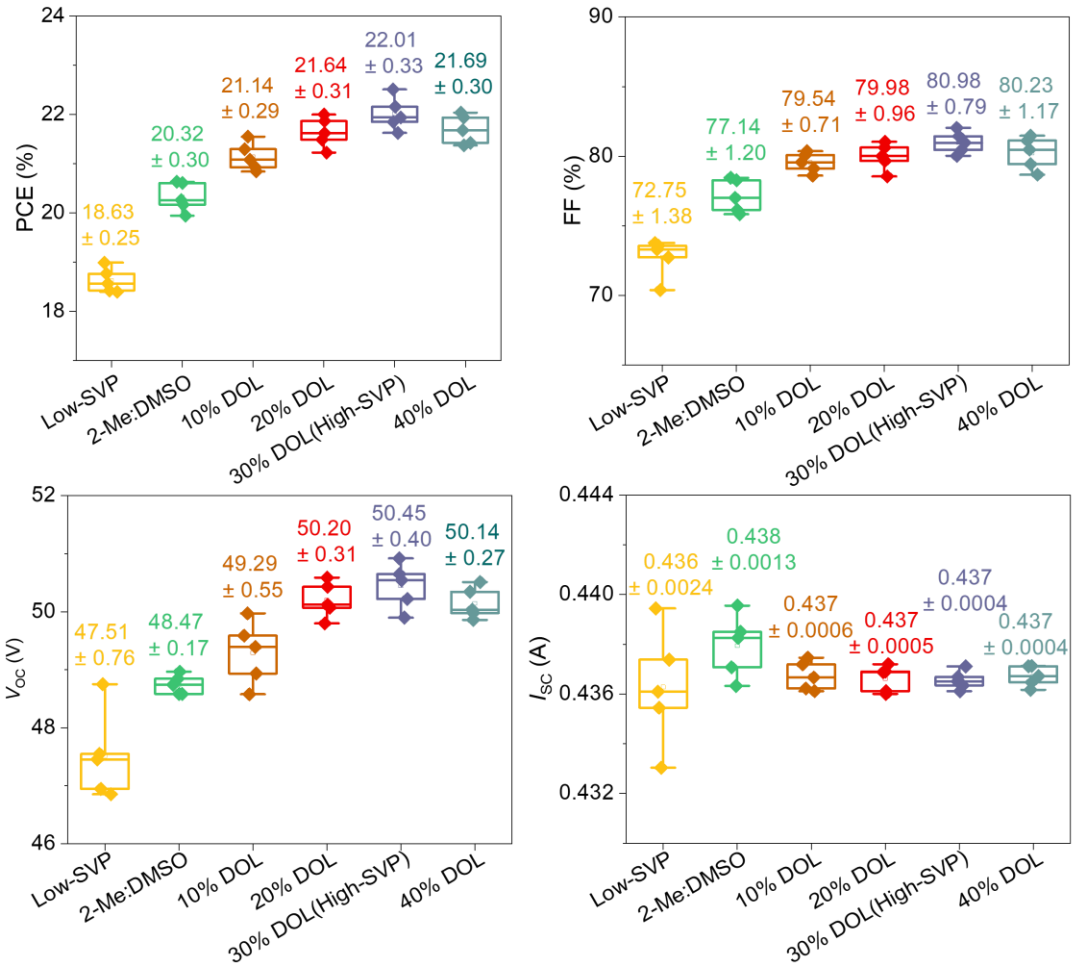

Supplementary Fig. 22 | Statistical photovoltaic parameters of the modules made by perovskites prepared in different solvent systems without passivation. A ***DMF:DMSO = 9:1*** mixture is referred to as ***low-SVP***; a 2-Me:DMSO = 9:1 mixture is referred to as 2-Me:DMSO; when the mixture ratios of 2-Me:DOL:DMSO are set to 8:1:1, 7:2:1, 6:3:1, and 5:4:1, they correspond to DOL contents of 10%, 20%, 30%, and 40%, respectively. Among these, the ***2-Me:DOL:DMSO = 6:3:1*** ratio is defined as the ***high-SVP***. The active area of module is 810 cm^2. Five parallel data sets were taken for each set of conditions. Scatters represent raw data; boxplots show the interquartile range with the median as the center line; whiskers indicate the 5th–95th percentiles. Numerical data are presented as mean ± SD.

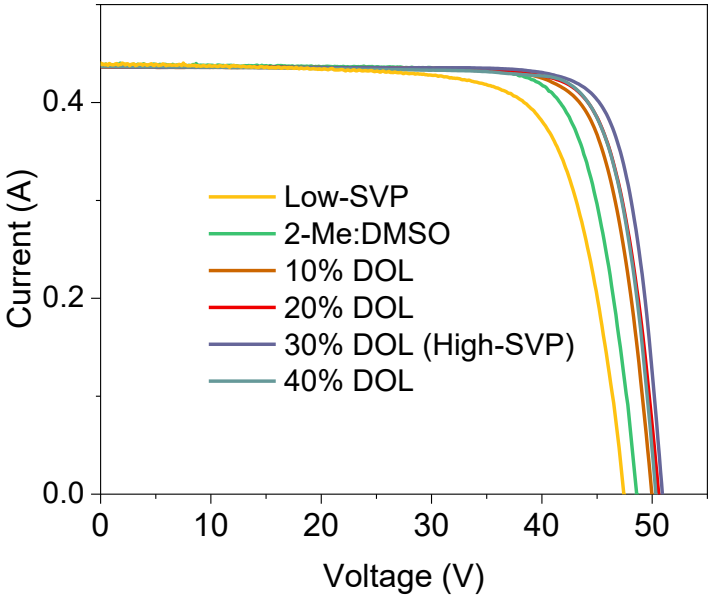

Supplementary Fig. 23 | *I-V* curves of the optimal modules. The PV modules made by perovskites prepared in different solvent systems and without passivation (the optimal efficiency derived from the statistical data in Supplementary Fig. 22).

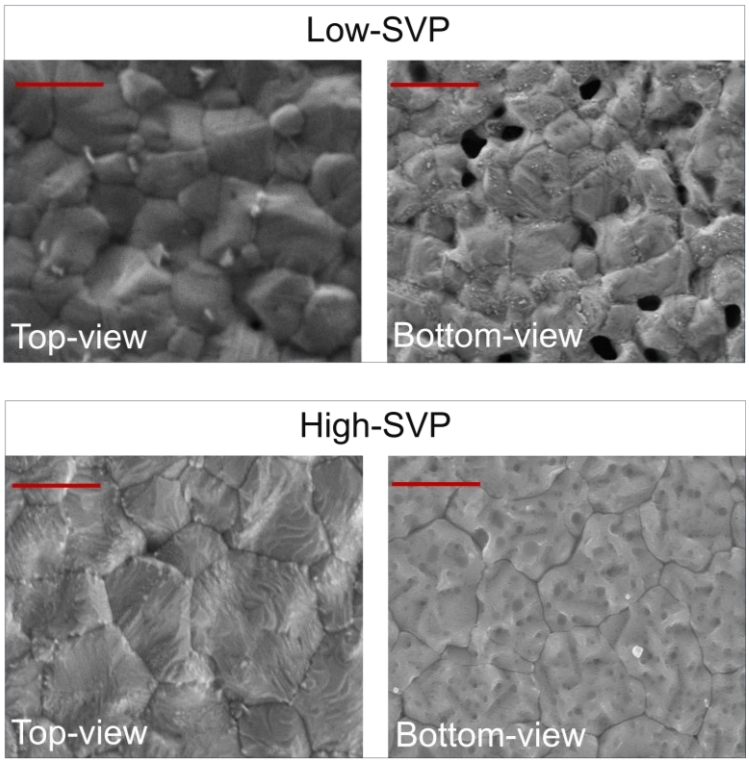

Supplementary Fig. 24 | SEM images of perovskite films. The top-view and bottom-view SEM images of perovskite films prepared with low-SVP of DMF:DMSO and high-SVP solvents of 2-Me:DOL:DMSO. After bonding the glass and perovskite film using UV-curing adhesive, the perovskite is peeled off from the FTO substrate, exposing the bottom interface of the perovskite for testing. The scale bars correspond to 500 nm in all images.

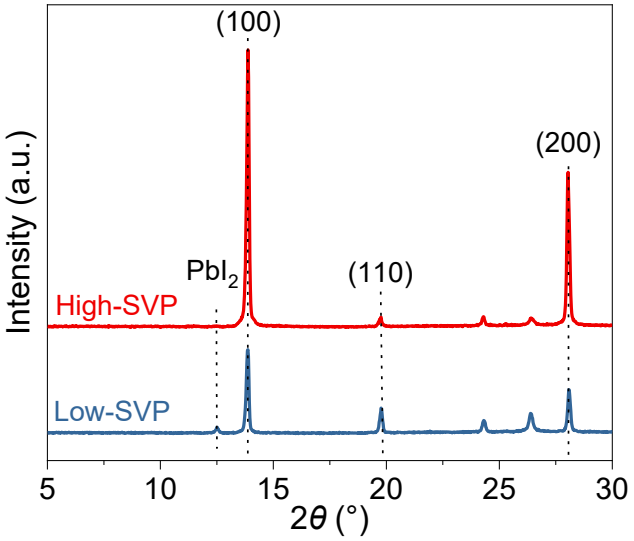

Supplementary Fig. 25 | XRD patterns of the perovskite films. The films prepared by low-SVP of DMF:DMSO and high-SVP solvents of 2-Me:DOL:DMSO.

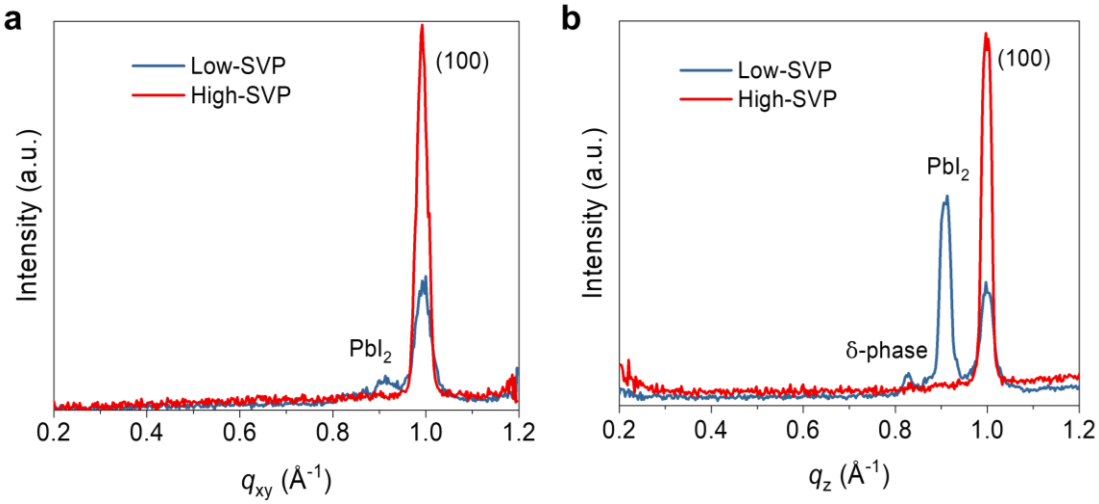

Supplementary Fig. 26 | GIWAXS intensity profiles. The low-SVP and high-SVP perovskite films along the **a,** in-plane and **b,** out-of-plane directions.

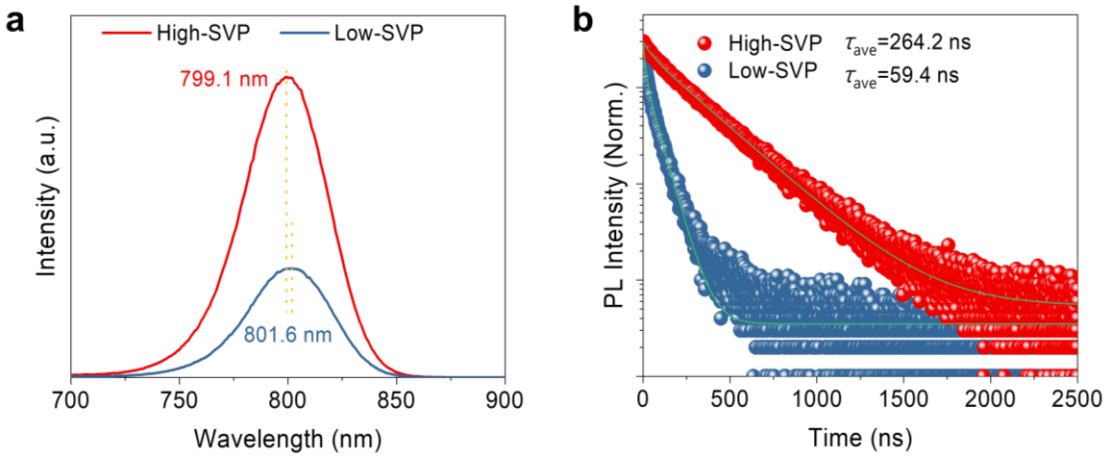

Supplementary Fig. 27 | Steady PL spectra and TRPL curves of perovskite films fabricated using low-SVP and high-SVP solvents. The slight redshift observed in the PL peak of Cs-formed perovskite films may be caused by the higher concentration of PbI_2 at the perovskite surface and the excessively high density of defect states.

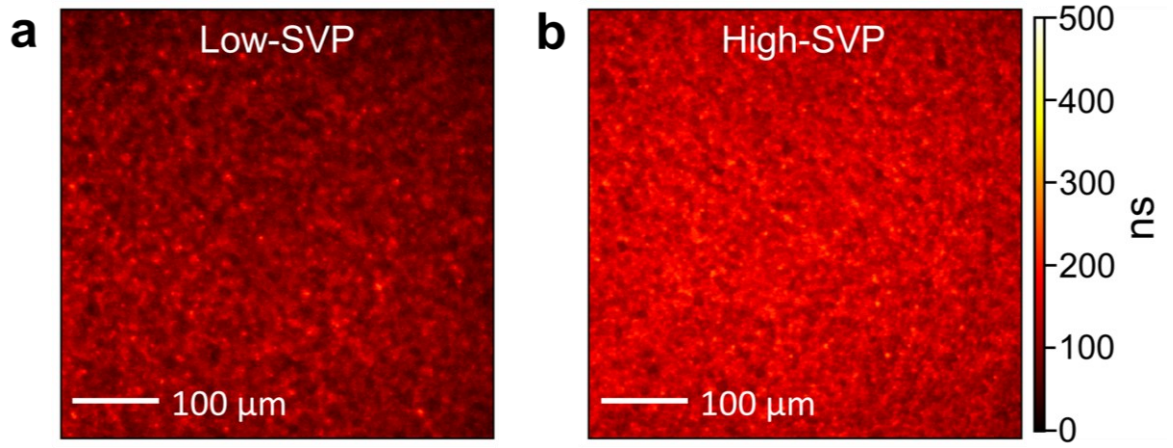

Supplementary Fig. 28 | The carrier lifetime mappings of perovskite films. a, low-SVP and **b,** high-SVP solvent-fabricated perovskite films.

Supplementary Note 3:

The performance of excess FAI in the low-SVP perovskite system.

To clarify that simply increasing the FAI content in the precursor is not a viable route for achieving high-performance modules, and to further highlight the necessity and superiority of our proposed method, we prepared low-SVP perovskite inks with 2%, 4%, and 6% excess FAI (molar ratio). Microscopically, excess FAI leads to larger and denser perovskite grains (Supplementary Fig. 29). However, XRD characterization reveals that excess FAI alters the crystallization orientation, exhibiting a progressively stronger (110) preferred orientation as the FAI content increases. Moreover, at 6% excess, the formation of the photo-inactive δ-$FAPbI_3$ phase is observed (Supplementary Fig. 30), which is detrimental to device performance. Consequently, we fabricated perovskite modules (810 cm^2) based on these compositions (Supplementary Fig. 31). A clear trend of declining efficiency is observed with increasing FAI excess, primarily manifested as a reduction in V_{OC} and FF, a result consistent with the XRD findings.

The perovskite module production line operates under ambient conditions with 30–40% RH. As outlined in Supplementary Note 2, the process from film coating to encapsulation and testing for a single module can be completed within a short timeframe, during which the perovskite film is exposed to air for a limited duration (typically <2 h). Owing to the low ambient humidity, brief exposure, and the protective effect of consecutively deposited functional layers (C_{60}, ALD-SnO_2, IZO, Cu), we observed no visible phase degradation of the perovskite films during the production process. However, when different perovskite films were placed in a flowing air environment with 60–70% RH, distinct stability variations emerged within just 1 h (Supplementary Fig. 32). Specifically, the low-SVP and 2% excess FAI perovskite films showed no significant visual change, whereas films with 4% and 6% excess FAI exhibited pronounced phase degradation. The degree of phase instability increased with higher FAI content. XRD results confirm that this degradation process involves the facile transformation of excess-FAI perovskite films from the photoactive α-$FAPbI_3$ phase to the non-photovoltaic-active δ-$FAPbI_3$ phase under humid conditions.

In summary, merely introducing excess FAI is insufficient to achieve high-performance perovskite modules. Furthermore, its inherent instability under ambient conditions severely restricts the viability of this approach for large-scale atmospheric-environment manufacturing.

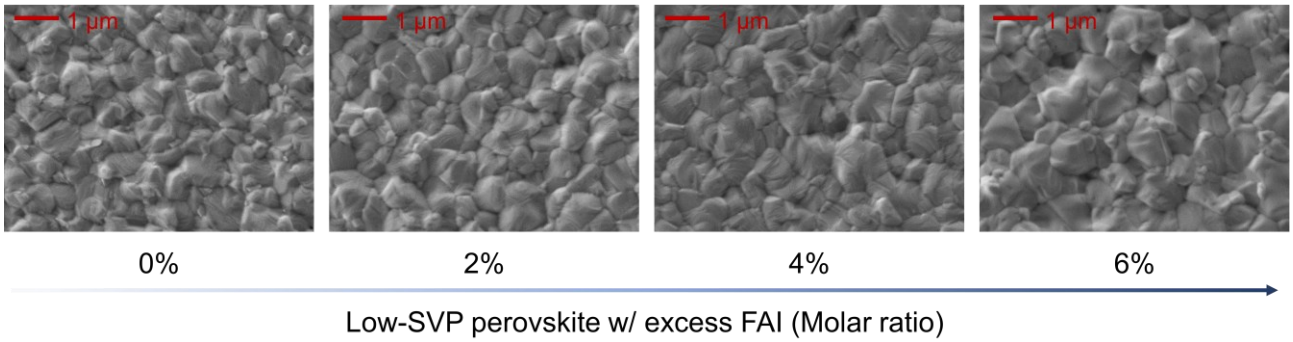

Supplementary Fig. 29 | Top-view SEM images of perovskite films. Perovskite film surfaces with varying excess FAI content.

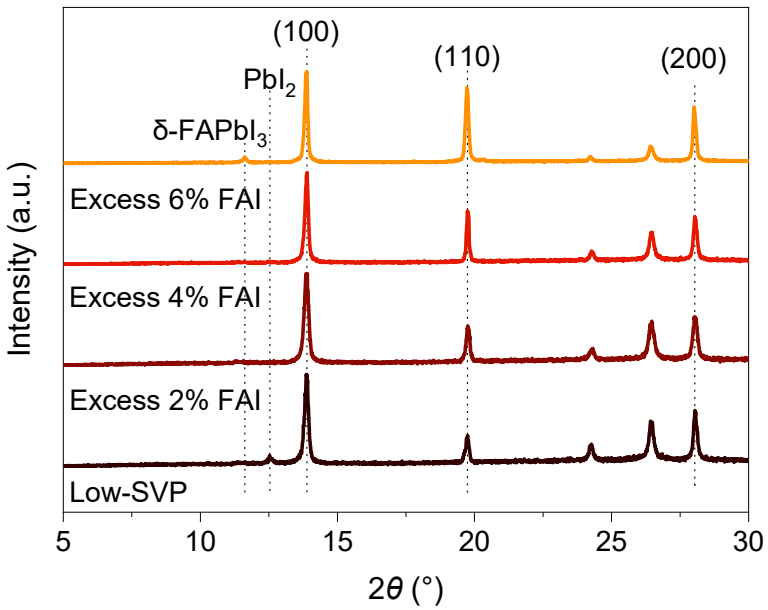

Supplementary Fig. 30 | XRD patterns of perovskite films. XRD patterns of the freshly prepared perovskite films, as shown in Supplementary Fig. 29.

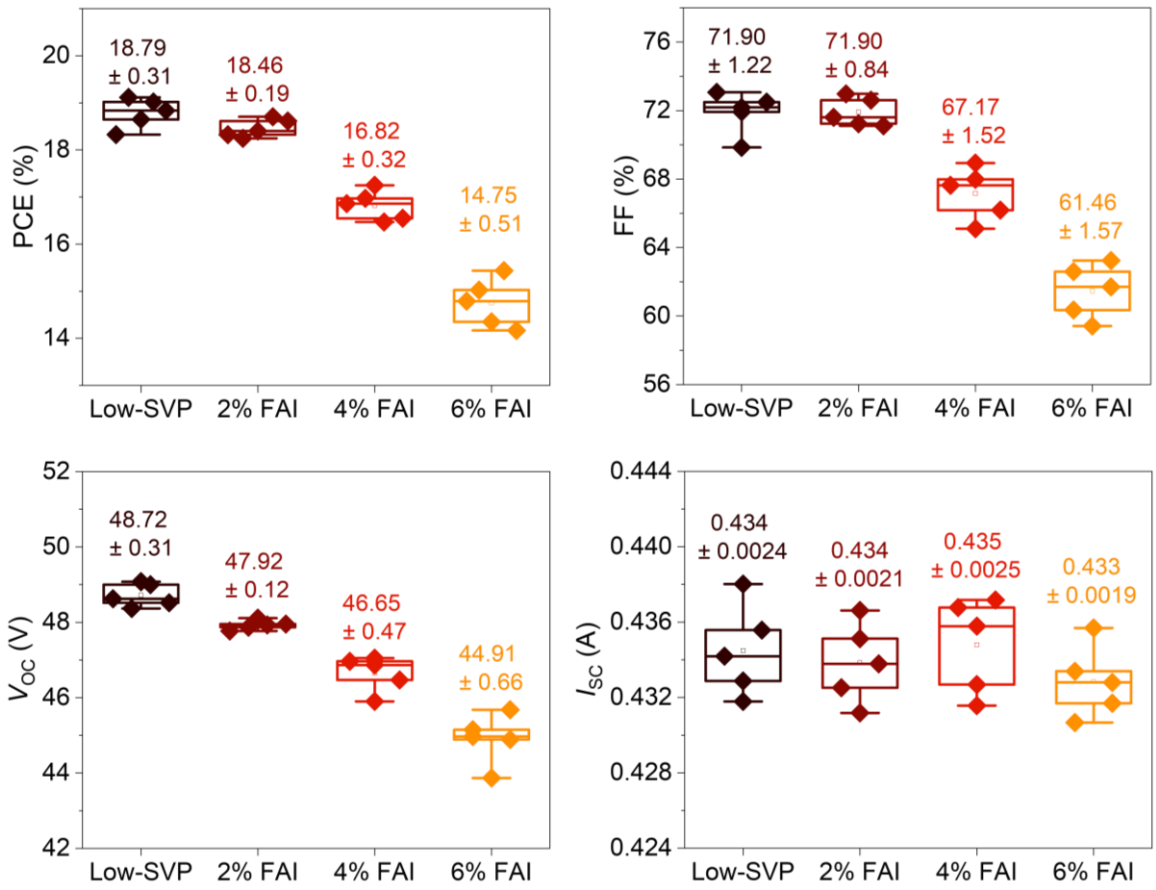

Supplementary Fig. 31 | Statistical photovoltaic parameters of the modules. The PV modules fabricated by low-SVP perovskite films with excess FAI. The aperture area of the module is 810 cm^2. Five parallel data sets were taken for each set of conditions. Scatters represent raw data; boxplots show the interquartile range with the median as the center line; whiskers indicate the 5th–95th percentiles. Numerical data are presented as mean ± SD.

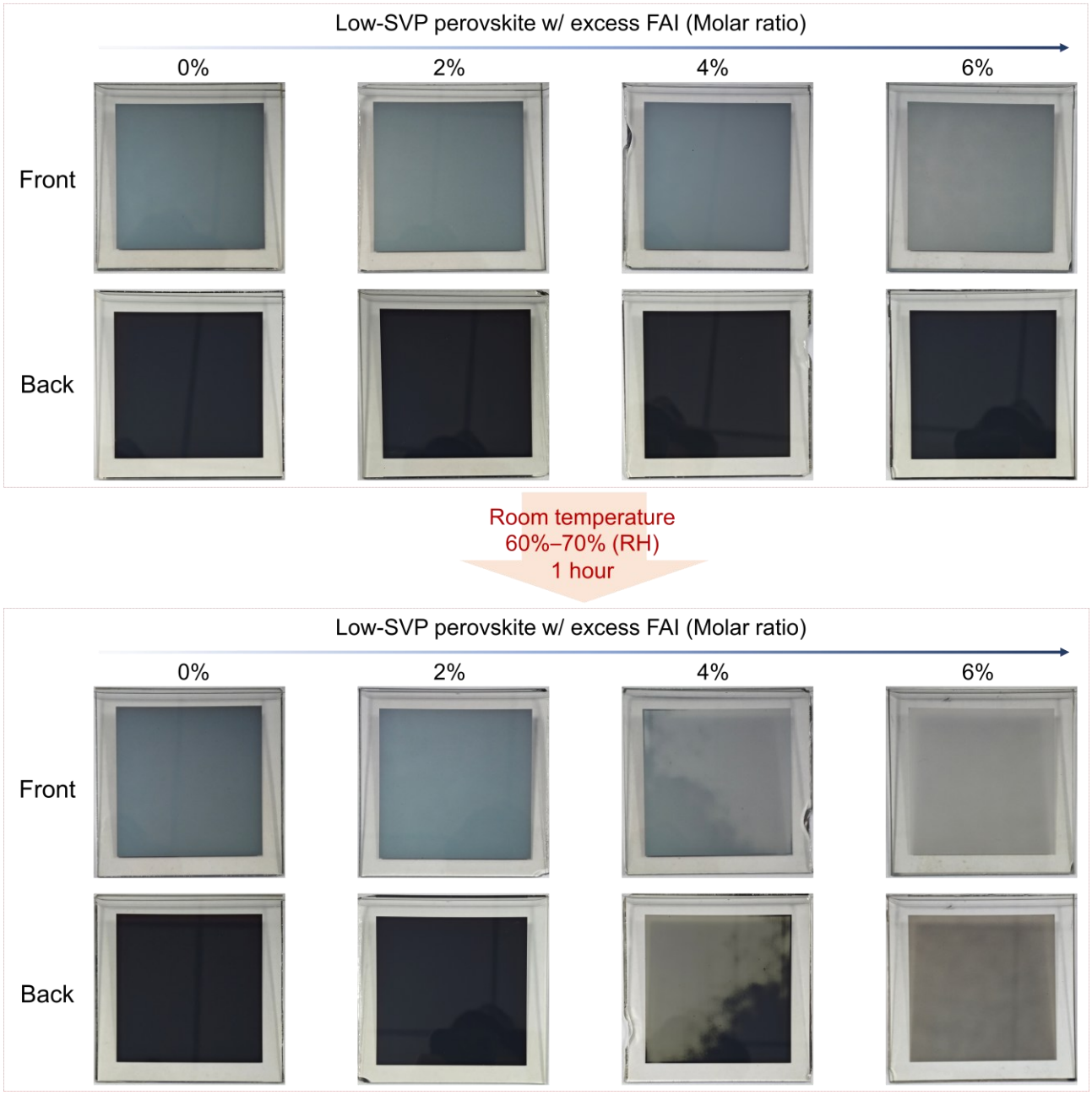

Supplementary Fig. 32 | Photographs of perovskite films before and after aging. Demonstrating the moisture stability of films with 0%, 2%, 4%, and 6% excess FAI (molar ratio) after exposure to 60–70% RH for 1 h.

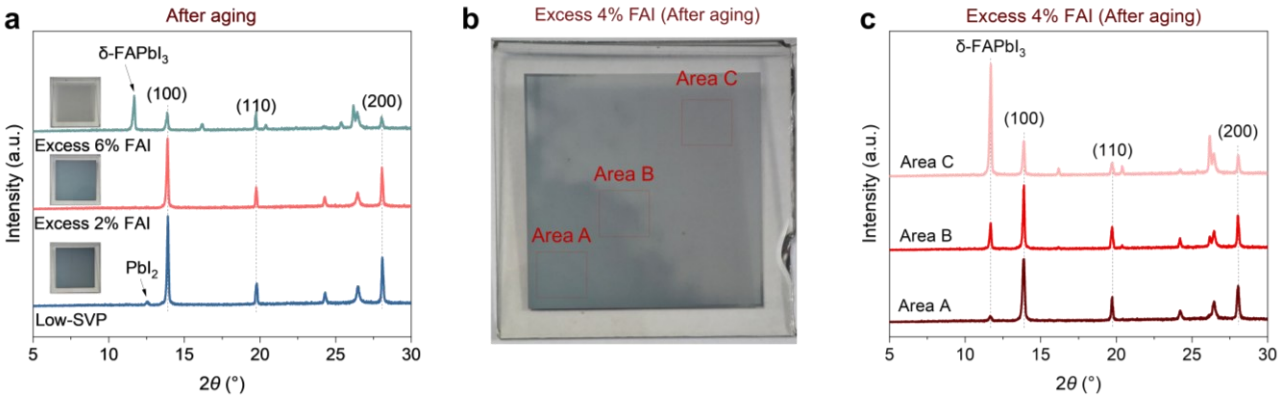

Supplementary Fig. 33 | The XRD patterns of perovskite films after aging (conditions shown in Supplementary Fig 32). a, XRD patterns of low-SVP films with 0%, 2%, and 6% excess FAI after aging. **b,** Photograph of the aged perovskite film with 4% excess FAI, divided into three regions exhibiting different degrees of decomposition (Area A, B, and C). **c,** Corresponding XRD patterns of the distinct regions (A, B, C) from the aged film with 4% excess FAI, as defined in panel b.

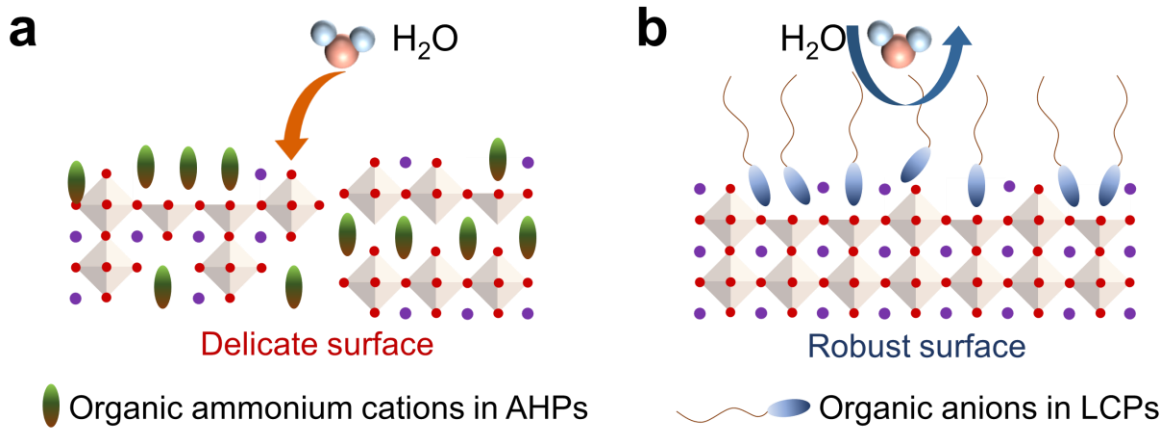

Supplementary Fig. 34 | Schematic illustration of surface states for different perovskites following passivation treatments. a, The delicate surface formed on a PbI_2-enriched surface under AHPs treatment. **b,** The robust surface formed on a FAI-enriched surface under LCPs treatment.

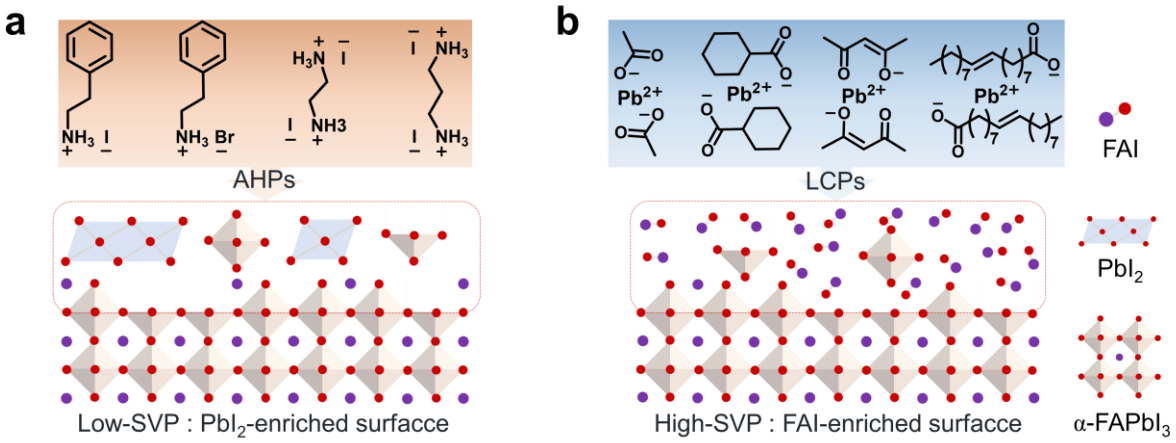

Supplementary Fig. 35 | Schematic illustration of different perovskite surface states and corresponding passivators. a, PbI_2-enriched surface formed by low-SVP solvents and the corresponding AHPs. **b,** FAI-enriched surface formed by high-SVP solvents and the corresponding LCPs.

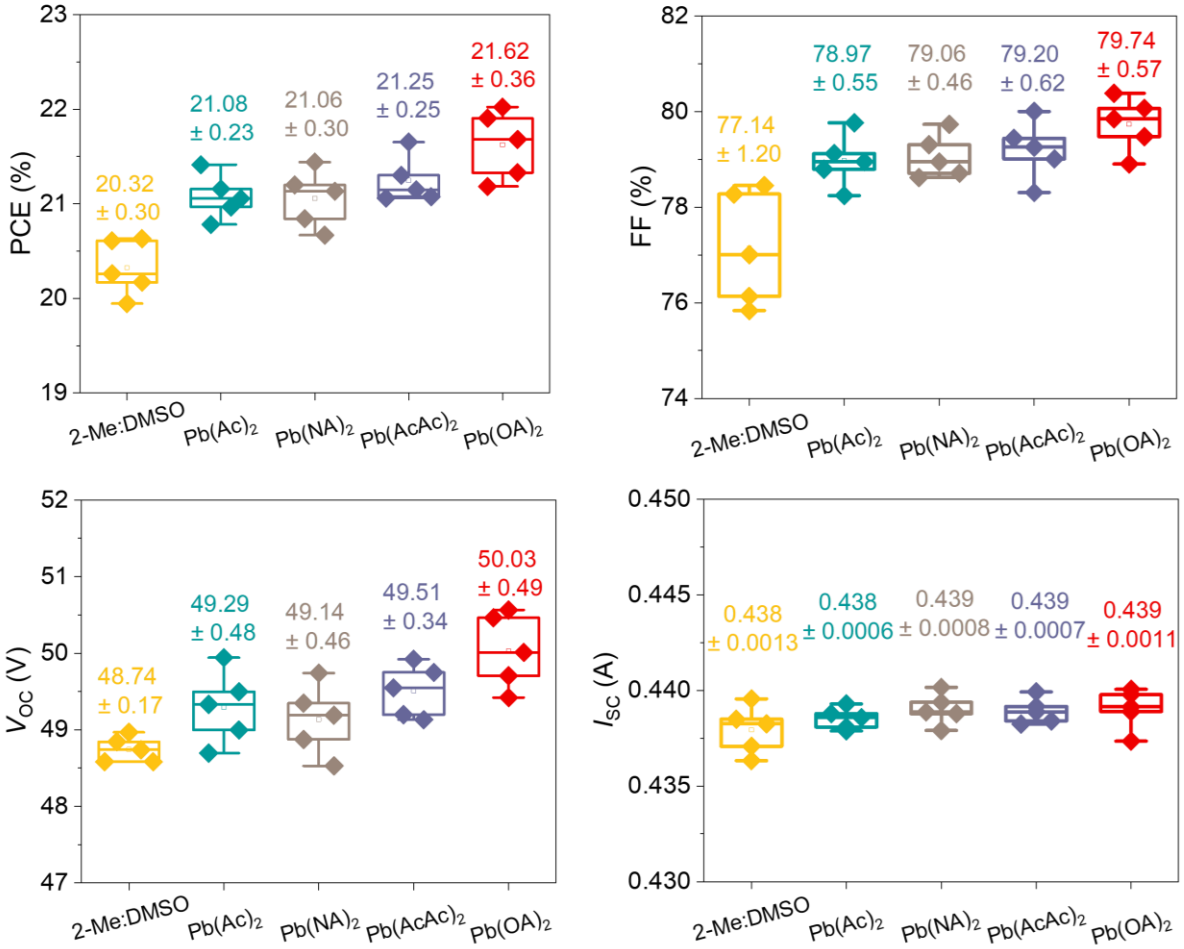

Supplementary Fig. 36 | Statistical photovoltaic parameters of the modules. The PV modules fabricated by 2-Me:DMSO perovskite films (2-Me:DMSO = 9:1 mixture is referred to as 2-Me:DMSO) with different lead carboxylates surface passivation. Corresponding passivator of lead carboxylates are $Pb(Ac)_2$, $Pb(NA)_2$, $Pb(AcAc)_2$ and $Pb(OA)_2$. The concentration of passivator is 1.5 mg mL^{-1} and the aperture area of the module is 810 cm^2. Five parallel data sets were taken for each set of conditions. Scatters represent raw data; boxplots show the interquartile range with the median as the center line; whiskers indicate the 5th–95th percentiles. Numerical data are presented as mean ± SD.

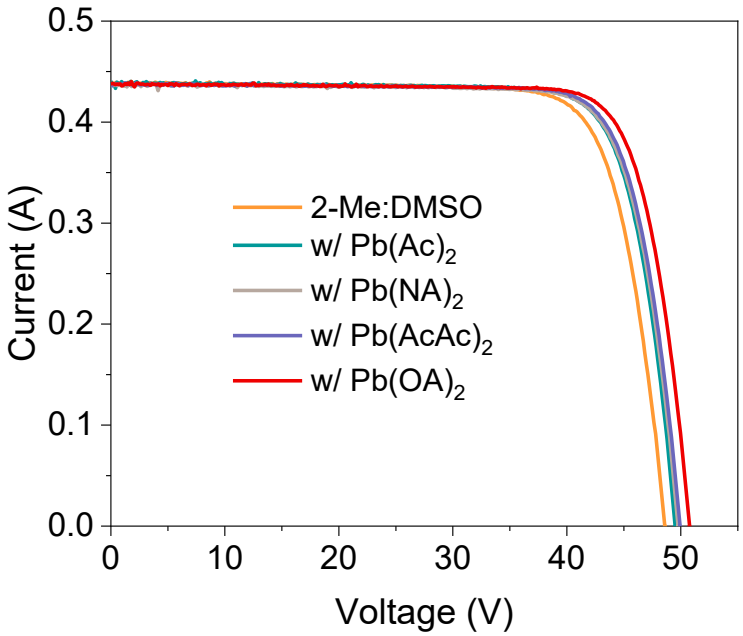

Supplementary Fig. 37 | *I-V* curves of the optimal modules. The PV modules fabricated from 2-Me:DMSO solvent (2-Me:DMSO = 9:1 mixture is referred to as 2-Me:DMSO) with different lead carboxylates surface passivation (the optimal efficiency derived from the statistical data in Supplementary Fig. 36).

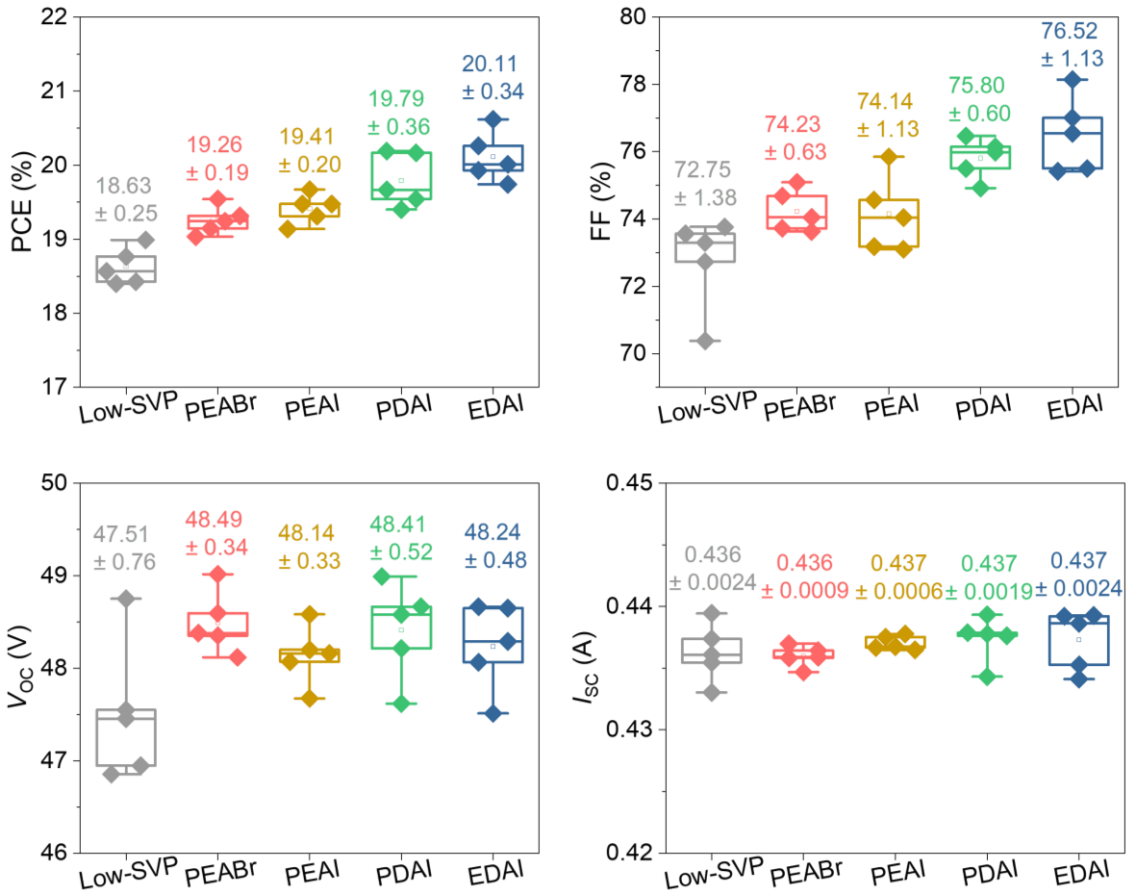

Supplementary Fig. 38 | Statistical photovoltaic parameters of the modules. The PV modules fabricated by low-SVP perovskite films with different ammonium salts surface passivation. Commonly used ammonium salts for low-SVP perovskite films are PEABr, PEAI, $PDAI_2$ and $EDAI_2$. The concentration of passivator is 1.0 mg mL^{-1} and the aperture area of the module is 810 cm^2. Five parallel data sets were taken for each set of conditions. Scatters represent raw data; boxplots show the interquartile range with the median as the center line; whiskers indicate the 5th–95th percentiles. Numerical data are presented as mean ± SD.

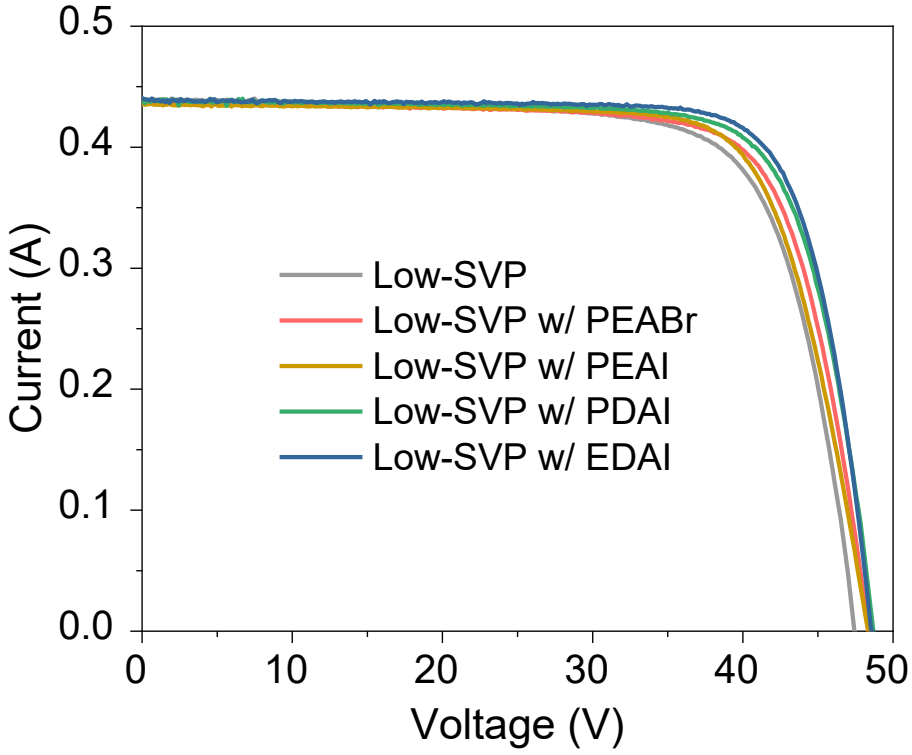

Supplementary Fig. 39 | *I-V* curves of the optimal modules. The modules fabricated by low-SVP perovskite films with surface passivation (the optimal efficiency derived from the statistical data in Supplementary Fig. 38).

Supplementary Note 4:

The coffee-ring effect of AHP in IPA solution.

We attribute the observed coffee-ring effect to a mismatch between solubility and diffusion rate. In IPA, AHP ($EDAI_2$) forms a typical coffee-ring deposit, while LCP ($Pb(OA)_2$) yields a uniform film. The underlying mechanism stems from fundamental differences in solute state, diffusion coefficient (D), and Marangoni flow intensity between the two systems in IPA. The coffee-ring effect arises during droplet drying when the contact line is pinned, preventing overall droplet contraction. To compensate for the rapid evaporation at the edge, a sustained outward capillary flow develops within the droplet. This flow transports solutes toward the periphery. When the rate at which solutes are carried to the edge exceeds their rate of return to the center via Brownian diffusion, solute accumulates at the edge, forming a ring-like deposit.

$Pb(OA)_2$ exists in IPA primarily as colloidal nanoparticles or large molecular clusters, with sizes ranging from several to tens of nanometers. Its large size results in a very low diffusion coefficient (D). Although the initial capillary flow carries particles toward the edge, their extremely low diffusivity causes rapid accumulation and the formation of a solid shell at the periphery, which triggers depinning of the contact line. The subsequent retraction of the contact line (in a "sliding" mode) interrupts the sustained outward capillary flow, a key factor in achieving uniform deposition. Moreover, $Pb(OA)_2$ acts as a surfactant, creating a pronounced concentration gradient at the liquid surface that induces strong Marangoni flow (driven by surface tension gradients). This internal convection effectively mixes the droplet, further suppressing ring-like solute segregation.

In contrast, $EDAI_2$ in IPA is a fully dissolved small-molecule ionic compound ($EDAI^+$ and I^-) with molecular-scale dimensions (<1 nm) and exhibits a very high diffusion coefficient (D) in the low-viscosity solvent. The high interfacial tension between IPA and the perovskite leads to strong pinning of the contact line, hindering its retraction, while continuous evaporation at the edge generates a robust, steady outward capillary flow. Under the rapid-drying conditions of slot-die coating or droplet evaporation (high evaporation flux J), the Péclet number ($Pe = JR/D$, where R is the characteristic length) is much greater than 1, indicating that convective transport far outpaces the return of molecules to the center via diffusion. Additionally, compared to $Pb(OA)_2$, $EDAI_2$ has a negligible effect on the surface tension of IPA, failing to generate a sufficiently strong counteracting Marangoni flow to offset the capillary flow.

In summary, the $Pb(OA)_2$/IPA system suppresses coffee-ring formation through the synergistic action of depinning induced by low diffusivity and strong Marangoni convection. Conversely, the $EDAI_2$/IPA system produces the characteristic coffee-ring deposit due to the combined effects of high diffusivity, strongly pinned contact line, capillary-flow dominance at high Pe, and weak Marangoni

effects. This analysis provides a clear physical picture of how solvent-solute interactions govern the uniformity of printed films.

We performed microscopic SEM characterization of the coffee-ring effect induced by AHPs, as shown in Supplementary Fig. 40. In the PL mapping, regions with lower PL intensity appear darker. The corresponding SEM images reveal that these areas exhibit localized, flake-like aggregates, which obscure the perovskite grain boundaries and crystal facets. Notably, the prevalence of these flake-like aggregates diminishes as the PL brightness increases. Based on the theoretical analysis above, we propose that the coffee-ring effect drives the localized accumulation of AHPs, forming flake-like aggregates. Such high-concentration local stacking is detrimental to the photovoltaic performance of the modules.

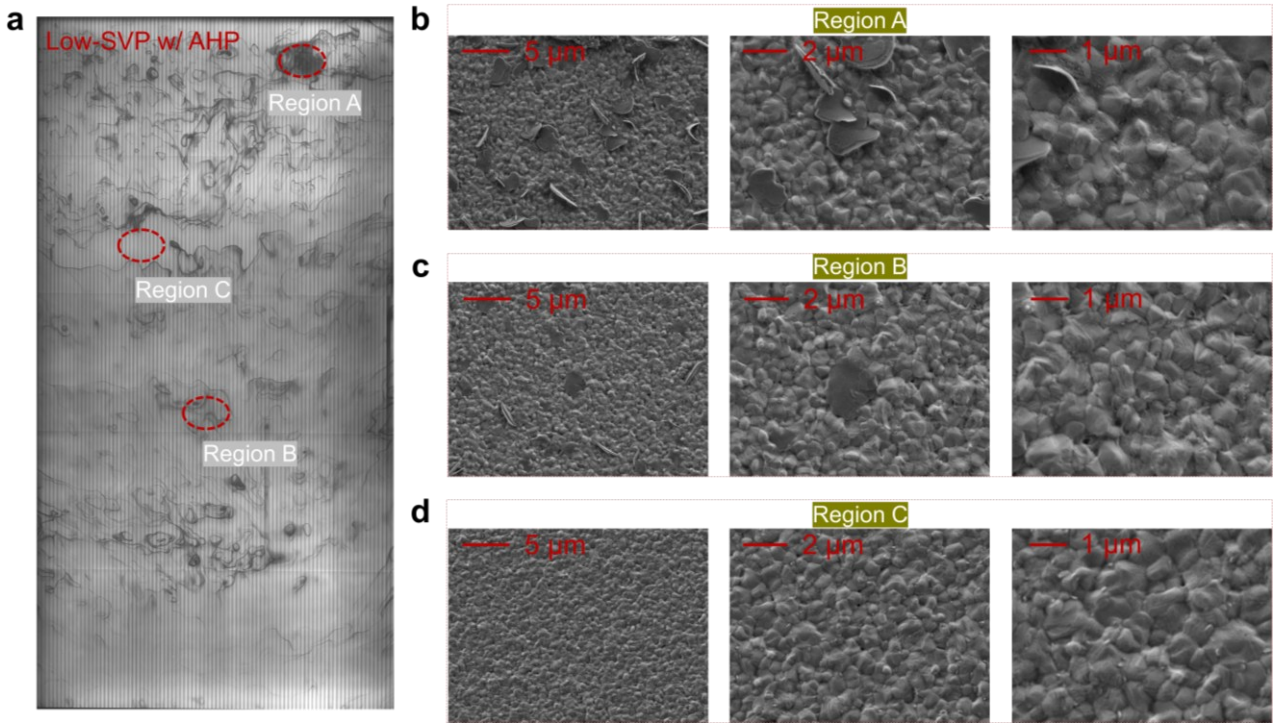

Supplementary Fig. 40 | Microscopic manifestation of the coffee-ring effect. a, PL mapping of AHP commercial-scale PV module. **b-d,** SEM images of the perovskite surface after AHP passivation, showing different regions. Region A, region B, and region C correspond to areas with increasing PL intensity (from dark to bright) in the PL mapping.

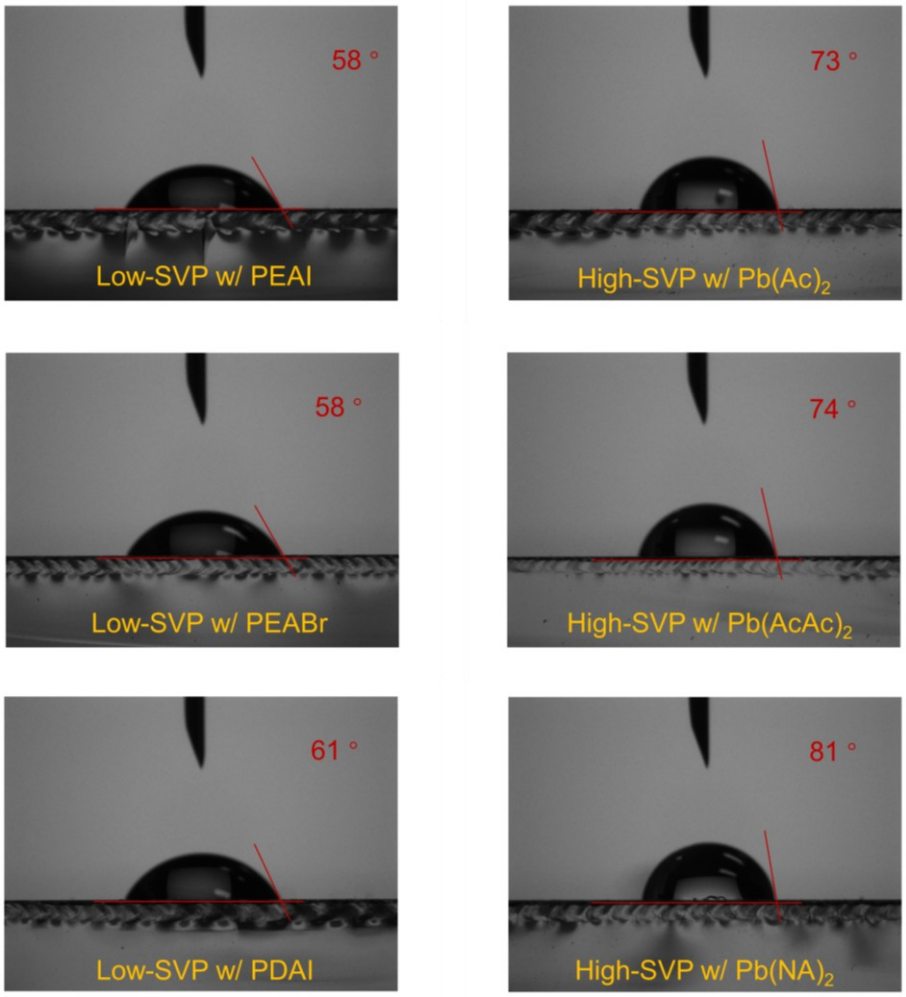

Supplementary Fig. 41 | Water contact angle measurements on different perovskite film surfaces.

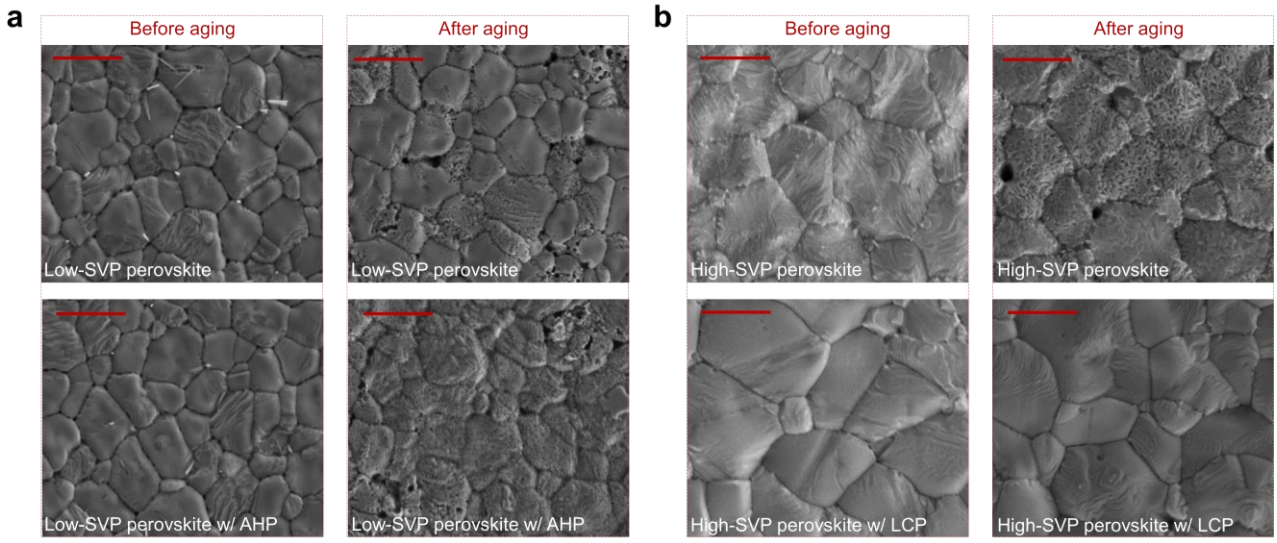

Supplementary Fig. 42 |Top-view SEM images of perovskite films after air aging (30%-50% RH). **a,** Low-SVP perovskite with the corresponding AHP. **b,** High-SVP perovskite with the corresponding LCP. The scale bars correspond to 500 nm in all images.

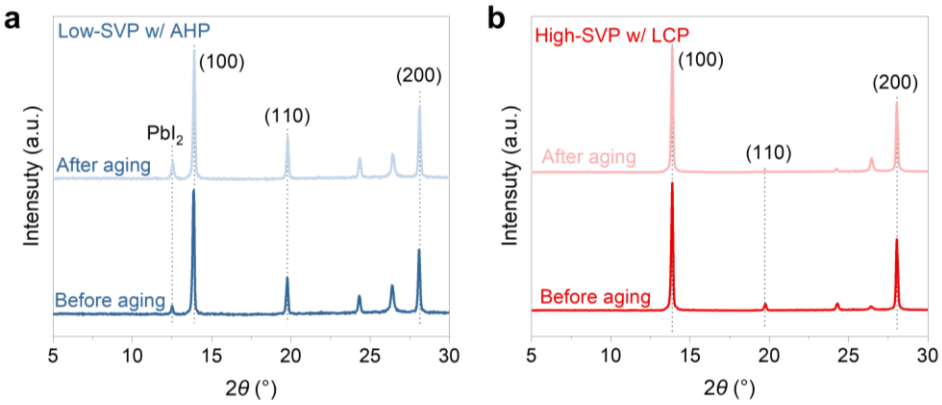

Supplementary Fig. 43 | XRD patterns of perovskite films after air aging (30%-50% RH, 24 h). **a,** Low-SVP perovskite with the corresponding AHP. **b,** High-SVP perovskite with the corresponding LCP.

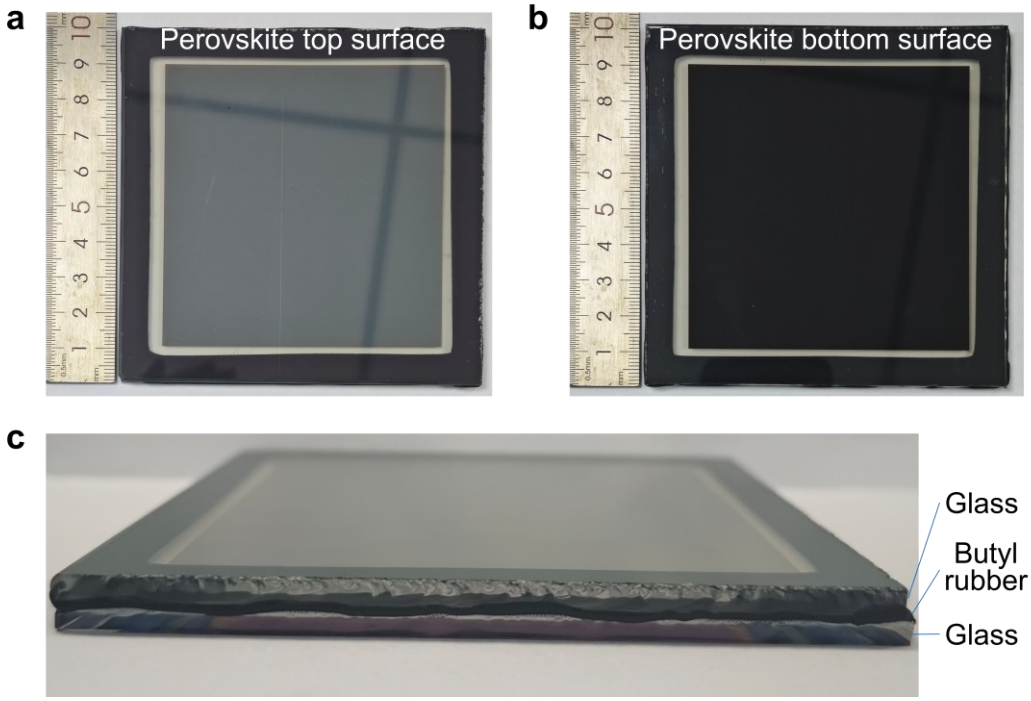

Supplementary Fig. 44 | Photograph of the perovskite film encapsulated in a glass-glass configuration. a, Perovskite film top surface. **b,** Perovskite film bottom surface. **c,** Photograph of the encapsulation cross-section. To exclude the influence of atmospheric conditions during UV aging, the perovskite films were encapsulated prior to aging. The edges were sealed with butyl rubber via hot-pressing, while the active perovskite area was left without a polyolefin elastomer (POE) filler to enable subsequent characterization of the fractured samples.

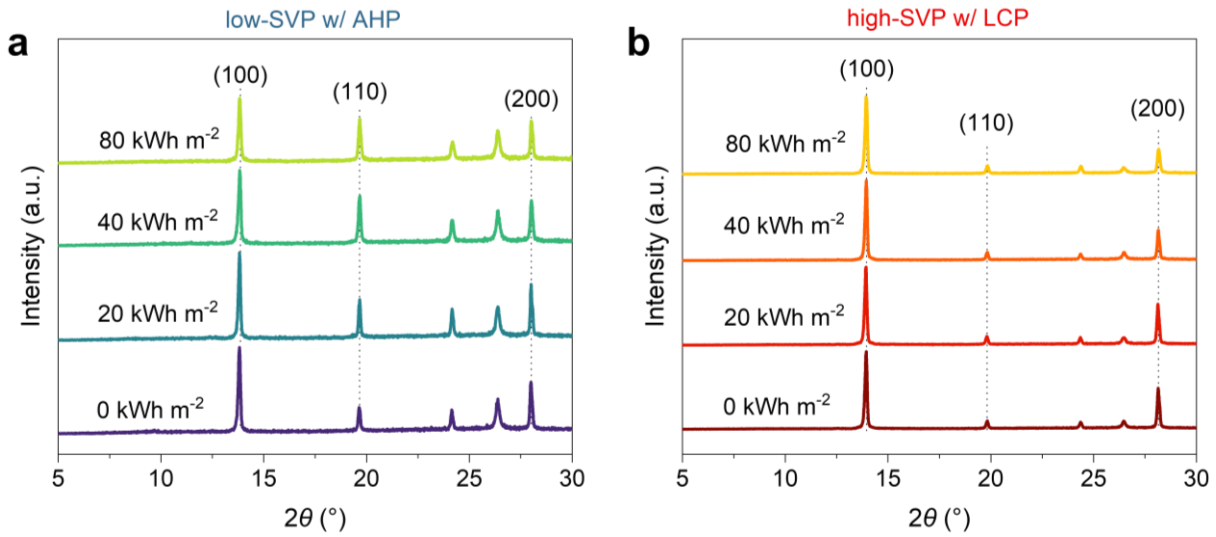

Supplementary Fig. 45 | XRD patterns of perovskite films after UV irradiation. a, The perovskite film prepared low-SVP solvent w/ AHP. **b,** The perovskite film prepared high-SVP solvent w/ LCP. Following AHP ($EDAI_2$) passivation of the low-SVP film, the PbI_2 diffraction peak is attenuated or disappears, yet no low-dimensional perovskite phase is detected in the XRD pattern. In the conventional low-SVP w/ AHP system, the perovskite film undergoes subtle changes in crystallographic orientation upon cumulative UV irradiation doses of 20, 40, and 80 kWh m^{-2}. Specifically, the diffraction intensity of the (100) plane decreases, while that of the (110) plane increases relatively. In contrast, no such shift is observed in the high-SVP system with LCP passivation.

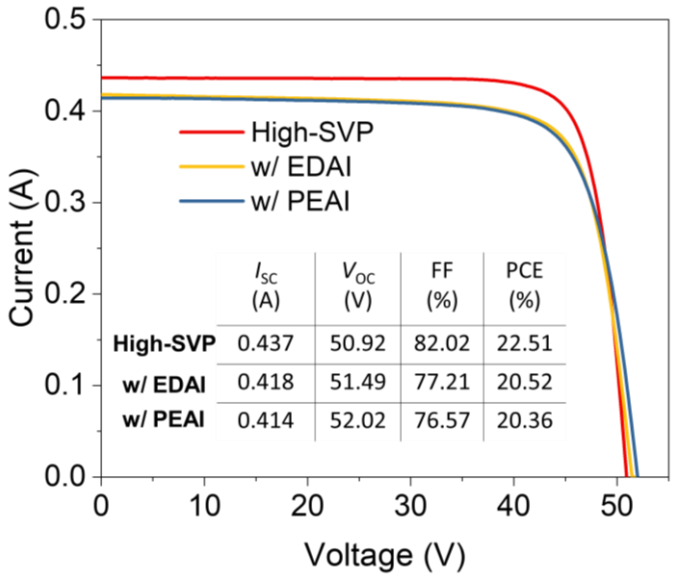

Supplementary Fig. 46 | *I-V* curves of perovskite modules. The modules made from high-SVP system with organic salt surface passivation.

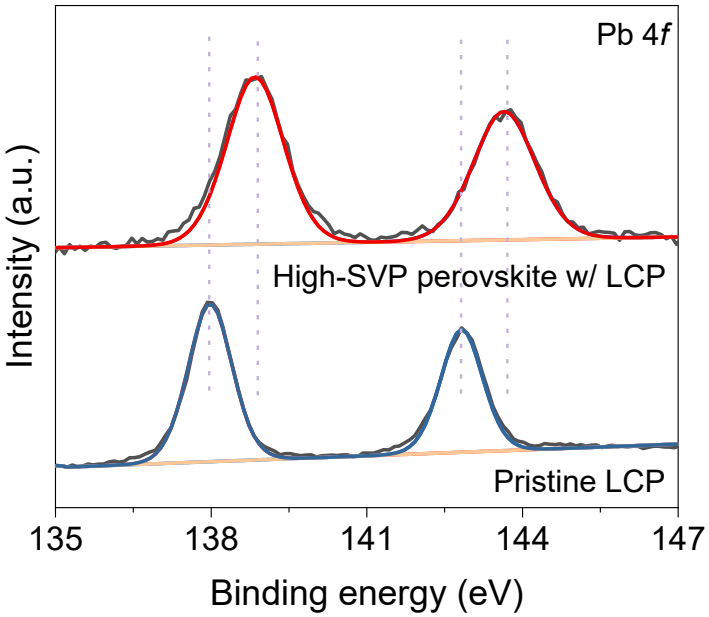

Supplementary Fig. 47 | Pb 4*f* XPS spectra. The XPS spectra of pristine LCP and high-SVP perovskite film with LCP modification.

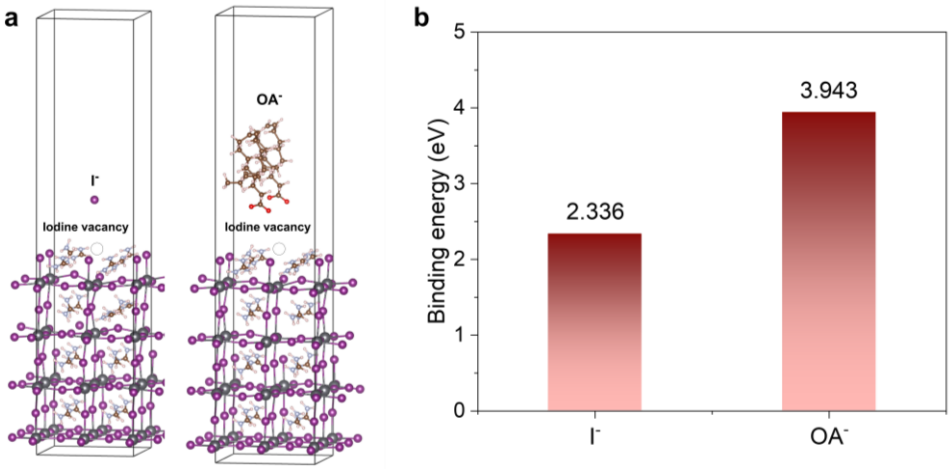

Supplementary Fig. 48 | Calculation of the binding energies of I^- and OA^- at iodine vacancy sites. **a,** Computational models of I^- and OA^- on a defective PbI-terminated surface (I^- vacancy). **b,** Binding energies of I^- and OA^- occupying iodine vacancies.

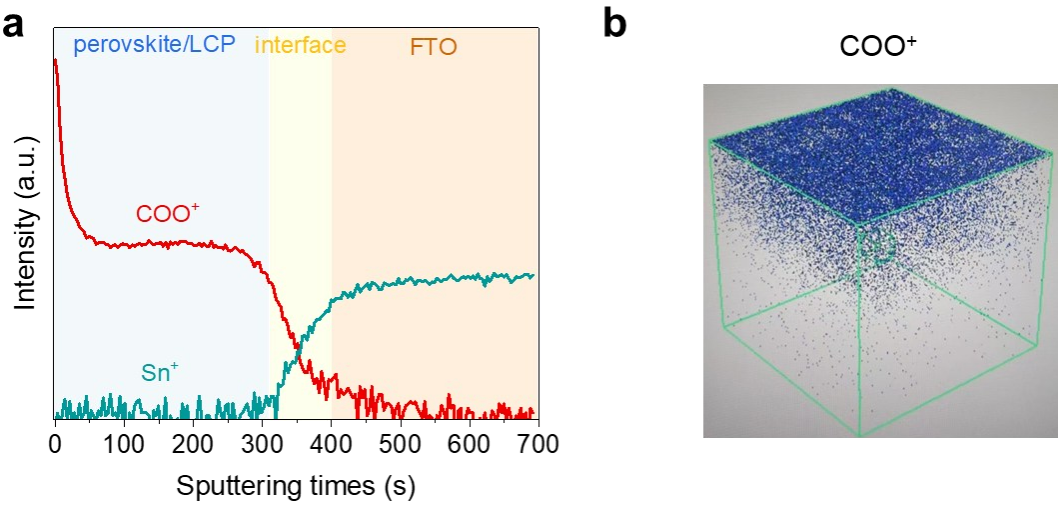

Supplementary Fig. 49 | The TOF-SIMS analysis of high-SVP perovskite film with LCP. a, TOF-SIMS depth profile and **b,** 3D distribution plot of the LCP-passivated perovskite film prepared via the high-SVP method.

Supplementary Note 5:

The ion migration activation energy of perovskite film.

Herein, we investigated the ion migration properties of the perovskite films using temperature-dependent conductivity measurements on Au/perovskite/Au structures to experimentally determine the ion migration activation energy (E_a). The activation energy can be extracted by fitting the raw data to the Nernst–Einstein relation:

$$\sigma(T)=\frac{\sigma 0}{T}\exp(\frac{E_a}{k_B T})$$

where σ(T) is the conductivity as a function of temperature, σ0 is a temperature-independent prefactor, and k_B is the Boltzmann constant.

The fitted Arrhenius plots exhibit two distinct linear regimes. In the low-temperature regime, ion migration is essentially suppressed due to insufficient thermal energy. Above a critical temperature, ion migration becomes thermally activated, leading to an exponential enhancement in conductivity.

From the slopes of the Arrhenius plots, the ion migration activation energy of the high-SVP perovskite film was determined to be 0.531 eV, which increased slightly to 0.554 eV after LCP passivation (Supplementary Fig. 50). This small but clear gain in indicates that the LCP passivation strategy moderately suppresses ion migration, a conclusion that aligns with the theoretical calculations presented in Supplementary Fig. 48.

Furthermore, we employed a quasi-in situ FIB-SEM-AFM technique to analyze the cross-sectional morphology and potential distribution. Supplementary Fig. 51a provides a schematic of the sample preparation, Supplementary Fig. 51b shows a photograph of the FIB etching setup, and Supplementary Fig. 51c presents an SEM image of the intermediate layer exposed after FIB etching on the high-SVP perovskite surface. Theoretically, if OA^- were to infiltrate the perovskite bulk along grain boundaries, a potential difference between the grain boundaries and grain interiors would be expected. However, the actual measurements reveal no significant potential contrast between the grain boundaries and the interiors in the micro-region corresponding to Supplementary Fig. 52. We attribute this to the extremely low concentration of OA^- that permeates into the bulk via grain boundaries, resulting in a negligible change in chemical potential. Additionally, the grain-boundary gaps are highly compact, which may prevent KPFM from accurately resolving the subtle electrical signal variations within such confined areas. Therefore, the trace-level penetration of OA^- does not adversely affect charge transport or the chemical potential landscape within the film.

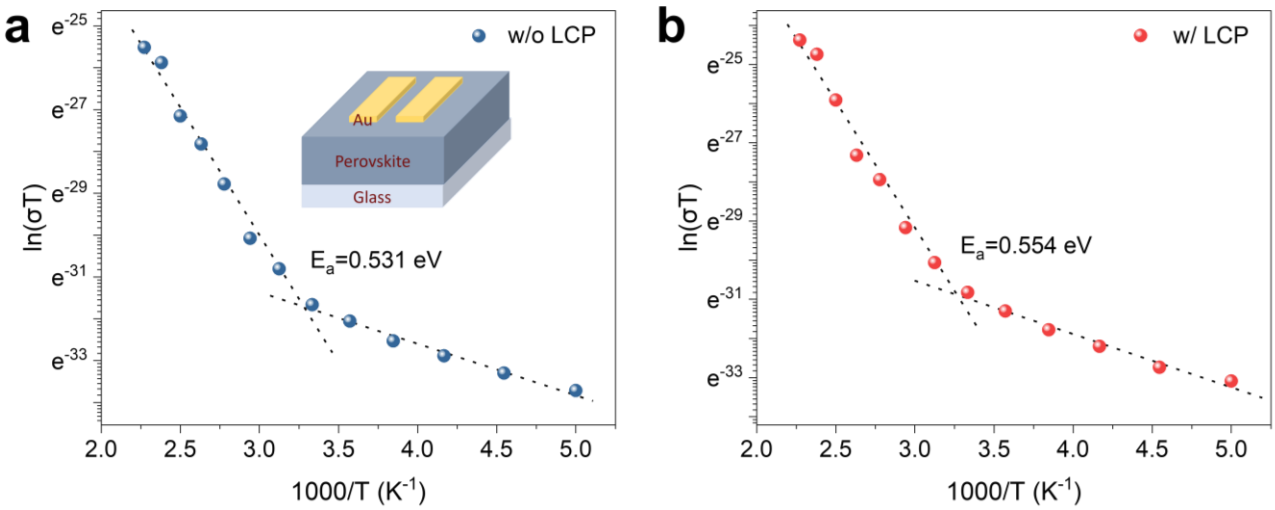

Supplementary Fig. 50 | Temperature-dependent conductivity of perovskite film. a, high-SVP perovskite film and **b,** high-SVP perovskite film w/ LCP.

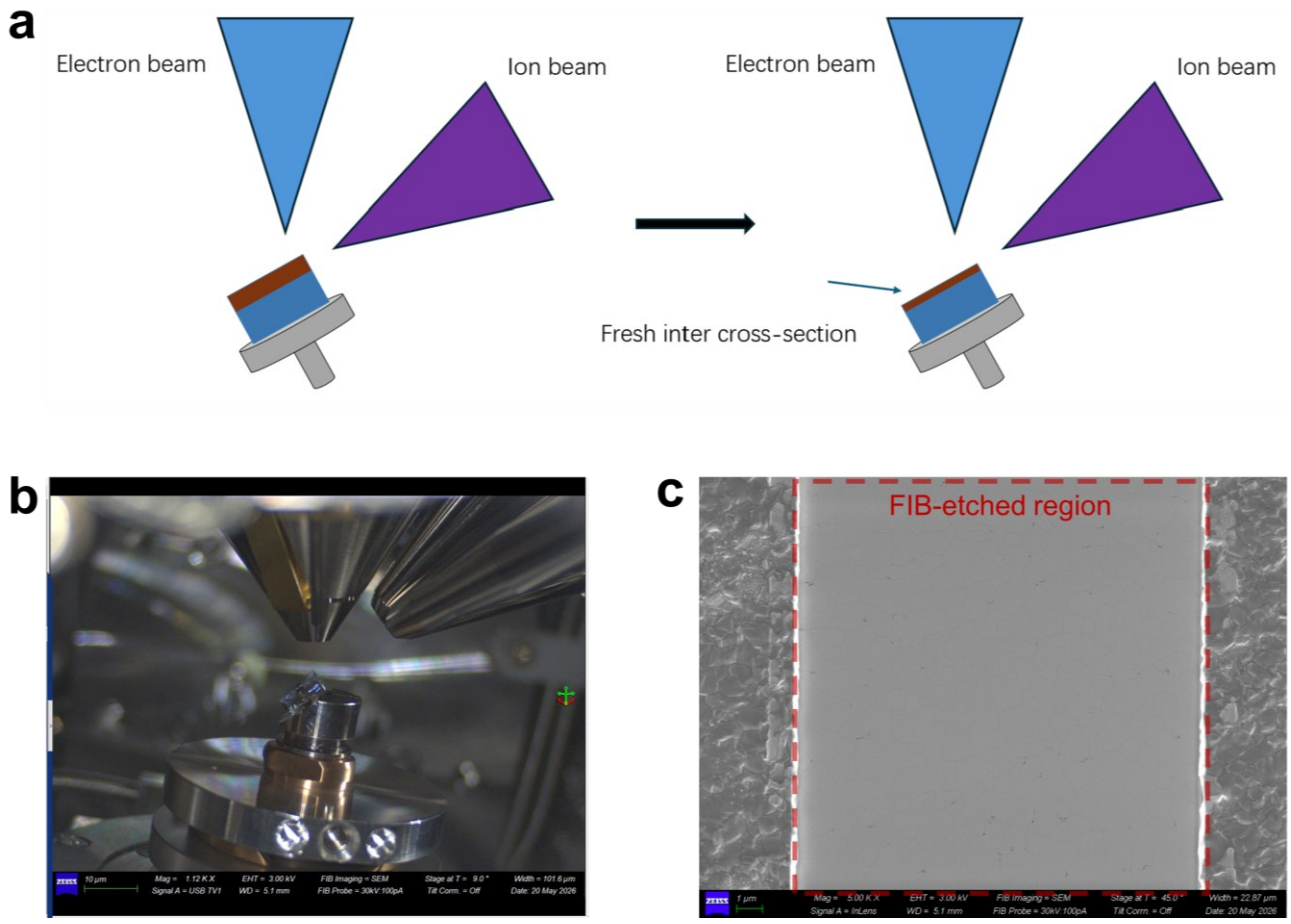

Supplementary Fig. 51 | Surface etching of perovskite film (high-SVP w/ LCP). a, Schematic illustration of focused ion beam (FIB) etching on a perovskite surface. **b,** Photograph of the surface etching setup. **c,** SEM image of the perovskite surface after etching, showing the exposed internal layer where the top surface has been removed in the central region.

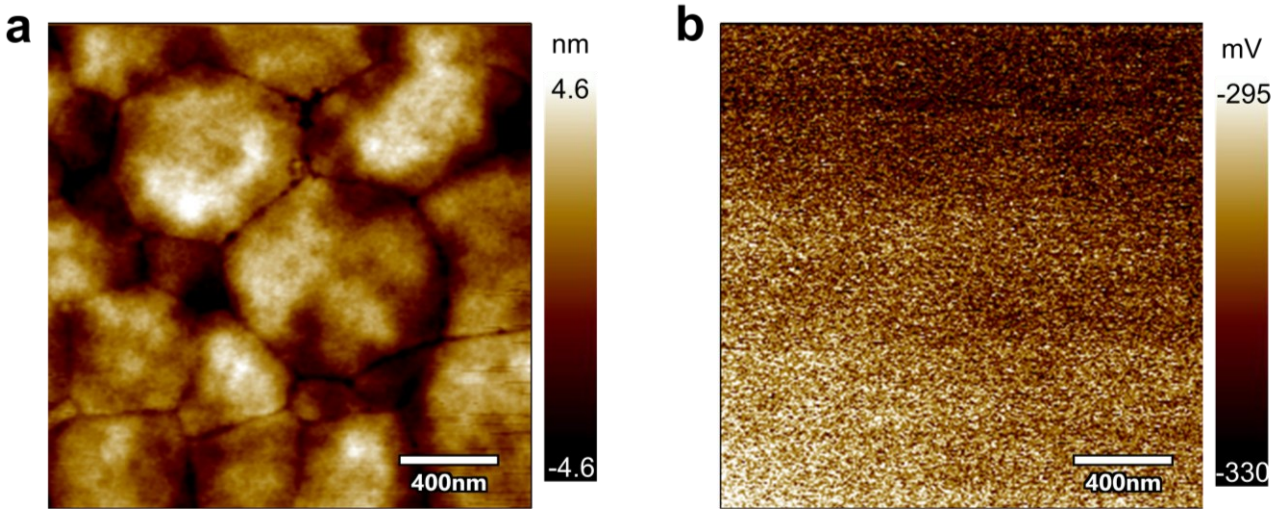

Supplementary Fig. 52 | Potential distribution of perovskite crystals after etching. a, The AFM image and **b,** corresponding KPFM image of high-SVP perovskite film with LCP. The measurement location corresponds to the region subjected to FIB etching in Supplementary Fig. 51c.

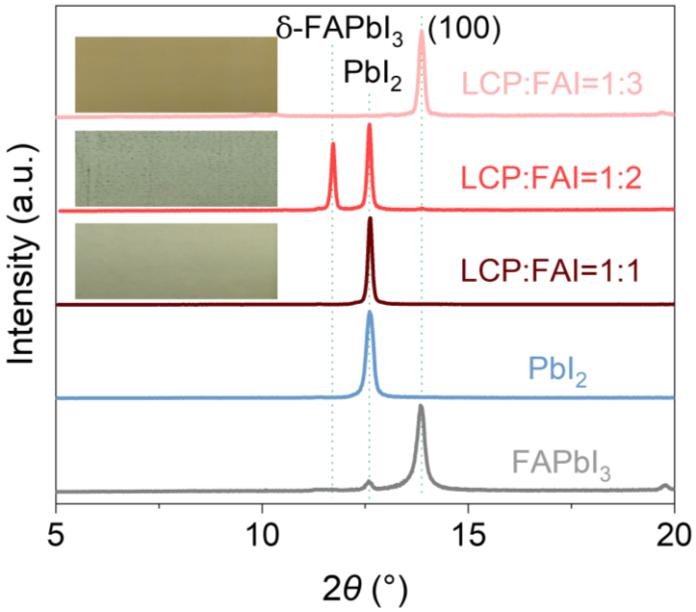

Supplementary Fig. 53 | The XRD patterns of $FAPbI_3$, PbI_2, and mixing LCP ($Pb(OA)_2$) and FAI at different molar ratios. The left inserts are the corresponding photos of the formed films. The LCP:FAI molar ratios of 1:1, 1:2, and 1:3 denote the stoichiometric proportions. The perovskite films were fabricated by dispersing LCP and FAI in a mixed DMF:DMSO solvent (volume ratio 4:1) at a total concentration of 0.5 M. The precursor solution was then subjected to blade coating, followed by vacuum evaporation for 40 s and annealing at 140 °C for 15 min.

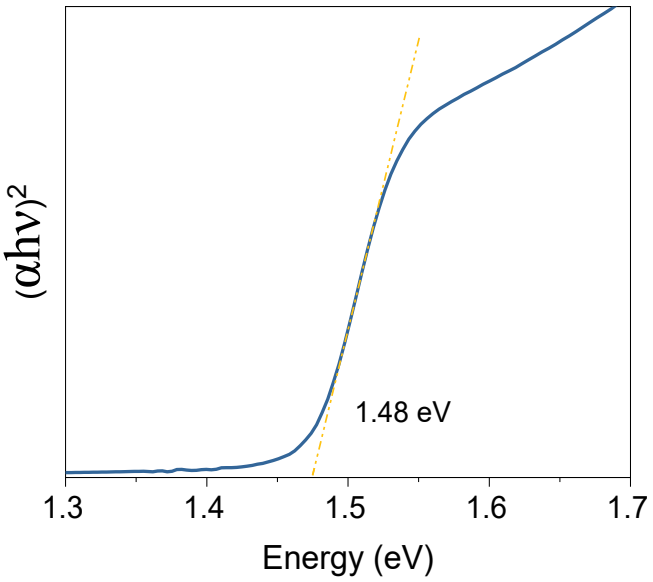

Supplementary Fig. 54 | The bandgap of the film. Derivate bandgap extracted from UV-vis by using the Tauc plots method of the film formed with LCP:FAI mole ratio of 1:3.

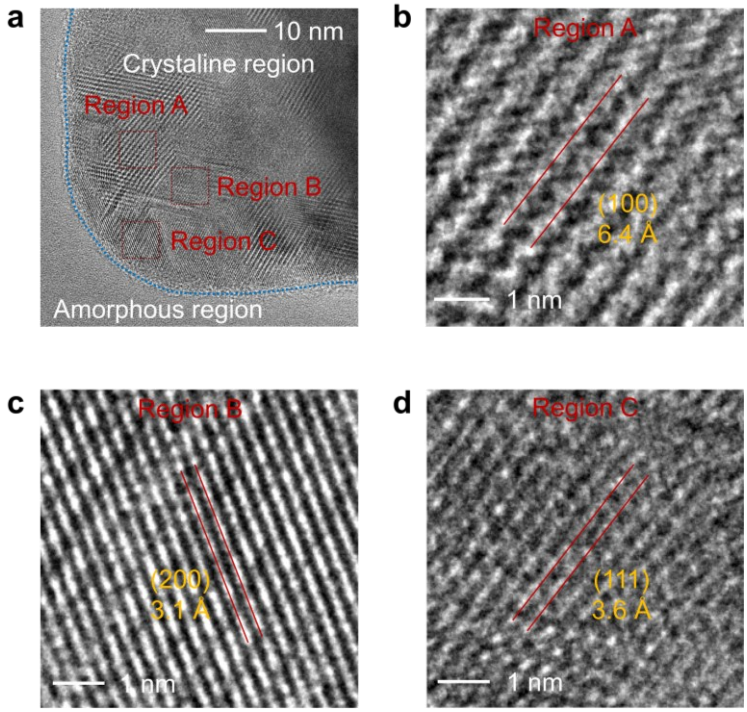

Supplementary Fig. 55 | High-resolution transmission electron microscopy (HR-TEM) images. **a,** Low-magnification HRTEM image. **b–d,** Magnified HR-TEM images of the regions marked in panel a, corresponding to the (100), (200), and (111) lattice planes of α-$FAPbI_3$, respectively. The sample was fabricated using the same protocol as the LCP:FAI = 1:3 condition in Supplementary Fig. 53, confirming the formation of phase-pure α-$FAPbI_3$.

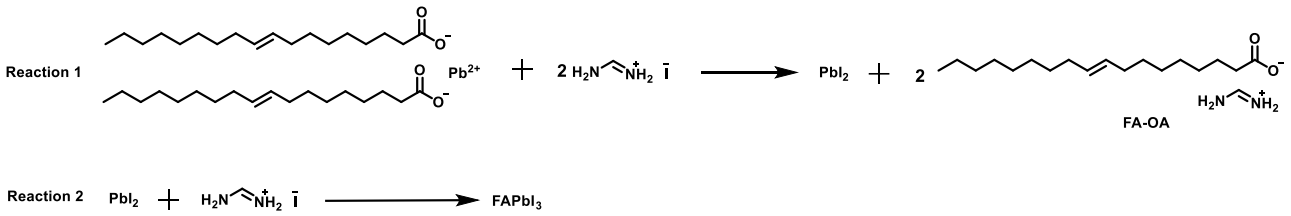

Supplementary Fig. 56 | The in situ reaction process between FAI and LCP via a two-step process. Firstly, PbI_2 and FA-OA is formed via the reaction between FAI and LCP (reaction 1). Subsequently, the as-formed PbI_2 further reacts with FAI to yield $FAPbI_3$ (reaction 2).

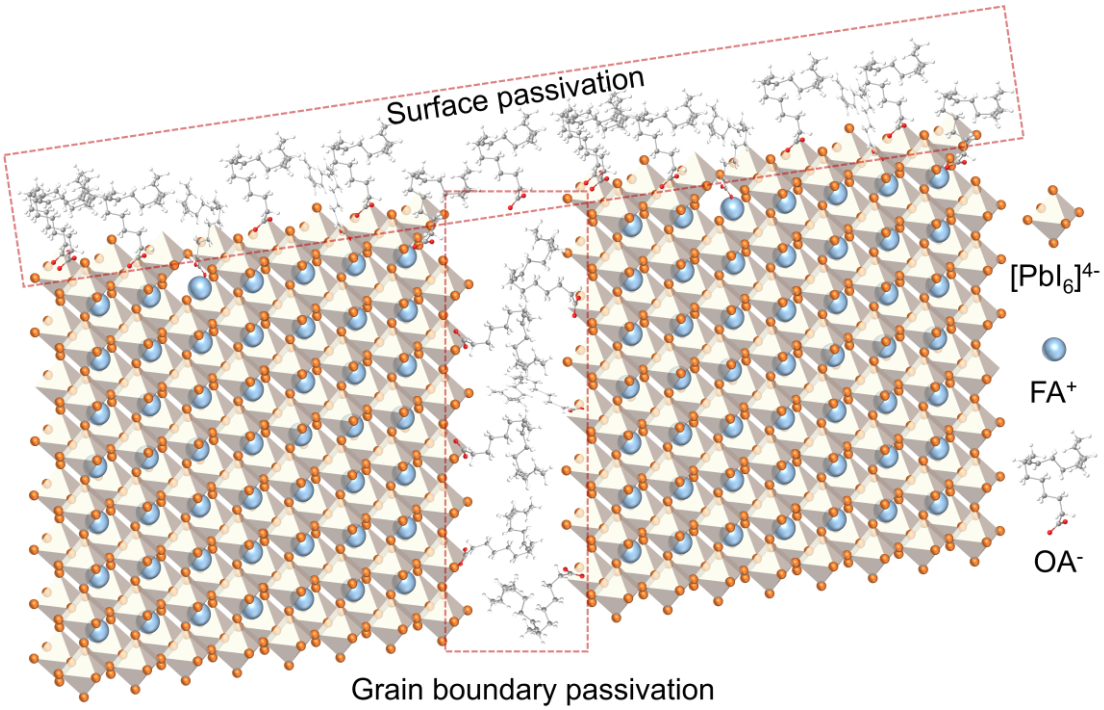

Supplementary Fig. 57 | Schematic illustration of the passivation effect of LCP.

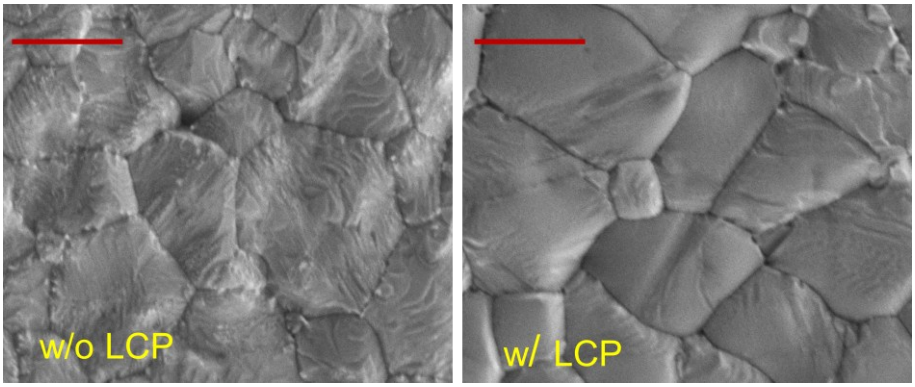

Supplementary Fig. 58 | SEM images of high-SVP perovskite films. The top-view SEM images of high-SVP perovskite films with and without LCP passivation. The scale bars correspond to 500 nm in all images.

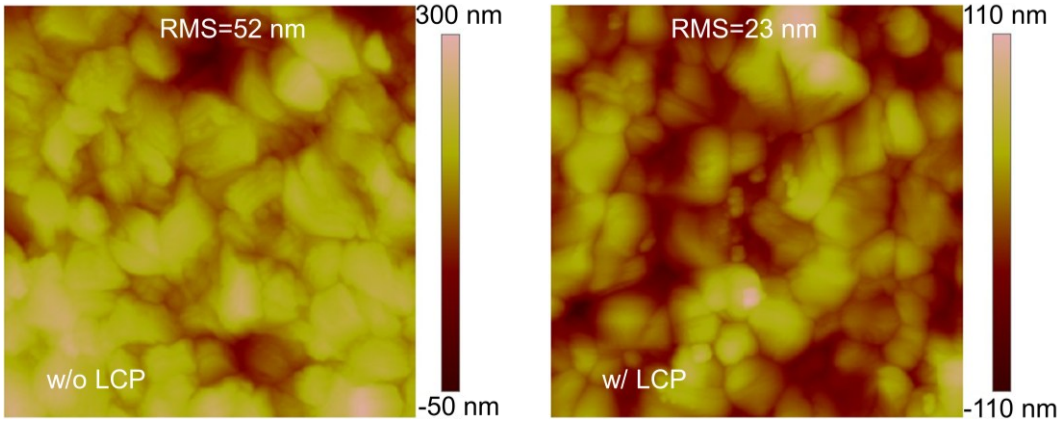

Supplementary Fig. 59 | The AFM images of high-SVP perovskite films with and without LCP passivation. The surface roughness of the perovskite was reduced following LCP modification.

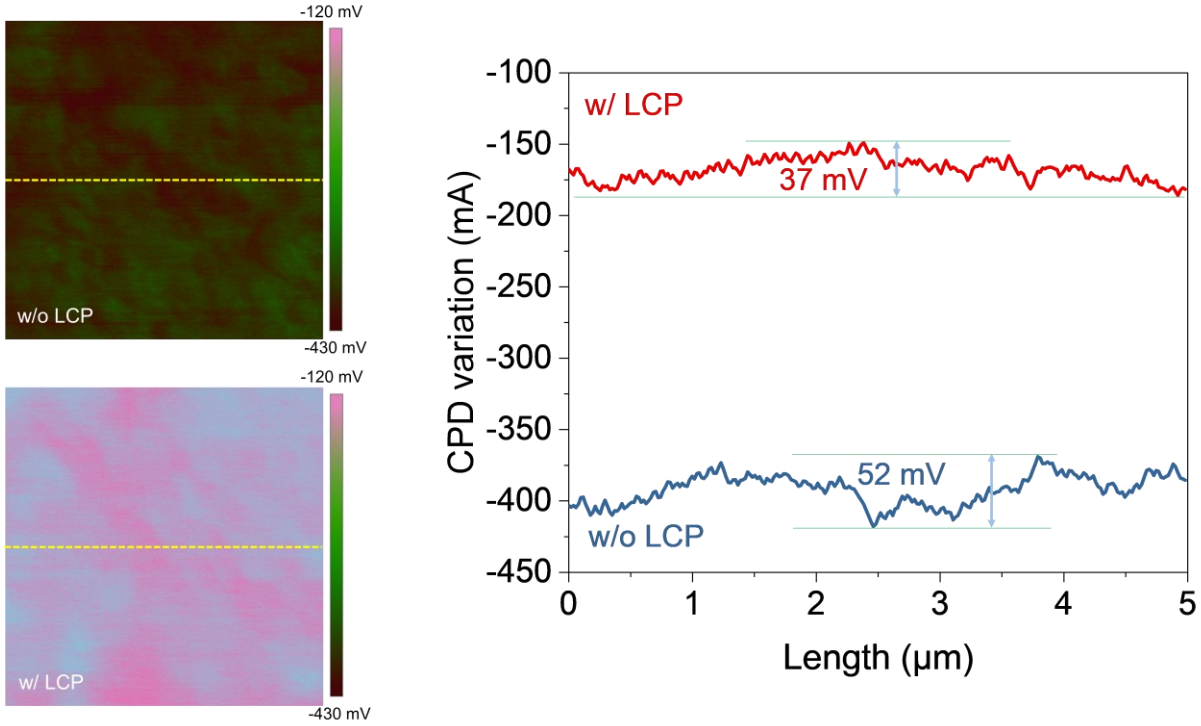

Supplementary Fig. 60 | The KPFM images of high-SVP perovskite films with and without LCP passivation. The line-scan profile in the right panel corresponds to the yellow dashed line indicated in the left panel.

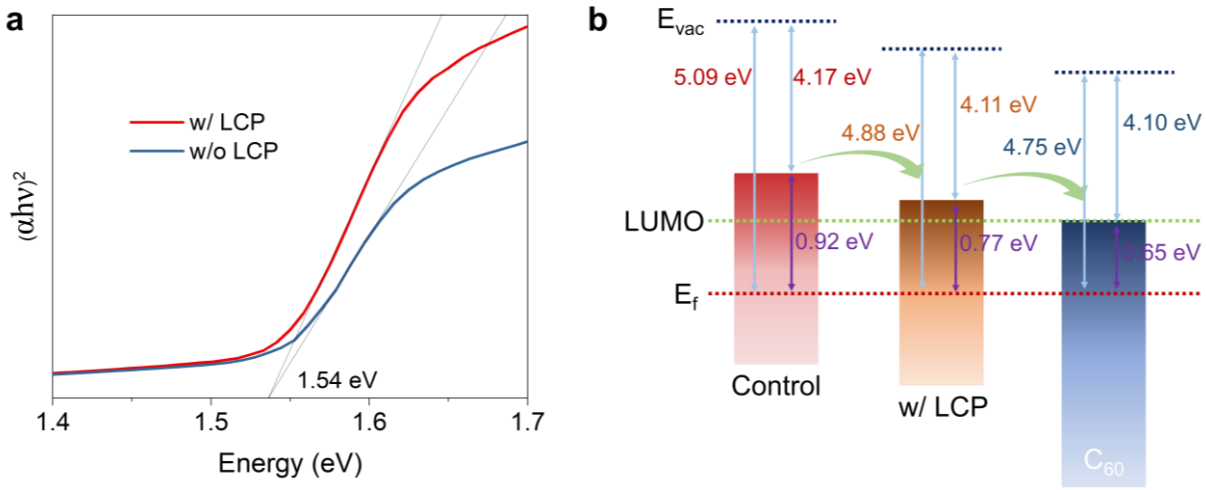

Supplementary Fig. 61 | The energy-level alignment with LCP modification. a, Derivate bandgap extracted from UV-vis by using the Tauc plots. **b,** Band alignment at the interface between perovskite films and electron transport layer C_{60}.

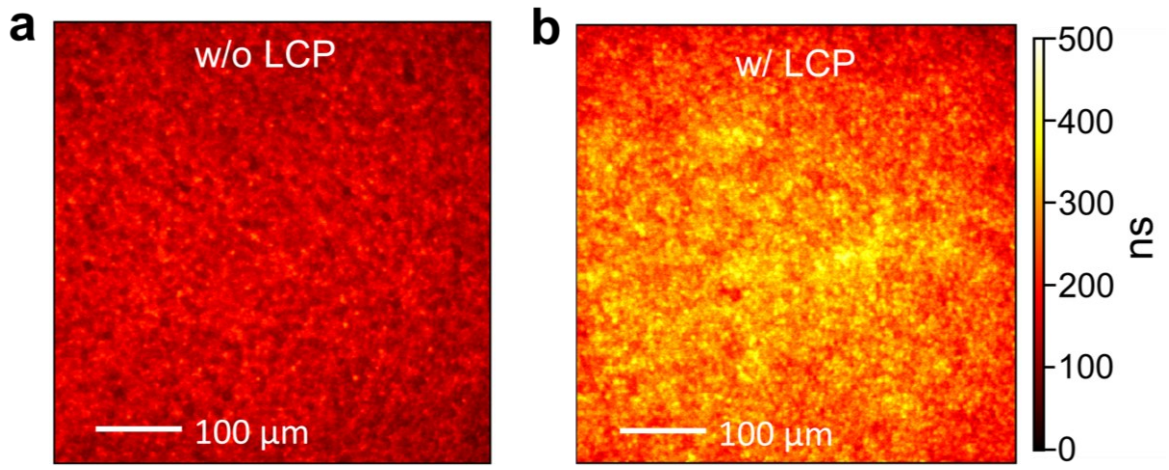

Supplementary Fig. 62 | The carrier lifetime mappings of high-SVP perovskite film with and without LCP passivation. The LCP-modified perovskite exhibits a higher carrier lifetime.

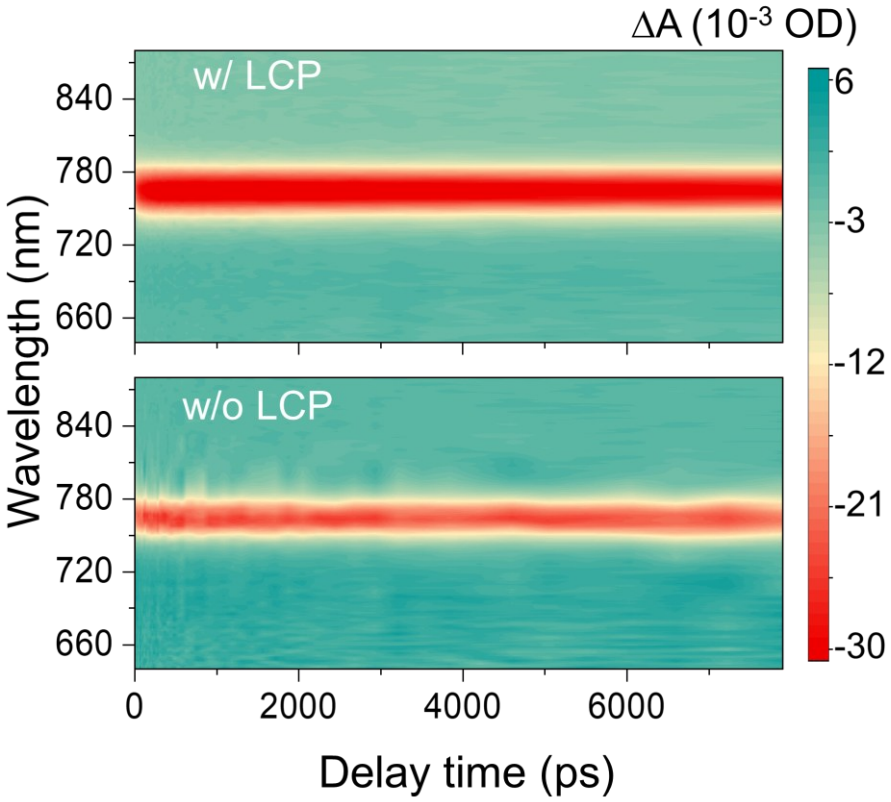

Supplementary Fig. 63 | The ultrafast TA 2D spectra of perovskite films with and without LCP passivation under 380 nm pump excitation.

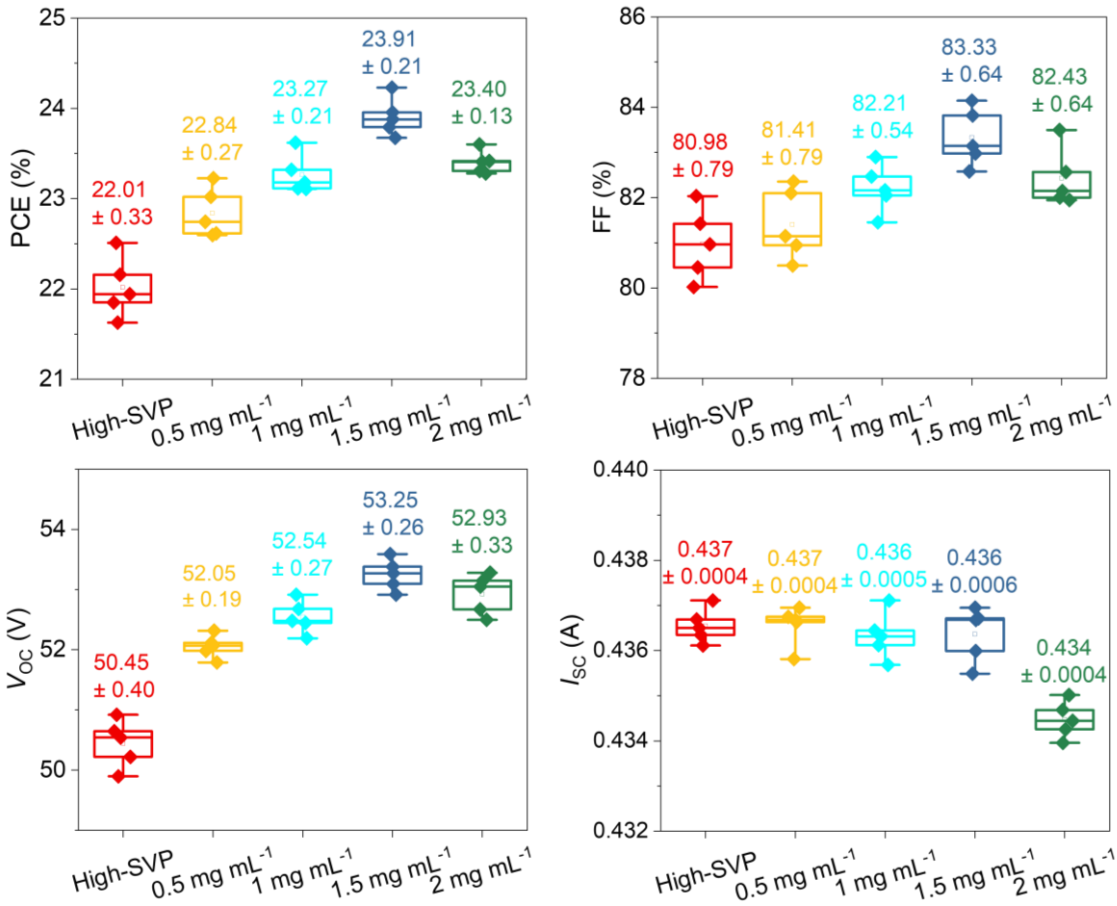

Supplementary Fig. 64 | Statistical photovoltaic parameters of the modules. The PV modules fabricated by high-SVP perovskite films with LCP ($Pb(OA)_2$) at different concentrations. The aperture area of the module is 810 cm^2. Five parallel data sets were taken for each set of conditions. Scatters represent raw data; boxplots show the interquartile range with the median as the center line; whiskers indicate the 5th–95th percentiles. Numerical data are presented as mean ± SD.

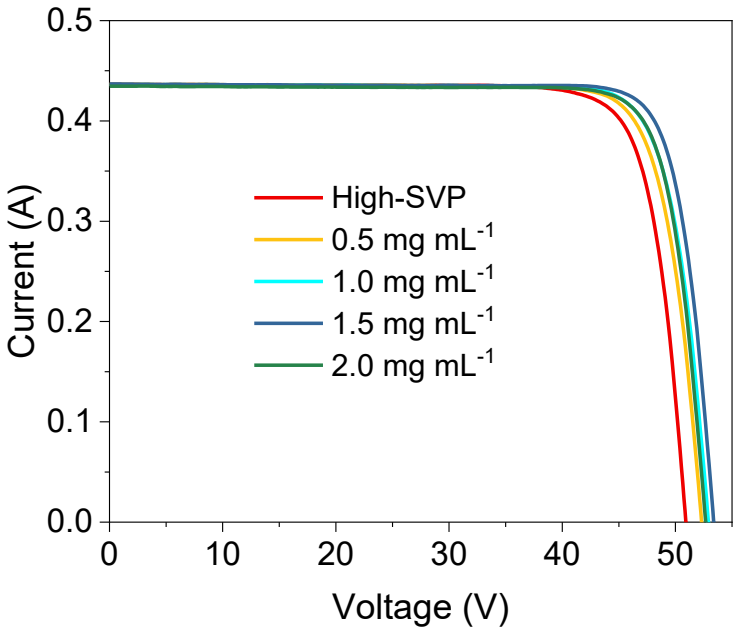

Supplementary Fig. 65 | *I-V* curves of the optimal modules. The modules fabricated by high-SVP perovskite films with LCP ($Pb(OA)_2$) at different concentrations.

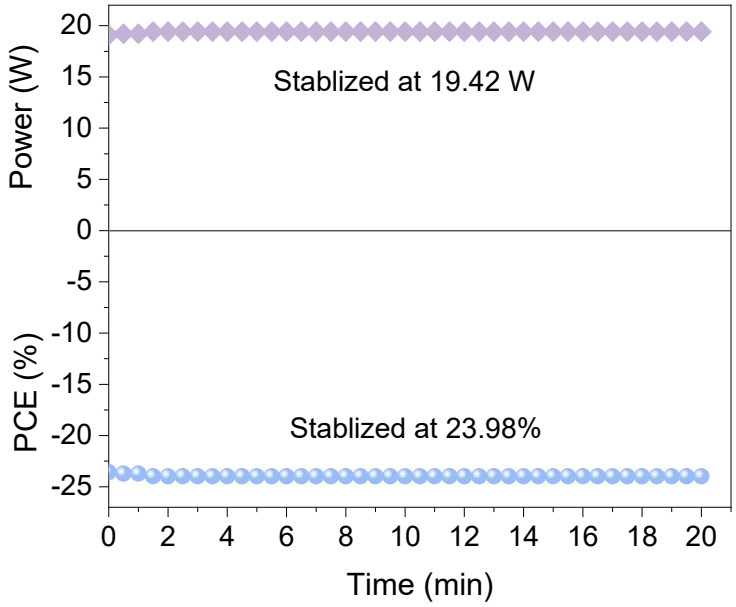

Supplementary Fig. 66 | Stabilized P_{max} plots for the best-performing module for 20 min.

2.3 Date(s) of Testing 2025-10-28

2.4 Location(s) of Testing Zhejiang HJE Co., LTD
3-4/F., Building 1, No. 3556, Linggongtang Road, Nanhu District, Jiaxing, Zhejiang, China

2.5 Points of Non-Compliance or Exceptions of the Test Procedure

- N/A

3. Test Results

- "Decision rule according to IEC Guide 115:2023, clause 4.3.3 was applied."
- "Decision rule (based on ILAC-G8) for an upper specification limit (A lower limit or specification with an up-per and a lower limit is treated similarly.):
  - Inconclusive result: If a measurement result plus/minus the expanded uncertainty with a 95 % coverage probability overlaps the limit it will be stated that it is not possible to state compliance or non-compliance."
- There are no statements to conformity in this report, no decision rule has been applied.

3.1 Positive Test Results

3.1.1	TABLE: I-V characteristic							—
Test Date [MM/DD/YYYY].....				10/28/2025				—
Radiant Source.....				☒ Solar simulator ☐ Natural sunlight				—
Module temperature [°C].....			:	26.20 for reverse scan 26.66 for forward scan				—
Irradiance [W/m²].....			:	1000				—
Sample No.	Isc [A]	Voc [V]	Imp [A]	Vmp [V]	Pmp [W]	FF[%]	η[%]	Remark
RS-A-1#	0.436	53.461	0.419	46.381	19.436	83.40	24.00	Reverse scan (Voc→Isc)

	0.437	53.348	0.410	46.036	18.874	80.88	23.30	Forward scan (Isc→Voc)

Supplementary information: The aperture area of the mask: 809.69cm² (provided by customer).
Reverse scan:

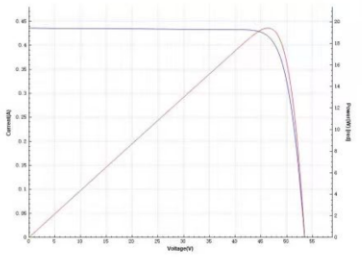

Forward scan:

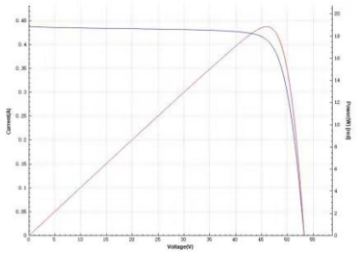

Report No.: 704062596802
Rev.: 00A1
Date: 2025-11-07
www.tuvsud.com

Supplementary Fig. 67 | TÜV SÜD-certified champion module with the efficiencies of 24.0% (reverse) and 23.30% (forward) PCE at 810 cm² aperture area.

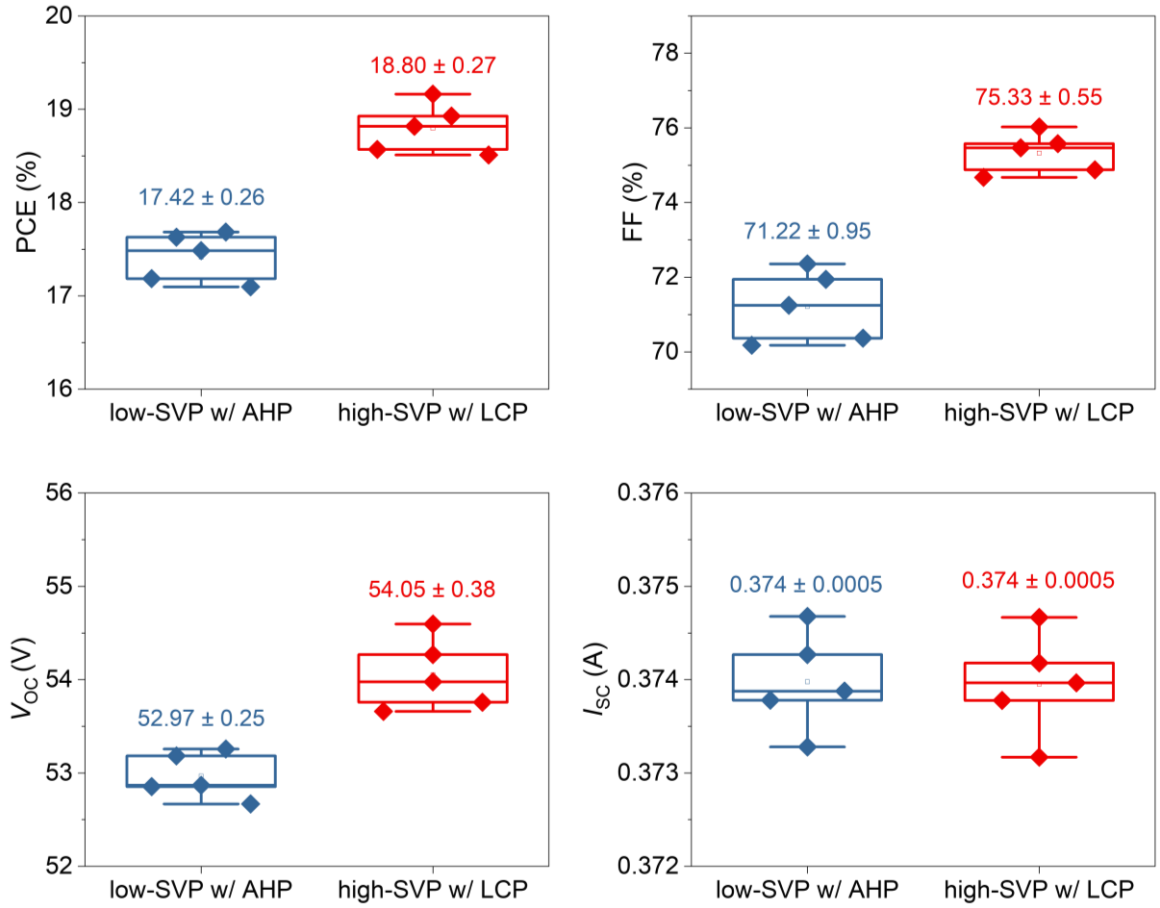

Supplementary Fig. 68 | Statistical photovoltaic parameters of the perovskite modules (the perovskite film bandgap is 1.68 eV). The PV modules fabricated by low-SVP perovskite with AHP and high-SVP perovskite with LCP. The aperture area of the module is 810 cm^2. Five parallel data sets were taken for each set of conditions. Scatters represent raw data; boxplots show the interquartile range with the median as the center line; whiskers indicate the 5th–95th percentiles. Numerical data are presented as mean ± SD.

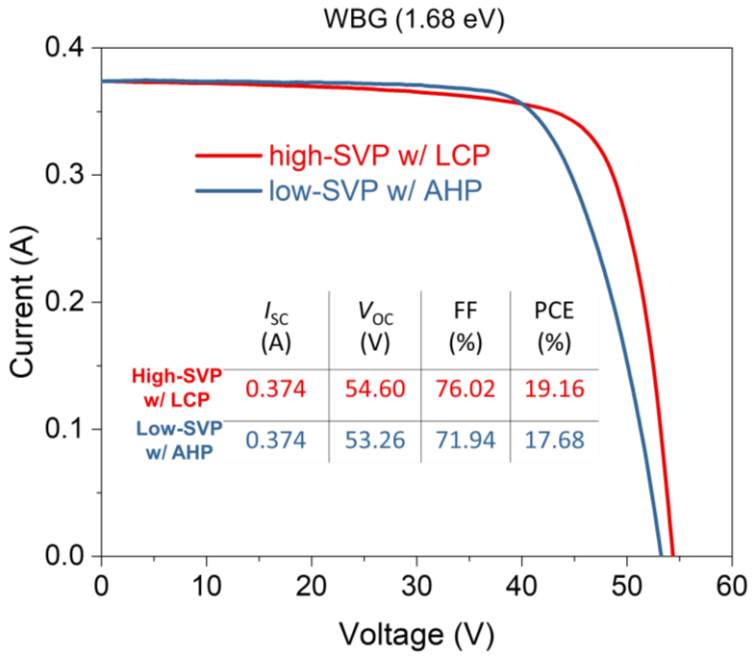

Supplementary Fig. 69 | *I-V* curves of the optimal modules (bandgap=1.68 eV). The modules, fabricated from low-SVP perovskite with AHP and high-SVP perovskite with LCP, correspond to Supplementary Fig. 68.

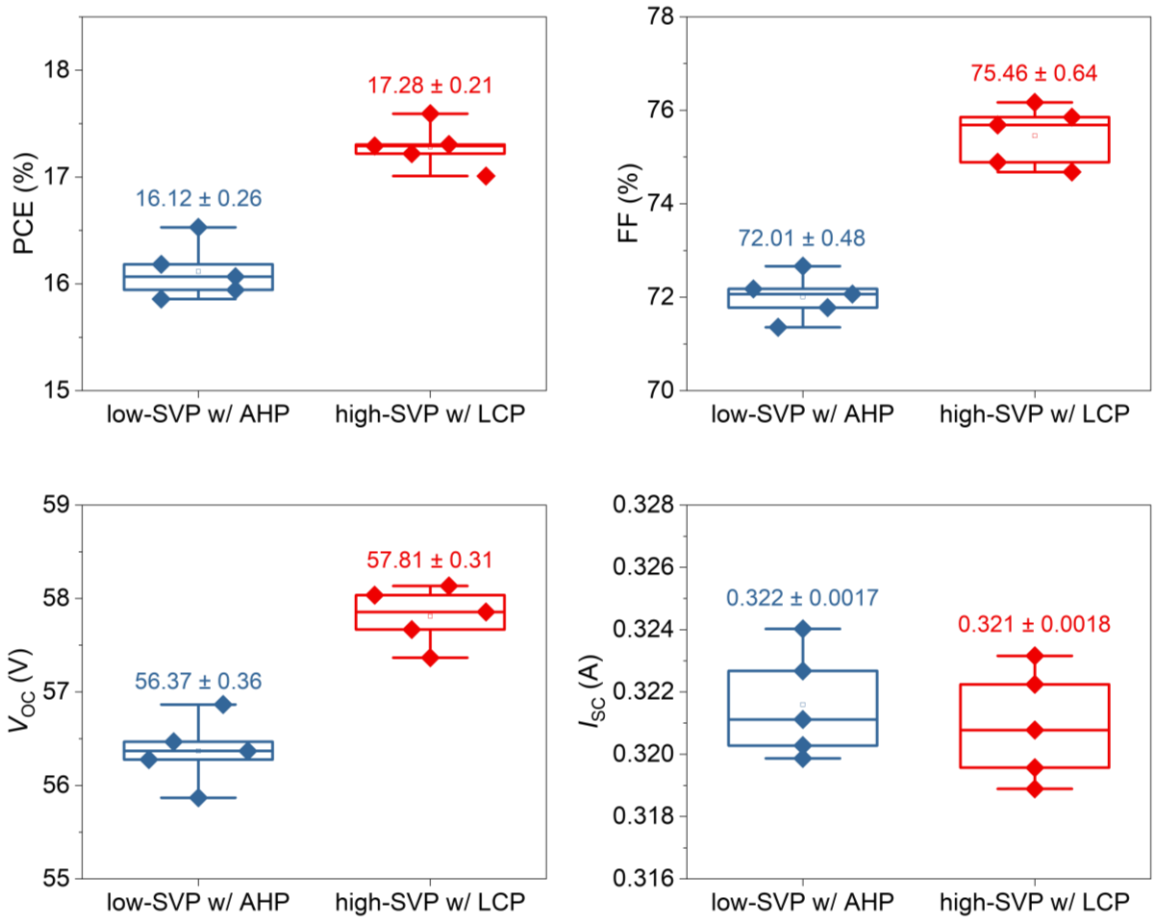

Supplementary Fig. 70 | Statistical photovoltaic parameters of the perovskite modules (the perovskite film bandgap is 1.80 eV). The PV modules fabricated by low-SVP perovskite with AHP and high-SVP perovskite with LCP. The aperture area of the module is 810 cm^2. Five parallel data sets were taken for each set of conditions. Scatters represent raw data; boxplots show the interquartile range with the median as the center line; whiskers indicate the 5th–95th percentiles. Numerical data are presented as mean ± SD.

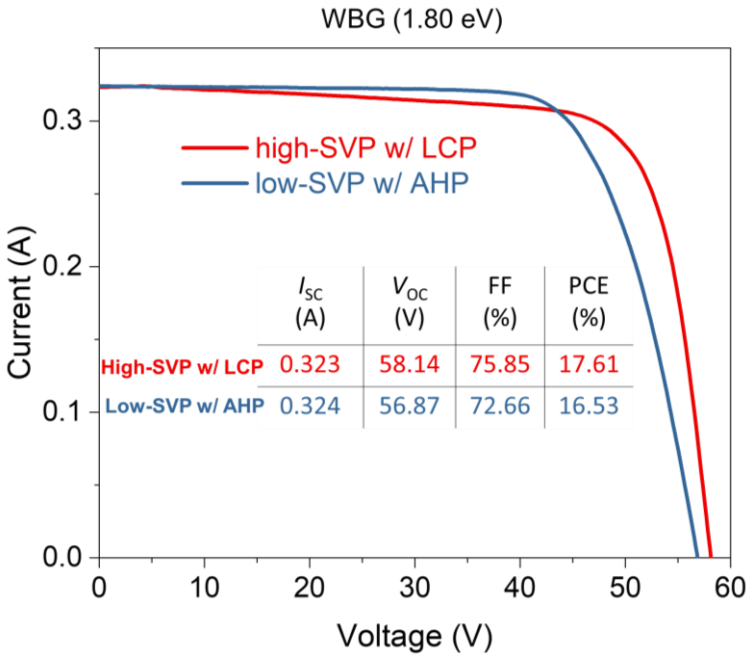

Supplementary Fig. 71 | *I-V* curves of the optimal modules (bandgap=1.80 eV). The modules, fabricated from low-SVP perovskite with AHP and high-SVP perovskite with LCP, correspond to Supplementary Fig. 70.

2.3 Date(s) of Testing 2025-11-13

2.4 Location(s) of Testing China Telecommunication Technology Labs. CuiHu Cloud Center, No.1 Gaolizhang Road, Wenquan Town, Haidian District, Beijing, China

2.5 Points of Non-Compliance or Exceptions of the Test Procedure

- N/A

3. Test Results

- "Decision rule according to IEC Guide 115:2023, clause 4.3.3 was applied."
- "Decision rule (based on ILAC-G8) for an upper specification limit (A lower limit or specification with an up-per and a lower limit is treated similarly.):
  - Inconclusive result: If a measurement result plus/minus the expanded uncertainty with a 95 % coverage probability overlaps the limit it will be stated that it is not possible to state compliance or non-compliance."
- There are no statements to conformity in this report, no decision rule has been applied.

3.1 Positive Test Results

3.1.1	TABLE: I-V characteristic							—
Test Date [MM/DD/YYYY].....				11/13/2025				—
Radiant Source.....				☒ Solar simulator ☐ Natural sunlight				—
Module temperature [°C].....			:	25±2				—
Irradiance [W/m²].....			:	1000				—
Sample No.	Isc [A]	Voc [V]	Imp [A]	Vmp [V]	Pmp [W]	FF[%]	η[%]	Remark
21#	1.766	110.75	1.662	95.30	158.38	80.98	22.00	Reverse scan (Voc→Isc)
21#	1.776	109.83	1.629	93.38	152.16	78.01	21.13	Forword scan (Isc →Voc)

Supplementary information: Module area: 7200cm²

Reverse scan

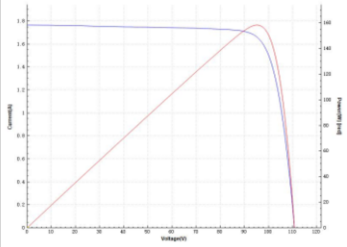

Forword scan

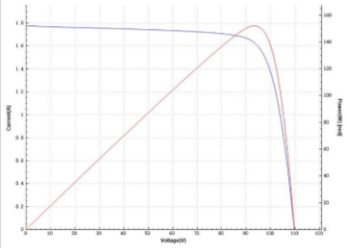

The decimal places of electrical parameters are retained according to customer requirements.

3.2 Points of Non-Compliance according to the test specification

- None

Supplementary Fig. 72 | TÜV SÜD-certified champion commercial-scale PV module with the efficiencies of 22.0% (reverse) and 21.13% (forward) PCE at 0.72 m^2 total area.

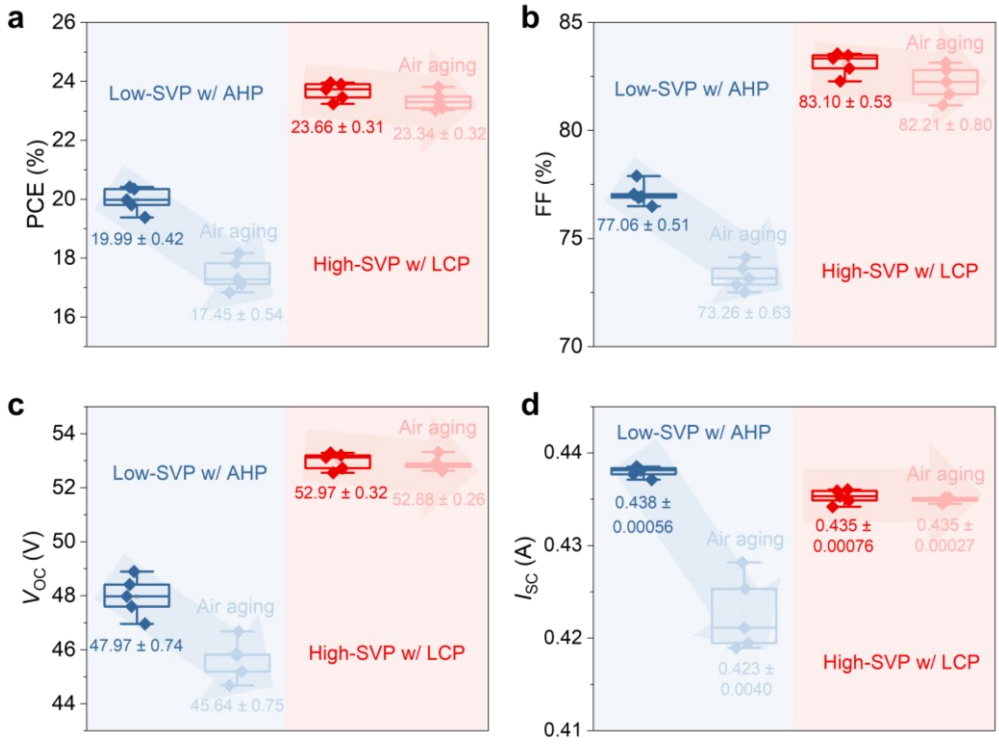

Supplementary Fig. 73 | Statistical photovoltaic parameters of the modules (Aperture area = 810 cm², 5 modules for each type). a, PCE, **b,** FF, **c,** V_{OC}, and **d,** I_{SC}. The aging conditions were identical to those described in Supplementary Fig. 41. Subsequently, the remaining functional layers were deposited sequentially, such as thermally evaporated C_{60} and ALD SnO_2, to complete the module fabrication. Scatters represent raw data; boxplots show the interquartile range with the median as the center line; whiskers indicate the 5th–95th percentiles. Numerical data are presented as mean ± SD.

Supplementary Note 6:

The stability test in internal laboratory.

(i) UV Test (Ultraviolet Aging Test)

Purpose: Pre-treatment of components with UV radiation before thermal cycling/wet-freeze tests to evaluate materials and adhesives susceptible to UV aging.

Apparatus: a) Test chamber capable of maintaining component temperature at (60 ± 5) °C. b) Temperature sensor attached near the center of the component (front or back) without blocking light exposure. c) UV radiometer. d) UV light source with ±15% irradiance uniformity and capable of providing necessary total irradiance across different spectral ranges. e) Components can be short-circuited or open-circuited as per choice.

Procedure: a) Ensure wavelength range is 280 nm to 400 nm, with irradiance not exceeding 250 W/m^2 (5 times natural sunlight) and uniformity within ±15%. b) Install components (short circuited or open-circuited) on the test plane, maintaining temperature at (60 ± 5) °C. c) Total irradiance must be at least 15 kWh/m^2, with component temperature maintained within the specified range.

Criteria: a) After 15 kWh of UV pre-treatment, power degradation should be ≤5%. Further testing may extend to 30–60 kWh, with power degradation ≤5%. The longer the duration, the better.

(ii) Damp Heat Test (1300 Hours)

Purpose: To evaluate the component's resistance to long-term humidity penetration.

Procedure: Conduct the test according to IEC 60068-2-78 and the following conditions: Temperature: (85 ± 2) °C; Relative Humidity: (85 ± 5)%; Duration: (1300 ±48) hours.

Final Testing: After recovery for 2-4 hours under open-circuit conditions at (23±5) °C and ≤75% relative humidity, repeat visual and wet leakage current tests. Power degradation after 1000 hours of aging should be <5%.

(iii) Thermal Cycling Test (300 Cycles)

Purpose: To measure the component's resistance to thermal mismatch, fatigue, and other stresses caused by temperature variations.

Apparatus: a) Fixtures to secure components in the environmental chamber, allowing free airflow. b) Temperature measurement tools with ± 2.0 °C accuracy and ± 0.5 °C repeatability. c) Continuous current supply device. d) Monitoring equipment for current flow during the test. e) Apply a 5 N weight to the junction box during testing.

Procedure: Heating/cooling rate: ≤1.7 °C/min. Cycle between -40 °C and +85 °C for 300 cycles. Hold at peak temperatures for at least 10 minutes. Apply Imp current during heating from -40 °C to +80 °C; otherwise, apply <1% Imp current.

Monitoring: Ensure junction box adhesion to the back sheet is maintained during testing. Apply a 5 N weight to the junction box during the test.

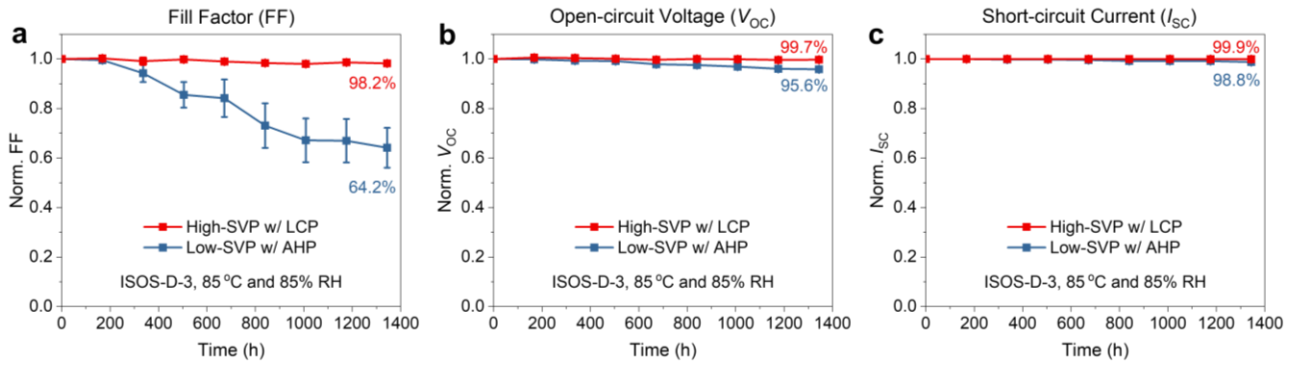

Supplementary Fig. 74 | Encapsulated PV modules aged under ISOS-D-3 testing protocol (5 modules for each type). Corresponding changes in the parameters **a,** FF, **b,** V_{OC}, and **c,** I_{SC}.

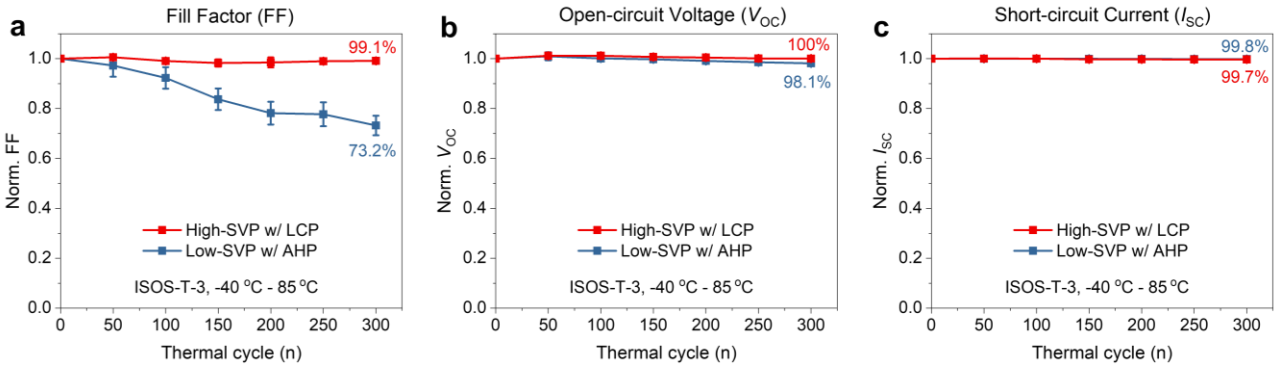

Supplementary Fig. 75 | Encapsulated PV modules aged under ISOS-T-3 testing protocol (5 modules for each type). Corresponding changes in the parameters **a,** FF, **b,** V_{OC}, and **c,** I_{SC}.

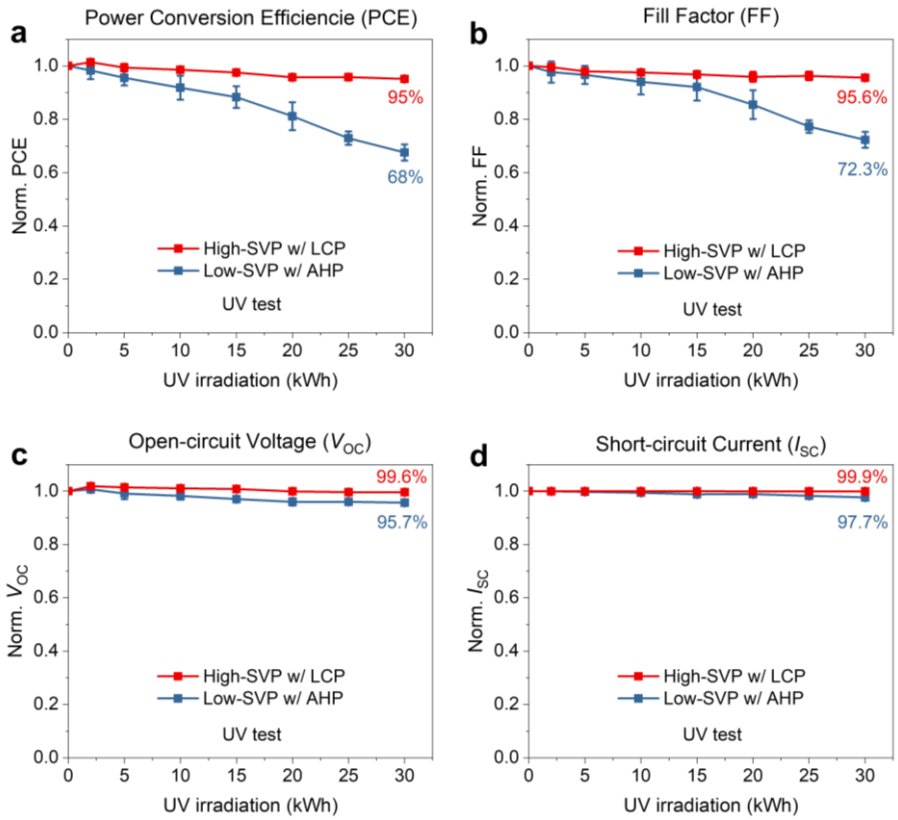

Supplementary Fig. 76 | UV preconditioning test with a cumulative UV irradiation of 30 kWh m^{-2} (5 modules for each type). Corresponding changes in the parameters **a,** PCE, **b,** FF, **c,** V_{OC}, and **d,** I_{SC}.

Supplementary Note 7:

The performance of the unit cell within the module.

Whether the performance of each unit cell within a module changes in a manner similar to the overall module performance. Here, we compared the relationship between the efficiency of individual unit cells and the overall module efficiency for both high-SVP perovskite modules with LCP passivation and low-SVP perovskite modules with AHP passivation. Furthermore, the modules were subjected to ultraviolet aging under a total solar irradiance of 20 kWh m^{-2}, and the concurrent efficiency degradation of both the unit cells and the modules was analyzed.

To enable simultaneous tracking of individual unit cells within a complete module, we fabricated a perovskite module with an active area of 810 cm^2. Seven independently measurable sub-cells, designated A through G, were interconnected via busbars (Supplementary Fig. 77). To assess operational stability, the modules require encapsulation. Here, we observed a notable phenomenon: after attaching the busbars to the sub-cells and performing high-temperature lamination encapsulation, the efficiencies of both the entire module and the individual sub-cells decrease. We attribute this efficiency loss to the mechanical stress induced by the busbars during the encapsulation process. In the following descriptions, modules before high-temperature lamination are referred to as "unencapsulated," while those after lamination are termed "encapsulated."

The sub-cells in the pristine low-SVP module with AHP passivation are labeled A1 to G1. The full module exhibited an efficiency of 19.32%, while the efficiencies of the individual unit cells ranged from 18.56% to 19.43% (Supplementary Fig. 78 and Supplementary Table 6), indicating inherent performance variations among the sub-cells.

Following encapsulation, both the module and sub-cell efficiencies exhibited a similar declining trend, characterized by a pronounced drop in FF (Supplementary Fig. 79 and Supplementary Table 7). After subsequent UV aging with a cumulative irradiance of 20 kWh m^{-2}, the module efficiency decreased by 17.5%, and the corresponding sub-cells showed synchronized degradation (Supplementary Fig. 80 and Supplementary Table 8), with FF remaining the most severely degraded photovoltaic parameter. For the high-SVP module with LCP passivation, encapsulation also led to an efficiency loss; however, the device still maintained excellent UV stability (Supplementary Figs. 81–83 and Supplementary Tables 9-11). These results indicate that inherent performance variations exist among the sub-cells within a single module, and the degradation observed at the module level is directly mirrored in the individual sub-cells.

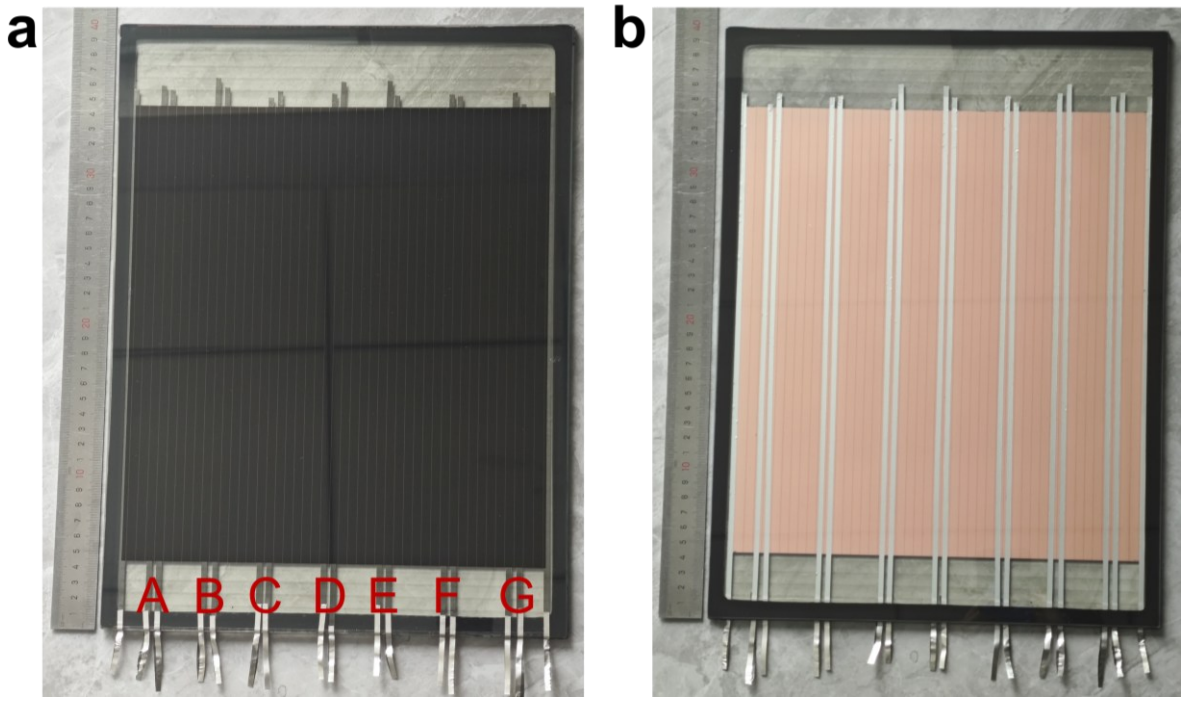

Supplementary Fig. 77 | Image of the perovskite module with an active area of 810 cm^2. a, Front (illuminated) side. **b,** Back (metal electrode) side.

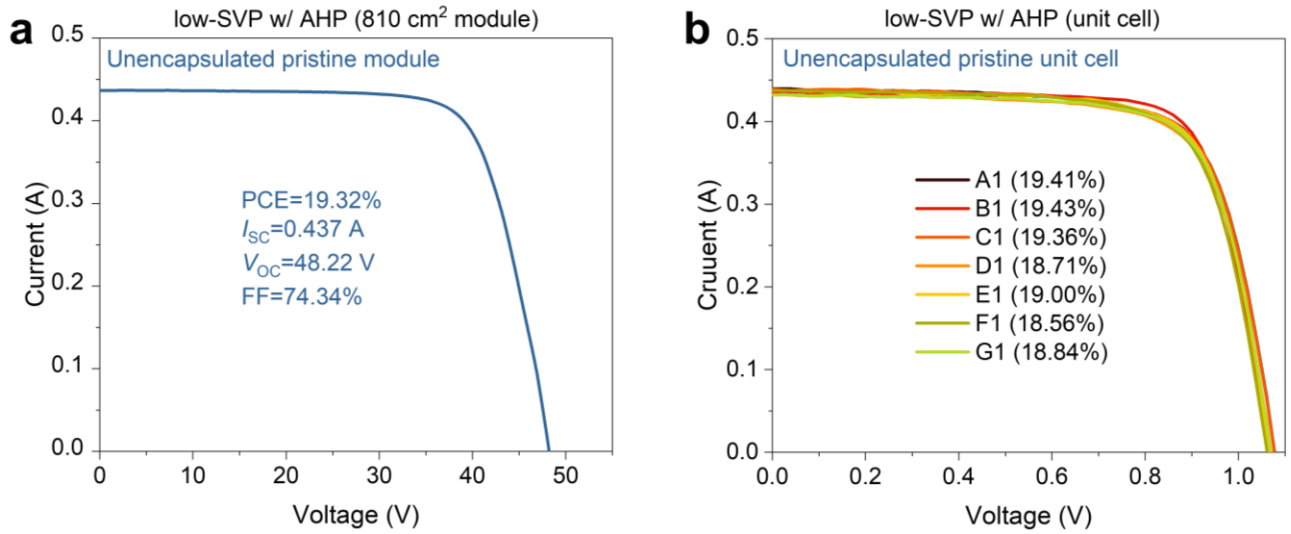

Supplementary Fig. 78 | *I-V* curves of pristine module. a, Unencapsulated 810 cm^2 module fabricated low -SVP perovskite w/ AHP. **b,** The unit cell within AHP module. A1 to G1 denote individual unit cells (A to G) in the low-SVP w/ AHP pristine module, with their spatial positions referenced in Supplementary Fig. 76.

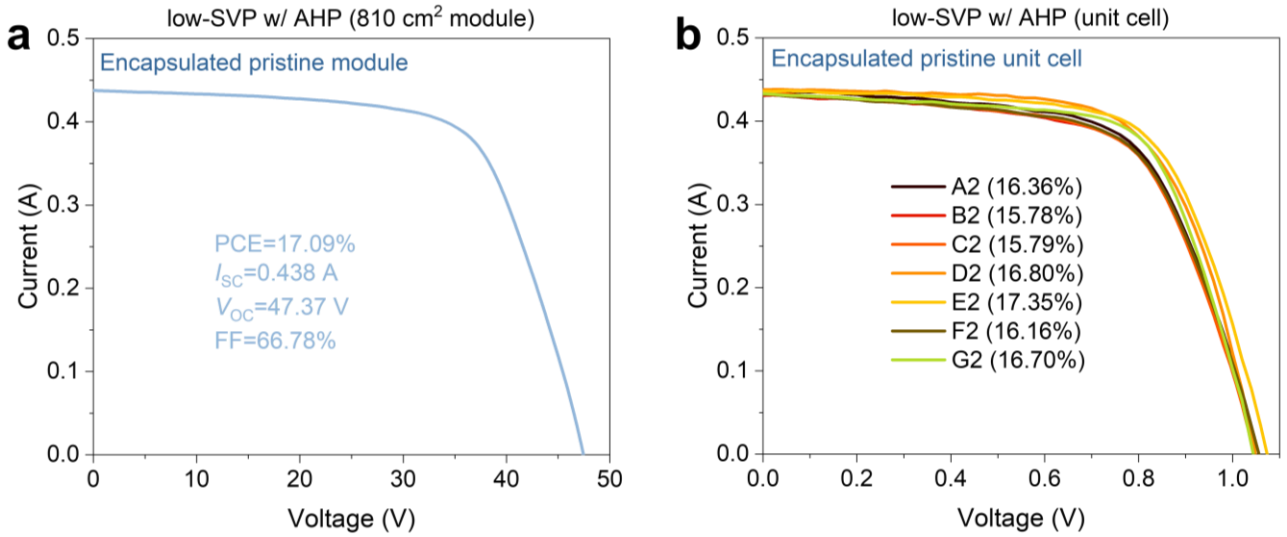

Supplementary Fig. 79 | *I-V* curves of pristine module. a, Encapsulated 810 cm^2 module fabricated low -SVP perovskite w/ AHP. **b,** The unit cell within AHP module. A2 to G2 denote individual unit cells (A to G) in the encapsulated pristine module.

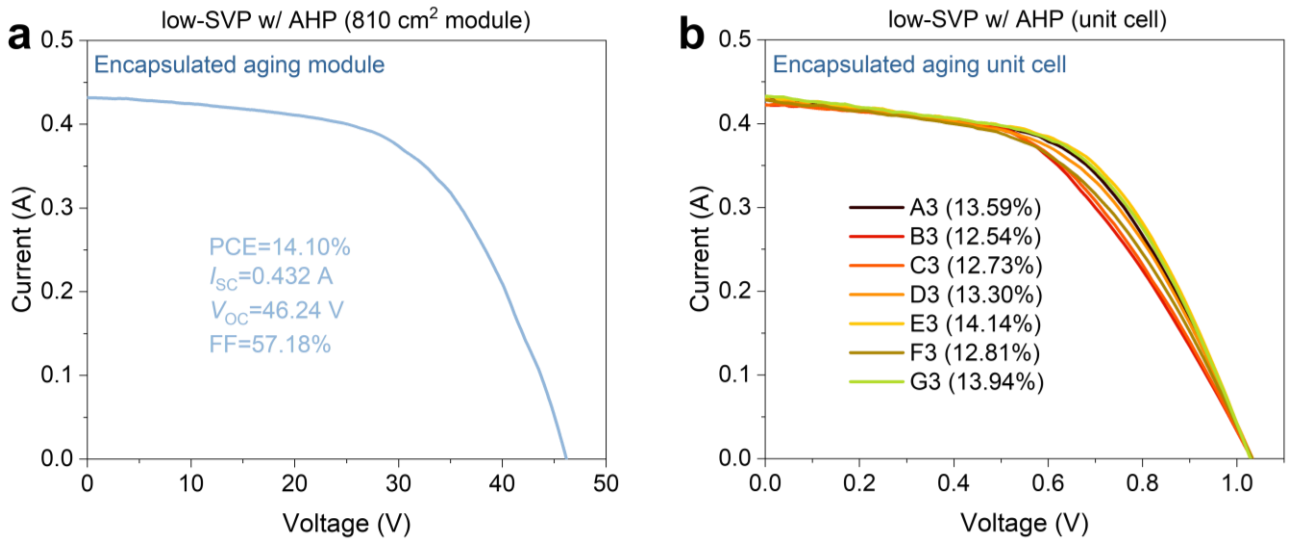

Supplementary Fig. 80 | *I-V* curves of aging module (the cumulative UV irradiation of 20 kWh m^{-2}). a, Encapsulated 810 cm^2 module fabricated low -SVP perovskite w/ AHP. **b,** The unit cell within AHP module. A3 to G3 denote individual unit cells (A to G) in the encapsulated aging module.

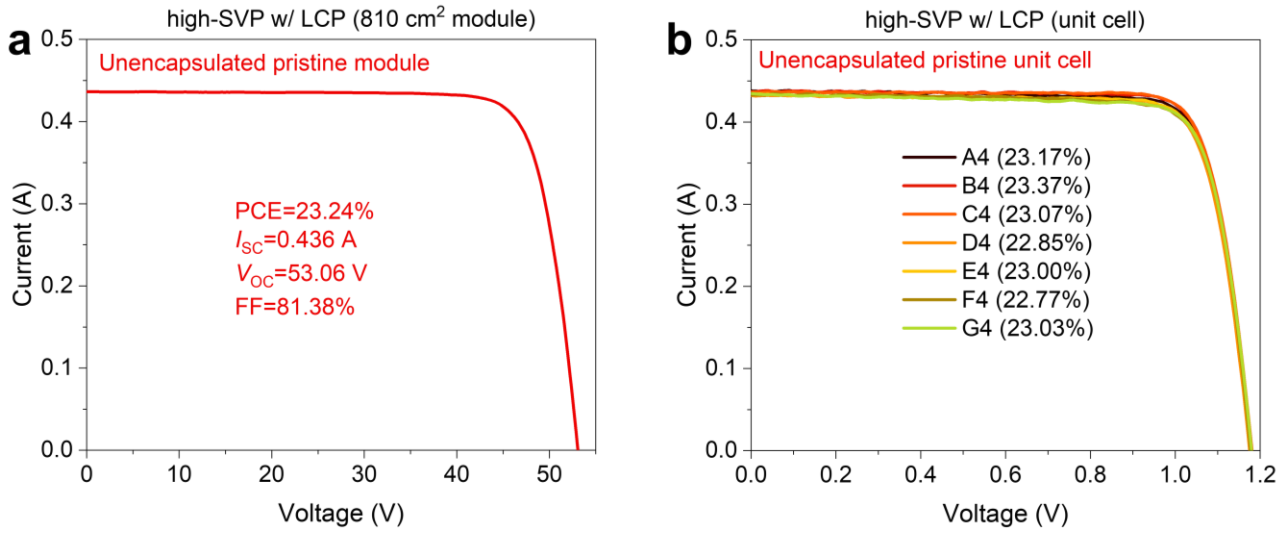

Supplementary Fig. 81 | *I-V* curves of pristine module. a, Unencapsulated 810 cm^2 module fabricated high-SVP perovskite w/ LCP. **b,** The unit cell within LCP module. A4 to G4 denote individual unit cells (A to G) in the high-SVP w/ LCP pristine module.

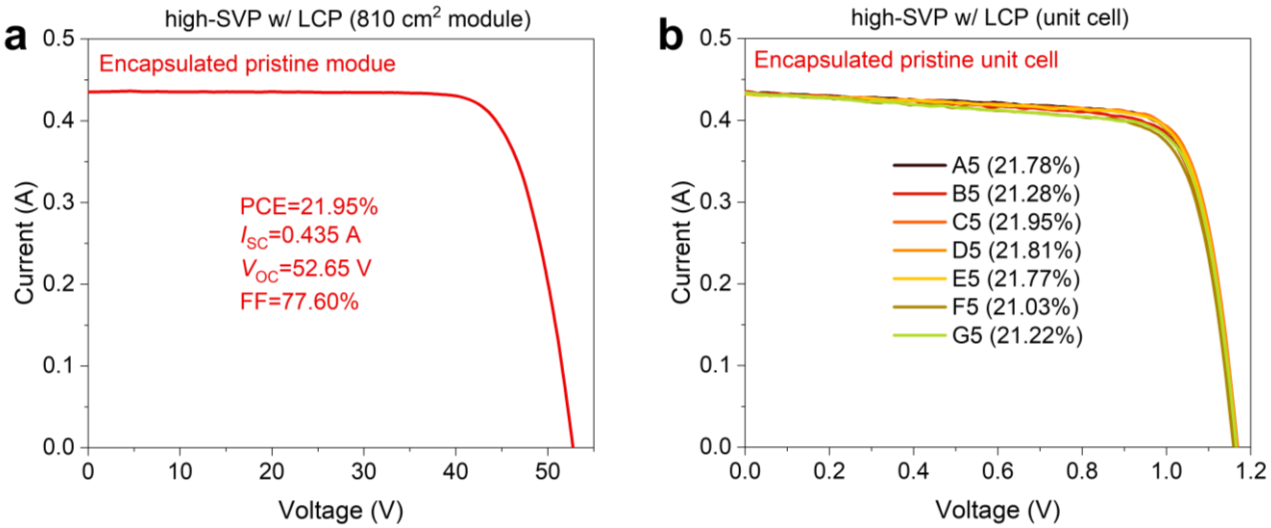

Supplementary Fig. 82 | *I-V* curves of pristine module. a, Encapsulated 810 cm^2 module fabricated high-SVP perovskite w/ LCP. **b,** The unit cell within LCP module. A5 to G5 denote individual unit cells (A to G) in the high-SVP w/ LCP pristine module.

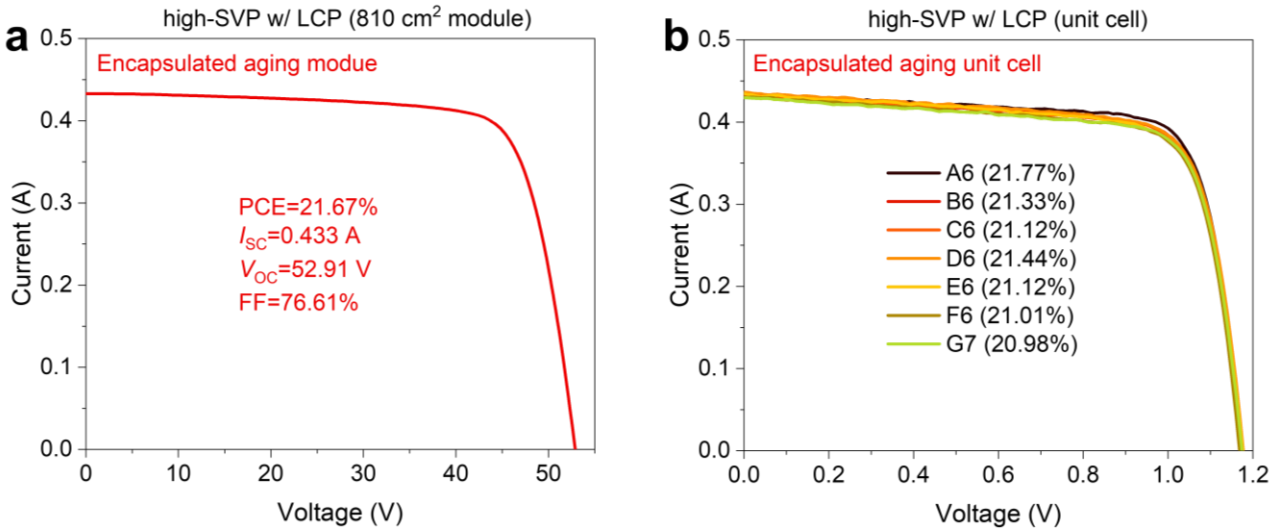

Supplementary Fig. 83 | *I-V* curves of aging module (the cumulative UV irradiation of 20 kWh m^{-2}). a, Encapsulated 810 cm^2 module fabricated high-SVP perovskite w/ LCP. **b,** The unit cell within LCP module. A4 to G4 denote individual unit cells (A to G) in the high-SVP w/ LCP aging module.

Supplementary Note 8:

The performance of modules modified hydrophobic AHP

We expanded the scope of AHP to include structures with hydrophobicity comparable to that of $Pb(OA)_2$. Specifically, we incorporated two distinct ammonium salts: trimethyltetradecylammonium chloride (TAC) and oleylamine hydrochloride (OAC) (Supplementary Fig. 84). By evaluating their performance within the low-SVP perovskite system, we provide a comprehensive validation of the advantages inherent to the LCP strategy.

Coating the perovskite surface with TAC and OAC yields hydrophobicity comparable to that of $Pb(OA)_2$ (Supplementary Fig. 85). Top-view SEM images reveal that both TAC and OAC treatments increase the surface roughness, yet induce distinctly different micro-morphologies (Supplementary Fig. 86). Upon introducing 1 mg mL^{-1} TAC, the surface develops a "fluffy" like texture with blurred grains, and increasing the concentration to 2 mg mL^{-1} further accentuates this disordered accumulation, resulting in a rougher film surface. In contrast, the OAC-treated perovskite exhibits polygonal grains of varying sizes, accompanied by well-defined and effectively filled grain boundaries, leading to a highly compact film. XRD characterization demonstrates that TAC removes surface PbI_2 but fails to form a two-dimensional (2D) structure, whereas OAC not only eliminates PbI_2 but also generates a low-dimensional perovskite phase (Supplementary Fig. 87). Consequently, we propose that TAC molecules tend to aggregate at the perovskite surface or grain boundaries, potentially increasing the interfacial resistance and impeding efficient carrier transport. In contrast, the long alkyl chains of OAC induce the formation of a 2D perovskite layer at the surface, which eliminates surface PbI_2 and promotes the growth of smaller perovskite crystallites.

Based on this, we fabricated perovskite modules with an active area of 810 cm^2. Both TAC and OAC modifications yielded a marginal increase in module efficiency (Supplementary Fig. 88). Subsequent stability testing of the modified modules revealed performance degradation under various conditions (Supplementary Fig. 89). Specifically, under ISOS-D-3 damp-heat testing, both module types degraded by approximately 10% within 500 h. Under ISOS-T-3 thermal cycling, efficiencies were maintained at only about 90% of the initial value after 150 cycles. Similarly, under UV aging, the modules exhibited a 10% efficiency loss after 14 kWh of cumulative irradiation. All these data demonstrate that the stability performance of the TAC and OAC modified modules is inferior to that achieved with the LCP strategy, further highlighting the superior performance provided by LCP passivation.

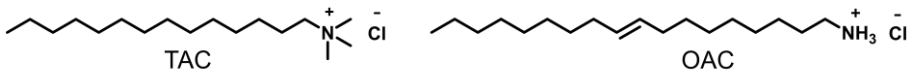

Supplementary Fig. 84 | Molecular Structures of TAC and OAC.

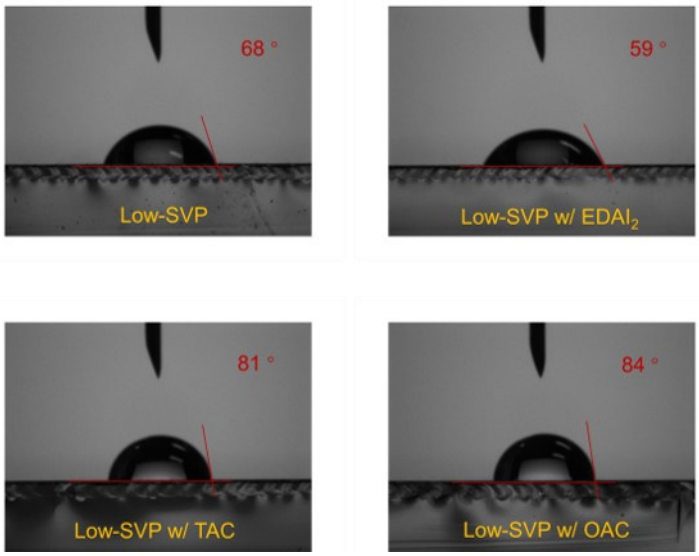

Supplementary Fig. 85 | Water contact angle measurements on perovskite film surface. The perovskite surfaces were modified with $EDAI_2$, TAC, and OAC, respectively.

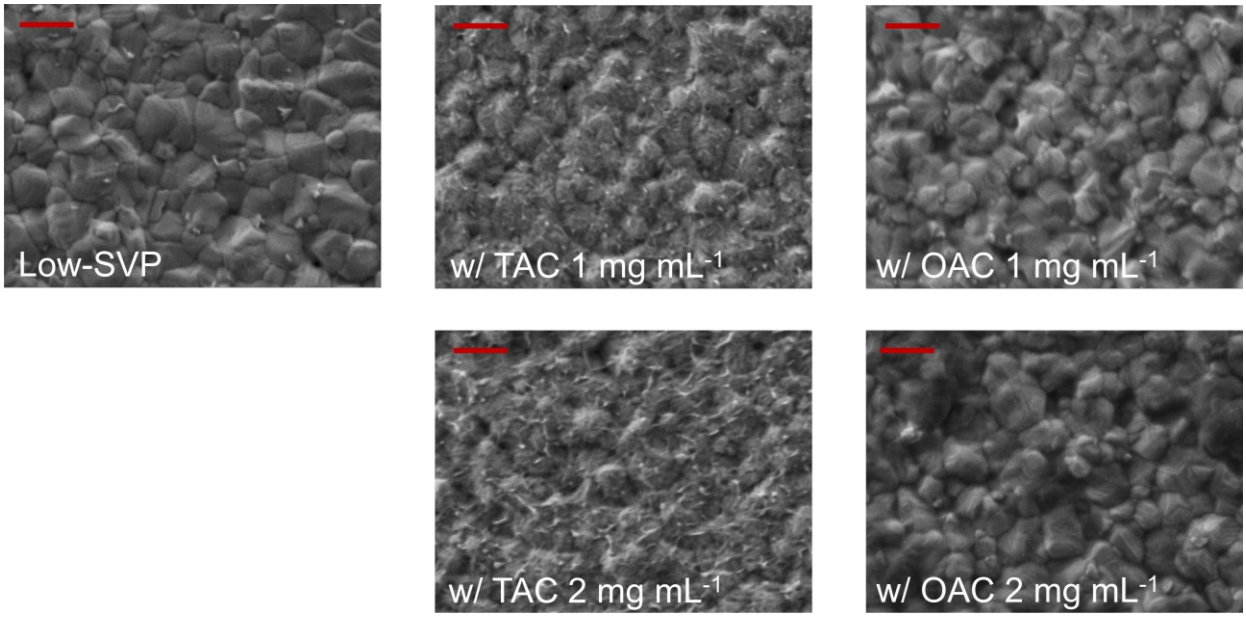

Supplementary Fig. 86 | SEM images of low-SVP perovskite films. The top-view SEM images of low-SVP perovskite film with TAC and OAC passivation. The scale bars correspond to 1 μm in all images.

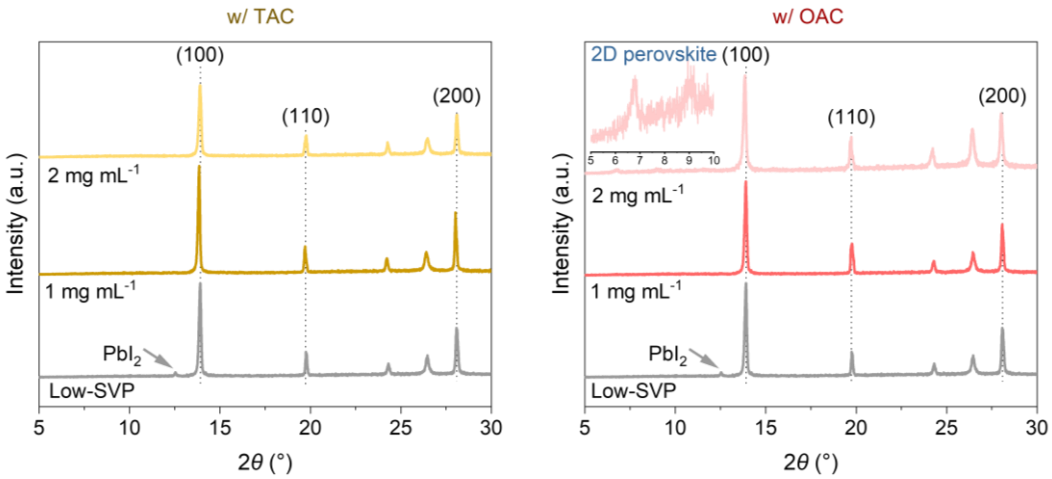

Supplementary Fig. 87 | XRD patterns of perovskite films. Surface characterization was conducted on the top surfaces of low-SVP perovskite films treated with varying concentrations (1 mg mL^{-1} and 2 mg mL^{-1}) of TAC and OAC.

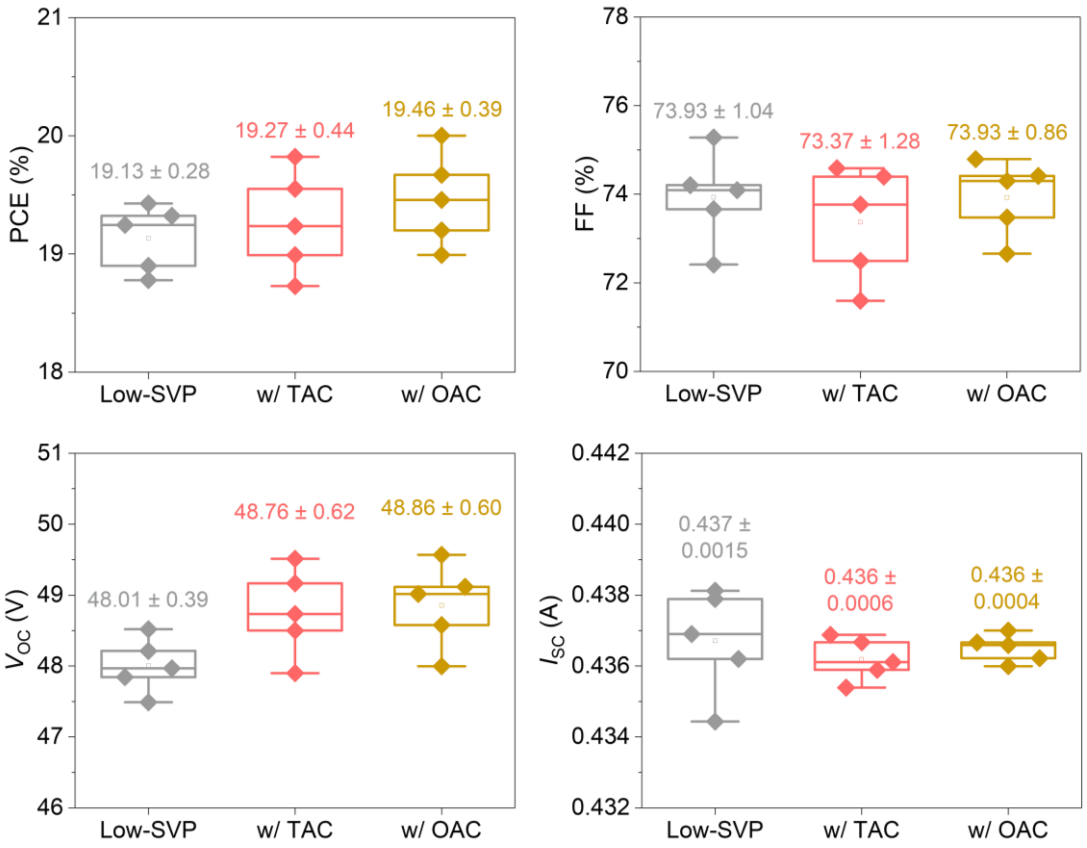

Supplementary Fig. 88 | Statistical photovoltaic parameters of the modules. The PV modules fabricated by low-SVP perovskite films with 1 mg mL^{-1} TAC and 1 mg mL^{-1} OAC. The aperture area of the module is 810 cm^2. Five parallel data sets were taken for each set of conditions. Scatters represent raw data; boxplots show the interquartile range with the median as the center line; whiskers indicate the 5th–95th percentiles. Numerical data are presented as mean ± SD.

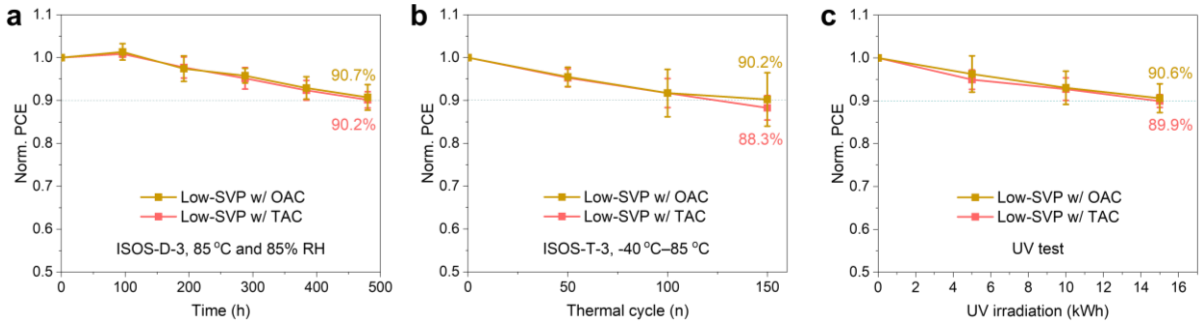

Supplementary Fig. 89 | Reliability tests of 810 cm^2 modules. a, Encapsulated PV modules aged under ISOS-D-3, **b,** ISOS-T-3 testing protocol, and **c,** UV preconditioning test with a cumulative UV irradiation (5 modules for each condition).

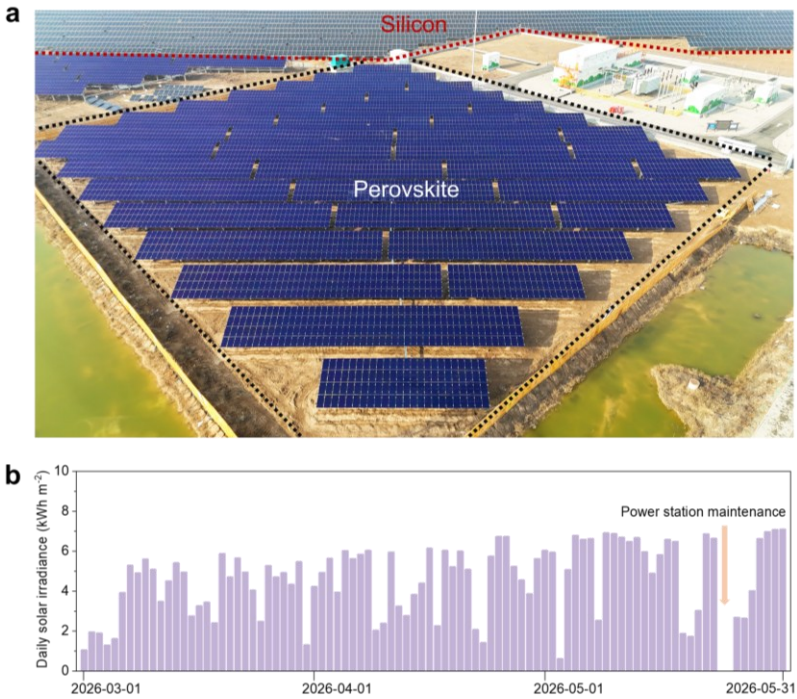

Supplementary Fig. 90 | Perovskite and silicon (TOPCon) photovoltaic power station. a, Photograph of the outdoor photovoltaic power station. **b,** Daily solar irradiance from March to May 2026.

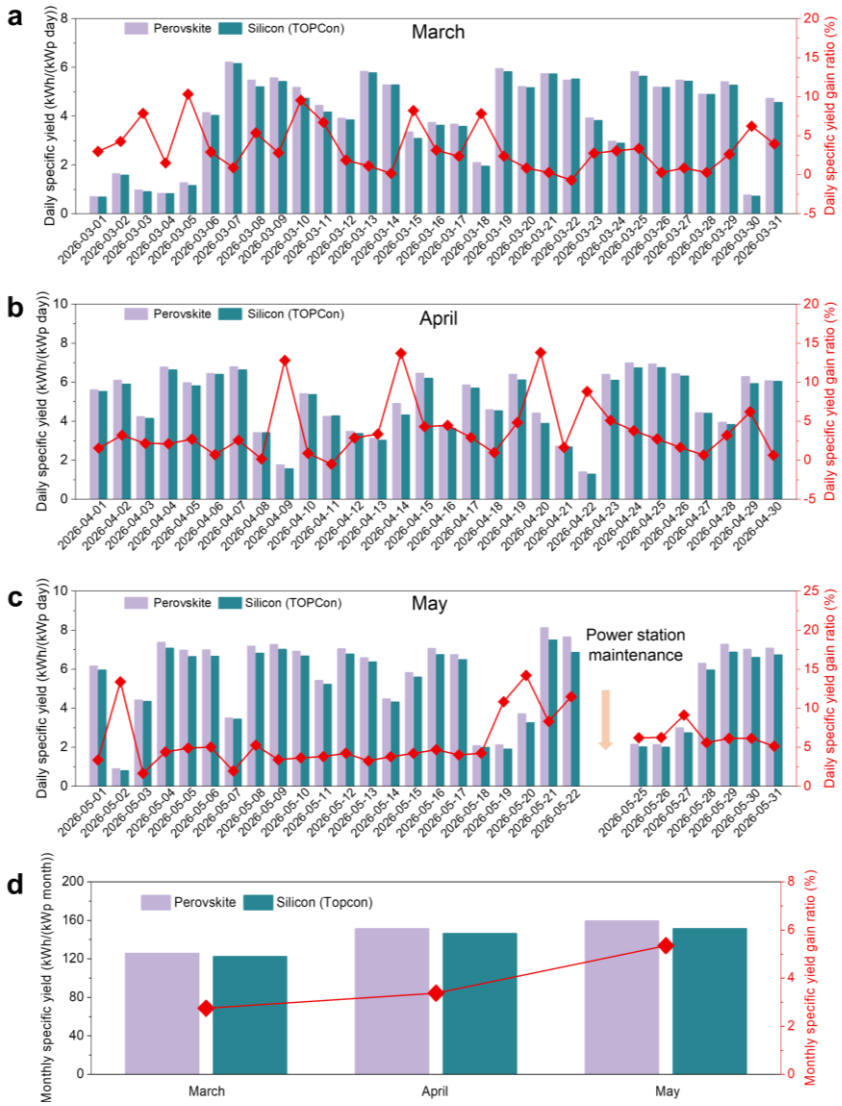

Supplementary Fig. 91 | Outdoor operational performance of perovskite and silicon PV station. **a–c,** Daily specific yield of the perovskite and silicon systems from March to May 2026. **d,** Monthly specific yield over the same period. The daily specific yield gain ratio represents the enhancement in daily specific energy yield of the perovskite relative to the silicon reference, calculated as (perovskite-silicon)/silicon.

Supplementary Table 1. Physicochemical properties of DOL, 2-Me, DMF, and DMSO, and their solubility for FAI and PbI_2. **Note.** Solubility measurements were conducted at room temperature. Values were determined by differential weighing after dissolving solutes into a supersaturated state. Minor errors may arise from this gravimetric approach.

		DOL	2-Me	DMF	DMSO
Boiling Point (°C)		75	128	153	189
SVP (kPa)		15.3	1.50	0.50	0.08
Solubility (mg mL^{-1})	**FAI**	Nearly insoluble	1030	1670	2130
	PbI_2	Insoluble	Nearly insoluble	310	550

Supplementary Table 2. The highest PV parameters of the different solvents PSMs from *I-V* curves shown in Supplementary Fig. 23.

	I_{SC} (A)	V_{OC} (V)	FF (%)	PCE (%)
Low-SVP	0.439	47.76	73.77	18.99
2-Me:DMSO	0.438	48.74	78.45	20.63
10% DOL	0.436	49.97	80.08	21.55
20% DOL	0.437	50.59	80.63	22.00
30% DOL (***High-SVP***)	0.437	50.92	82.03	22.51
40% DOL	0.437	50.34	81.12	22.04

Supplementary Table 3. The highest PV parameters of the 2-Me:DMSO PSMs without and with lead carboxylates passivators from *I-V* curves shown in Supplementary Fig. 37.

	I_{SC} (A)	V_{OC} (V)	FF (%)	PCE (%)
High-SVP	0.438	48.74	78.45	20.63
w/ $Pb(Ac)_2$	0.439	49.49	79.77	21.41
w/ $Pb(NA)_2$	0.438	49.74	79.73	21.44
w/ $Pb(AcAc)_2$	0.439	49.93	80.00	21.65
w/ $Pb(OA)_2$	0.439	50.56	80.38	22.02

Supplementary Table 4. The highest PV parameters of the low-SVP PSMs with ammonium salts from *I-V* curves shown in Supplementary Fig. 39.

	I_{SC} (A)	V_{OC} (V)	FF (%)	PCE (%)
Low-SVP	0.439	47.46	73.77	18.99
w/ PEABr	0.438	48.58	74.92	19.67
w/ PEAI	0.436	48.38	75.09	19.57
w/ $PDAI_2$	0.437	48.66	76.47	20.19
w/ $EDAI_2$	0.437	48.67	78.14	20.62

Supplementary Table 5. The highest PV parameters of the high-SVP perovskite films with LCP ($Pb(OA)_2$) at different concentrations from *I-V* curves shown in Supplementary Fig. 65.

	I_{SC} (A)	V_{OC} (V)	FF (%)	PCE (%)
High-SVP	0.437	50.92	82.03	22.51
0.5 mg mL^{-1}	0.437	52.32	82.36	23.22
1 mg mL^{-1}	0.436	52.91	82.90	23.62
1.5 mg mL^{-1}	0.437	53.38	84.15	24.23
2 mg mL^{-1}	0.435	52.67	83.49	23.60

Supplementary Table 6. The PV parameters of the unencapsulated pristine unit cells prepared low-SVP perovskite with AHP from *I-V* curves shown in Supplementary Fig. 78.

	I_{SC} (A)	V_{OC} (V)	FF (%)	PCE (%)
A1	0.439	1.077	73.84	19.41
B1	0.436	1.069	75.10	19.43
C1	0.439	1.077	73.68	19.36
D1	0.433	1.068	72.89	18.71
E1	0.437	1.066	73.41	19.00
F1	0.437	1.061	72.03	18.56
G1	0.432	1.068	73.53	18.84

Supplementary Table 7. The PV parameters of the encapsulated pristine unit cells prepared low-SVP perovskite with AHP from *I-V* curves shown in Supplementary Fig. 79.

	I_{SC} (A)	V_{OC} (V)	FF (%)	PCE (%)
A2	0.438	1.056	63.69	16.36
B2	0.431	1.045	63.05	15.78
C2	0.435	1.045	62.57	15.79
D2	0.438	1.049	65.85	16.80
E2	0.436	1.074	66.69	17.35
F2	0.432	1.057	63.69	16.16
G2	0.433	1.045	66.43	16.70

Supplementary Table 8. The PV parameters of the encapsulated aging unit cells prepared low-SVP perovskite with AHP from *I-V* curves shown in Supplementary Fig. 80.

	I_{SC} (A)	V_{OC} (V)	FF (%)	PCE (%)
A3	0.431	1.031	55.02	13.59
B3	0.423	1.031	51.79	12.54
C3	0.422	1.031	52.62	12.73
D3	0.429	1.033	53.96	13.30
E3	0.431	1.028	57.35	14.14
F3	0.428	1.032	52.14	12.81
G3	0.433	1.029	56.36	13.94

Supplementary Table 9. The PV parameters of the unencapsulated pristine unit cells prepared high-SVP perovskite with LCP from *I-V* curves shown in Supplementary Fig. 81.

	I_{SC} (A)	V_{OC} (V)	FF (%)	PCE (%)
A4	0.438	1.177	80.91	23.17
B4	0.437	1.177	81.87	23.37
C4	0.437	1.171	81.24	23.07
D4	0.432	1.175	80.96	22.85
E4	0.433	1.179	80.99	23.00
F4	0.433	1.177	80.44	22.77
G4	0.435	1.180	80.83	23.03

Supplementary Table 10. The PV parameters of the encapsulated pristine unit cells prepared high-SVP perovskite with LCP from *I-V* curves shown in Supplementary Fig. 82.

	I_{SC} (%)	V_{OC} (V)	FF (%)	PCE (%)
A5	0.434	1.165	77.51	21.78
B5	0.435	1.163	75.67	21.28
C5	0.433	1.169	77.99	21.95
D5	0.433	1.166	77.63	21.81
E5	0.433	1.166	77.59	21.77
F5	0.435	1.159	75.10	21.03
G5	0.435	1.166	75.39	21.22

Supplementary Table 11. The PV parameters of the encapsulated aging unit cells prepared high-SVP perovskite with LCP from *I-V* curves shown in Supplementary Fig. 83.

	I_{SC} (A)	V_{OC} (V)	FF (%)	PCE (%)
A6	0.431	1.176	77.25	21.77
B6	0.432	1.175	75.44	21.33
C6	0.431	1.173	75.23	21.12
D6	0.436	1.178	75.09	21.44
E6	0.435	1.176	74.34	21.12
F6	0.430	1.169	75.19	21.01
G6	0.430	1.174	74.89	20.98